J. Fluid Mech. (2019), *vol.* 876, *pp.* 356–412.
doi:10.1017/jfm.2019.543

Evolution of thermally stratified turbulent open channel flow after removal of the heat source

Michael P. Kirkpatrick[1],†, N. Williamson[1], S. W. Armfield[1] and V. Zecevic[1]

[1]School of Aerospace, Mechanical and Mechatronic Engineering, The University of Sydney, Sydney, NSW 2006, Australia

(Received 4 December 2018; revised 1 July 2019; accepted 1 July 2019; first published online 1 August 2019)

Evolution of thermally stratified open channel flow after removal of a volumetric heat source is investigated using direct numerical simulation. The heat source models radiative heating from above and varies with height due to progressive absorption. After removal of the heat source the initial stable stratification breaks down and the channel approaches a fully mixed isothermal state. The initial state consists of three distinct regions: a near-wall region where stratification plays only a minor role, a central region where stratification has a significant effect on flow dynamics and a near-surface region where buoyancy effects dominate. We find that a state of local energetic equilibrium observed in the central region of the channel in the initial state persists until the late stages of the destratification process. In this region local turbulence parameters such as eddy diffusivity k_h and flux Richardson number R_f are found to be functions only of the Prandtl number Pr and a mixed parameter $\mathcal{Q}$, which is equal to the ratio of the local buoyancy Reynolds number Re_b and the friction Reynolds number Re_τ. Close to the top and bottom boundaries turbulence is also affected by Re_τ and vertical position z. In the initial heated equilibrium state the laminar surface layer is stabilised by the heat source, which acts as a potential energy sink. Removal of the heat source allows Kelvin–Helmholtz-like shear instabilities to form that lead to a rapid transition to turbulence and significantly enhance the mixing process. The destratifying flow is found to be governed by bulk parameters Re_τ, Pr and the friction Richardson number Ri_τ. The overall destratification rate $\mathcal{D}$ is found to be a function of Ri_τ and Pr.

Key words: river dynamics, stratified flows, turbulent mixing

1. Introduction

When open channel flow is subjected to short-wave radiative heating from above progressive absorption of radiation by the fluid leads to a volumetric heat source that decreases with depth. This, combined with turbulence generation due to shear at the solid bottom surface, leads to a non-uniform stable temperature stratification profile in which stratification and its damping effects on turbulence are strongest close to the surface and weaken with depth. This situation occurs in rivers, canals, estuaries and shallow seas under the influence of solar heating. Damping of turbulence reduces

† Email address for correspondence: michael.kirkpatrick@sydney.edu.au

mixing of solutes in the fluid body. In the context of the environmental flows listed above, this can affect the levels and distribution of ecologically important chemical species such as dissolved oxygen, carbon dioxide, contaminants and nutrients (Turner & Erskine 2005).

For a given radiative forcing, the degree of turbulence damping that occurs increases as the flow rate decreases due to the associated reduction in turbulence generation due to shear at the channel bottom. Thus changes to natural flowing systems, such as the extraction of water from river systems for human purposes for example, can lead to reduced levels of dissolved oxygen along with increased contaminant concentrations, causing long-term damage to ecosystems (Turner & Erskine 2005). Reduced flow rates can also lead to acute ecological damage such as mass fish kills and cyanobacterial outbreaks, commonly known as algal blooms. These events have been found to be strongly associated with conditions in which high radiation levels combined with low flow rate leads to strong and persistent stable stratification (Sherman *et al.* 1998; Webster *et al.* 2000; Bormans, Ford & Fabbro 2005).

In previous work Williamson *et al.* (2015) studied the statistically steady state reached by a turbulent open channel flow subjected to radiative heating. The radiative heating was modelled using a volumetric heat source following the Beer–Lambert law. The volumetric heat source acts as a sink of gravitational potential energy, so the equilibrium flow state represents a state in which the turbulent kinetic energy generated by shear within the channel is in global balance with a combination of viscous dissipation and this potential energy sink. Conversion of turbulent kinetic energy to potential energy occurs through a downwards buoyancy flux. This steady state flow models the situation in a physical system in which solar heating has occurred over a long enough period of time for steady state to be achieved, for example the state of a river at the end of a sunny day.

In the current paper we study the evolution of the same flow when this heat source is removed and both top and bottom boundaries are kept adiabatic. In terms of the physical analogues mentioned above, this corresponds to situations in which solar forcing is removed and there is negligible heat transfer across the upper surface and bottom. This might occur when the sky becomes cloudy or the Sun sets while air temperature and humidity remain relatively high. A study of the flow with a non-adiabatic upper surface representing convective and radiative cooling that occurs at night or as the result of the passing of a cold front is the subject of a second paper.

With no heat input the temperature field gradually mixes and stratification weakens progressively until it approaches a fully mixed isothermal state. This can again be interpreted in terms of energy transfers. In this case, however, both mean flow kinetic energy and turbulent kinetic energy are converted into potential energy. Since the potential energy sink has been removed, potential energy increases as the flow approaches a final isothermal state.

A key finding of the study by Williamson *et al.* (2015) was that the turbulence in the central region of the steady state flow is in a state of local energetic equilibrium, that is $P \approx B + \varepsilon$, where P is shear production, B buoyancy destruction and ε viscous dissipation of turbulent kinetic energy. As a consequence, this region exhibits behaviour similar to that seen in studies of homogeneous stratified sheared turbulence such as those of Shih *et al.* (2005) and Chung & Matheou (2012). In the destratifying flow, we find that this region remains in energetic equilibrium as the flow evolves. As a consequence, as the flow destratifies, it sweeps through large ranges of local turbulence parameters such as the gradient Richardson number Ri and buoyancy

Reynolds number Re_b, making it a useful flow for determining scaling relationships between these local turbulence parameters and local flow properties such as eddy diffusivity k_h.

Previous studies of stratified channel flow such as those of Garg *et al.* (2000), Taylor, Sarkar & Armenio (2005) and Garcia-Villalba & del Alamo (2011) have found the friction Richardson number Ri_τ to be a useful parameter for characterising buoyancy effects in this context. Again, our destratifying flow sweeps through a large range of this parameter allowing us to explore the relationships between Ri_τ and local flow parameters and properties such as Re_b and k_h, as well as bulk flow behaviour such as the destratification rate.

Studies of the time evolution of turbulent flows due to a change in thermal forcing are relatively few in number. A recent experimental study by Van Buren *et al.* (2017) investigates the effect on a turbulent boundary layer of decreasing wall temperature. In their flow stratification is increasing with time, in contrast to our case where stratification decreases.

The overarching aim of this paper is to determine a scaling relationship for the destratification rate in terms of bulk parameters that can be predicted by large scale forecasting models such as hydraulic river models. Global destratification rate is dependent on vertical turbulent transport of heat within the channel, which depends on eddy diffusivity. So our approach is to first investigate relationships between eddy diffusivity k_h and local turbulence parameters such as Ri and Re_b. We then extend this to include bulk parameters Re_τ and Ri_τ. This leads finally to a scaling relationship for destratification rate in terms of bulk parameters that is justifiable in terms of our observations regarding the physical processes occurring locally within the channel.

The remainder of this paper is structured as follows. Section 2 describes the mathematical formulation of the problem including the governing equations and non-dimensionalisation approach used. Details of the numerical simulations including the numerical methods used and the parameter ranges considered are given in § 3. In § 4 we give an overview of the flow evolution and initial conditions. Section 5 shows how vertical profiles of important local turbulence parameters change as the flow evolves. Section 6 discusses bulk flow energetics and energy transfers. Section 7 discusses relationships amongst local parameters in the central region of the channel and introduces the mixed parameter $\mathcal{Q} = Re_b/Re_\tau$ while § 8 addresses the dynamics of the near-surface region. In § 9 we compare our data with various scalings based on Monin–Obukhov theory while § 10 discusses scalings between local turbulence parameters and the friction Richardson number Ri_τ. Finally in § 11 we derive a scaling relationship for destratification rate in terms of bulk parameters and present results to support this model.

2. Problem formulation

2.1. *The initial heated equilibrium state flow*

We use the framework for the radiatively heated equilibrium state flow described by Williamson *et al.* (2015). A schematic of the flow is shown in figure 1. It is an open channel flow with an adiabatic, no-slip wall at the lower surface, an adiabatic, free-slip impermeable boundary at the upper surface and periodic boundaries in the streamwise and spanwise directions. The flow is driven by a constant pressure gradient in the streamwise direction and radiative heating is represented by a depth-dependent volumetric heat source $\tilde{q}_r(\tilde{z})$ following the Beer–Lambert law,

$$\tilde{q}_r(\tilde{z}) = \tilde{I}_s \tilde{\alpha} \mathrm{e}^{(\tilde{z}-\tilde{h})\tilde{\alpha}}. \tag{2.1}$$

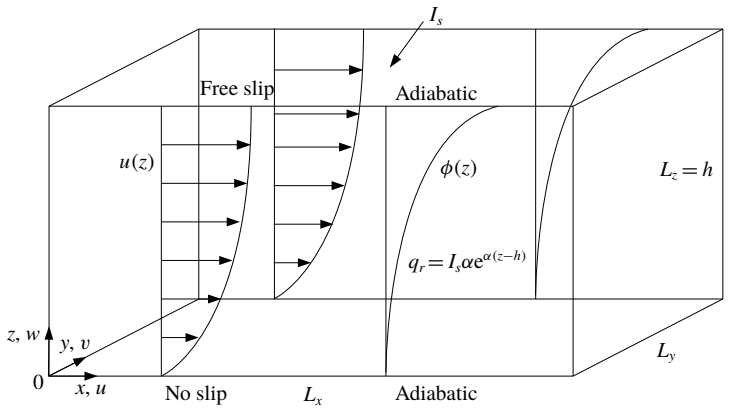

FIGURE 1. Schematic of the radiatively heated equilibrium flow.

Here $\tilde{I}_s$ is the short-wave radiative heat flux through the upper surface, $\tilde{\alpha}$ the attenuation coefficient due to turbidity and $\tilde{h}$ the channel depth. Here and throughout this paper a tilde $\tilde{\cdot}$ indicates a dimensional quantity, whereas a variable with no tilde is non-dimensional.

The temperature field $\tilde{\phi}$ is decomposed into a time varying mean and a statistically steady fluctuating component,

$$\tilde{\Phi}(\tilde{x}, \tilde{t}) = \tilde{\Phi}_v(\tilde{t}) + \tilde{\phi}(\tilde{x}, \tilde{t}). \tag{2.2}$$

Here $\tilde{\Phi}_v(\tilde{t})$ is the domain-averaged temperature at time $\tilde{t}$, which increases with time according to

$$\frac{\mathrm{d}\tilde{\Phi}_v}{\mathrm{d}\tilde{t}} = \frac{\tilde{Q}_r}{\tilde{\rho}_b \tilde{c}_p}, \tag{2.3}$$

where $\tilde{\rho}_b$ and $\tilde{c}_p$ are a reference density and the specific heat of the fluid, and $\tilde{Q}_r$ is the domain averaged radiative heat source,

$$\tilde{Q}_r = \frac{1}{\tilde{h}} \int_0^{\tilde{h}} \tilde{q}_r(\tilde{z})\, \mathrm{d}\tilde{z}. \tag{2.4}$$

The heat source is non-dimensionalised as

$$q_r(z) = \frac{\tilde{q}_r(\tilde{z}) - \tilde{Q}_r}{\tilde{Q}_N}, \tag{2.5}$$

where

$$\tilde{Q}_N = \frac{1}{\tilde{h}^2} \int_0^{\tilde{h}} (\tilde{Q}_r - \tilde{q}_r(\tilde{z}))(\tilde{h} - \tilde{z})\, \mathrm{d}\tilde{z}. \tag{2.6}$$

The temperature fluctuation field is non-dimensionalised as

$$\phi(x, t) = \frac{\tilde{\Phi}(\tilde{x}, \tilde{t}) - \tilde{\Phi}_v(\tilde{t})}{\tilde{\Phi}_N}, \tag{2.7}$$

where

$$\tilde{\Phi}_N = \frac{\tilde{Q}_N \tilde{h}}{\tilde{\rho}_b \tilde{c}_p \tilde{u}_\tau}. \tag{2.8}$$

Here $\tilde{u}_\tau$ is the friction velocity associated with the shear stress on the lower solid surface.

Williamson *et al.* (2015) define a non-dimensional bulk stability parameter,

$$\lambda = \tilde{h}/\tilde{\mathcal{L}}, \tag{2.9}$$

where $\tilde{\mathcal{L}}$ is a bulk Obukhov length scale defined as

$$\tilde{\mathcal{L}} = \frac{\tilde{u}_\tau^3}{\tilde{g}\tilde{\beta}\tilde{I}_s/\tilde{\rho}_b\tilde{c}_p}\left(\frac{1}{2} - \frac{1}{\tilde{\alpha}\tilde{h}}\right)^{-1}. \tag{2.10}$$

Here $\tilde{g}$ is gravitational acceleration and $\tilde{\beta}$ the coefficient of thermal expansion, which relates fluid density $\tilde{\rho}$ to temperature through $\mathrm{d}\tilde{\rho}/\tilde{\rho}_b = -\tilde{\beta}\,\mathrm{d}\tilde{\phi}$. This formulation of the Obukhov length scale results from the current context in which the heat flux into the domain takes the form of a volumetric heat source given in (2.1), which leads to

$$\tilde{Q}_N \approx \frac{\tilde{I}_s}{\tilde{h}}\left(\frac{1}{2} - \frac{1}{\tilde{\alpha}\tilde{h}}\right). \tag{2.11}$$

Combining this with (2.8) gives an alternative expression for λ,

$$\lambda = \frac{\tilde{\beta}\tilde{g}\tilde{\Phi}_N\tilde{h}}{\tilde{u}_\tau^2}, \tag{2.12}$$

which has the same form as a friction Richardson number.

The heated equilibrium state flow is governed by the Oberbeck–Boussinesq form of the equations for conservation of mass, momentum and energy for an incompressible fluid. These are written in non-dimensional Cartesian tensor form as

$$\frac{\partial u_j}{\partial x_j} = 0, \tag{2.13}$$

$$\frac{\partial u_i}{\partial t} + \frac{\partial u_i u_j}{\partial x_j} = -\frac{\partial p}{\partial x_i} + \nu\frac{\partial^2 u_i}{\partial x_j^2} + \delta_{i1} + \lambda_0\phi\delta_{i3}, \tag{2.14}$$

$$\frac{\partial \phi}{\partial t} + \frac{\partial \phi u_j}{\partial x_j} = \sigma\frac{\partial^2 \phi}{\partial x_j^2} + q_r. \tag{2.15}$$

Here u_i are the Cartesian components of the velocity vector $\boldsymbol{u}$, p the pressure, x_i the components of the position vector $\boldsymbol{x}$, t time, ν kinematic viscosity and σ thermal diffusivity; δ_{ij} represents the Kronecker delta. Summation over repeated indices is assumed. The flow is driven by a constant uniform pressure gradient, δ_{i1}, in the streamwise direction; q_r is the radiative volumetric heat source given in (2.1) and (2.5).

The variables are non-dimensionalised using the following scheme,

$$\left.\begin{gathered} u=\frac{\tilde{u}}{\tilde{u}_{\tau,0}}, \quad \phi=\frac{\tilde{\phi}}{\tilde{\Phi}_{N,0}}, \quad p=\frac{\tilde{p}}{\tilde{\rho}_b\tilde{u}_{\tau,0}^2}, \quad x=\frac{\tilde{x}}{\tilde{h}_0}, \quad t=\frac{\tilde{u}_{\tau,0}\tilde{t}}{\tilde{h}_0}, \\ \nu=\frac{\tilde{\nu}}{\tilde{u}_{\tau,0}\tilde{h}_0}\equiv\frac{1}{Re_{\tau,0}}, \quad \sigma=\frac{\tilde{\sigma}}{\tilde{u}_{\tau,0}\tilde{h}_0}\equiv\frac{1}{Re_{\tau,0}Pr}. \end{gathered}\right\} \tag{2.16}$$

The subscript 0 indicates use of the characteristic length, velocity and temperature scales for the equilibrium state, that is $\tilde{h}_0$, $\tilde{u}_{\tau,0}$ and $\tilde{\Phi}_{N,0}$, respectively. This distinction is necessary because in the subsequent destratifying flow the length scale $\tilde{h}$ and velocity scale $\tilde{u}_\tau$ will typically vary with time.

Hence, for the equilibrium state, the friction Reynolds number is

$$Re_{\tau,0}=\frac{\tilde{u}_{\tau,0}\tilde{h}_0}{\tilde{\nu}}, \tag{2.17}$$

the molecular Prandtl number,

$$Pr=\frac{\tilde{\nu}}{\tilde{\sigma}}, \tag{2.18}$$

the stability parameter,

$$\lambda_0=\frac{\tilde{\beta}\tilde{g}\tilde{\Phi}_{N,0}\tilde{h}}{\tilde{u}_{\tau,0}^2}, \tag{2.19}$$

and the characteristic temperature scale,

$$\tilde{\Phi}_{N,0}=\frac{\tilde{Q}_{N,0}\tilde{h}_0}{\tilde{\rho}_b\tilde{c}_p\tilde{u}_{\tau,0}}. \tag{2.20}$$

Boundary conditions for the bottom ($z=0$) and top ($z=1$) boundaries are

$$z=0: u=v=w=0; \quad \frac{\partial\phi}{\partial z}=0, \tag{2.21a,b}$$

$$z=1: \frac{\partial u}{\partial z}=\frac{\partial v}{\partial z}=0; \quad w=0; \quad \frac{\partial\phi}{\partial z}=0. \tag{2.22a–c}$$

Boundary conditions for all lateral boundaries are periodic.

The equilibrium state flow is defined by specifying $Re_{\tau,0}$, λ_0, Pr and a non-dimensional turbidity parameter $\alpha_0=\tilde{\alpha}\tilde{h}_0$.

A random realisation of the equilibrium state flow is used as the initial conditions of the destratifying flow.

2.2. *The destratifying flow*

When a physical open channel flow evolves from an initially stratified state to a final neutrally stratified state, changes in the balance between turbulent and laminar shear stresses within the channel lead to changes in the mean velocity profile, resulting in an increase in the coefficient of friction, $C_f=2(\tilde{u}_\tau/\tilde{U}_b)^2$. Here $\tilde{U}_b$ is the bulk flow velocity. In a physical open channel flow, the flow will typically respond with a change in height and deceleration of the flow.

In our simulations the height h is fixed and the flow is driven by a constant pressure gradient. As a result, an increase in C_f leads to an increase in the friction velocity, leading to an imbalance between wall shear stress and the applied pressure gradient. Over time, this imbalance causes the flow to gradually decelerate, reducing the friction velocity, until the force balance is restored.

In order to model the physical flow, the equations for the simulations of the destratifying flow are non-dimensionalised in terms of a time varying friction velocity $\tilde{u}_\tau(\tilde{t})$ and height $\tilde{h}(\tilde{t})$. The characteristic temperature scale used is fixed at the scale of the initial equilibrium state $\tilde{\Phi}_{N,0}$. This gives governing equations

$$\frac{\partial u_j}{\partial x_j} = 0, \tag{2.23}$$

$$\frac{\partial u_i}{\partial t} + \frac{\partial u_i u_j}{\partial x_j} = -\frac{\partial p}{\partial x_i} + \nu \frac{\partial^2 u_i}{\partial x_j^2} + \delta_{i1} + \gamma \phi \delta_{i3}, \tag{2.24}$$

$$\frac{\partial \phi}{\partial t} + \frac{\partial \phi u_j}{\partial x_j} = \sigma \frac{\partial^2 \phi}{\partial x_j^2}, \tag{2.25}$$

where

$$\left.\begin{aligned} u = \frac{\tilde{u}}{\tilde{u}_\tau}, \quad \phi = \frac{\tilde{\phi}}{\tilde{\Phi}_{N,0}}, \quad p = \frac{\tilde{p}}{\tilde{\rho}_b \tilde{u}_\tau^2}, \quad x = \frac{\tilde{x}}{\tilde{h}}, \quad \partial t = \frac{\tilde{u}_\tau \partial \tilde{t}}{\tilde{h}}, \quad \hat{t} = \frac{\tilde{u}_{\tau,0} \tilde{t}}{\tilde{h}_0}, \\ \nu = \frac{\tilde{\nu}}{\tilde{u}_\tau \tilde{h}} \equiv \frac{1}{Re_\tau}, \quad \sigma = \frac{\tilde{\sigma}}{\tilde{u}_\tau \tilde{h}} \equiv \frac{1}{Re_\tau Pr}, \quad \gamma = \frac{\tilde{\beta} \tilde{g} \tilde{\Phi}_{N,0} \tilde{h}}{\tilde{u}_\tau^2}. \end{aligned}\right\} \tag{2.26}$$

The boundary conditions are the same as those for the equilibrium state flow.

Due to the time variation of the velocity and length scales used to non-dimensionalise (2.23)–(2.25), integrating them in time is problematic. Instead, we have chosen to solve a dynamically equivalent set of equations and then renormalise the solution to give the solution to the equations above. This procedure is described in appendix A.

Whilst (2.23)–(2.25) were not solved directly, they are useful in the context of scaling analysis because they give the time rate of change of the dependent variables, $\boldsymbol{u}$, p and ϕ, relative to a characteristic friction time scale $\tilde{t}_\tau = \tilde{h}/\tilde{u}_\tau$ determined from flow conditions at a particular instant in 'measured time', $\hat{t}$. In our simulations, measured time, $\hat{t}$, is dimensional time $\tilde{t}$ normalised in terms of the initial friction velocity and height as shown in (2.26). Thus, in the following, t is used only within differentials ∂t and dt, while $\hat{t}$ refers to the point in time within the process at which a particular set of flow conditions occur.

In place of the stability parameter λ_0, the buoyancy term of the momentum equations for the destratifying flow (2.24) uses γ, which is defined as

$$\gamma = \frac{\tilde{\beta} \tilde{g} \tilde{\Phi}_{N,0} \tilde{h}}{\tilde{u}_\tau^2}. \tag{2.27}$$

In the destratifying flow, λ_0 no longer has the same function as it does in the equilibrium state equations. In the equilibrium state equations, λ_0, through its dependence on Q_N, couples the heat source q_r in the temperature equation to the buoyancy term $\lambda_0 \phi$ in the momentum equations. At the same time it is also a function

of the wall shear stress via friction velocity $\tilde{u}_{\tau,0}$. Through these interconnections it determines the stability of the equilibrium state flow. In the transient flow simulations this coupling no longer exists since q_r has been removed and ϕ is normalised by $\tilde{\Phi}_{N,0}$ frozen at its equilibrium state value.

Like λ, γ also has a form similar to the friction Richardson number,

$$Ri_\tau = \frac{\tilde{\beta}\tilde{g}\Delta\tilde{\phi}\tilde{h}}{\tilde{u}_\tau^2}, \tag{2.28}$$

where $\Delta\tilde{\phi}$ is the difference between the mean temperature at the top and bottom of the channel. Ri_τ can be reformulated in terms of our non-dimensional variables as

$$Ri_\tau = \frac{\gamma\,\Delta\phi h}{u_\tau^2}. \tag{2.29}$$

The friction Richardson number Ri_τ is a bulk parameter that represents the ratio between stabilising effects of temperature stratification and the destabilising effects of shear at the wall. At high Ri_τ the effects of temperature stratification are dominant and the flow is strongly affected by buoyancy. At low Ri_τ the effect of shear dominates and the flow is only weakly affected by buoyancy. The destratification process involves moving from an initial state in which the flow is strongly affected by buoyancy to a final state in which buoyancy effects are insignificant.

The parameter Ri_τ has been found to be a useful bulk parameter for characterising buoyancy effects in other types of stratified channel flow (see Garg *et al.* 2000; Garcia-Villalba & del Alamo 2011, for example). Based on this, and given that λ determines the stability of the heated equilibrium flow and has a form similar to Ri_τ, we suggest that Ri_τ plays the equivalent function in the destratifying flow.

Thus the proposed governing parameters for the destratifying flow are Re_τ, Ri_τ, Pr with α_0 and λ_0 affecting the flow only via the initial conditions.

3. Numerical simulations

A set of initial states covering a range of turbulence and stability conditions was generated by running direct numerical simulations (DNS) of the heated equilibrium state flow solving (2.13)–(2.15). Equilibrium states were generated for the parameter combinations shown in table 1. Whilst we have proposed that Ri_τ takes the place of λ_0 as a governing parameter for the destratifying flow, since it is not a governing parameter for the equilibrium state flow it was not possible generate initial conditions corresponding to specific values of Ri_τ. Instead we have varied λ_0. The initial values of the friction Richardson number $Ri_{\tau,0}$ are also shown.

Each simulation was run for an initial spin-up period of $t = 0$–30 for the $\lambda_0 = 0$–1 cases and $t = 0$–40 for the $\lambda_0 = 2$ cases. By these times bulk parameters such as wall shear stress, bulk and mean velocities and the temperature difference between the upper and lower surfaces had reached statistically steady state. Full realisations of the flow state were then recorded over a further 20 time units at an interval of 0.5 time units to allow the calculation of equilibrium state statistics where required.

Using each of these equilibrium states as the initial conditions, a set of transient simulations was run solving (2.23)–(2.25). Realisations of the transient flow were recorded at intervals of 0.1 time units. The total integration time for transient simulations depends on the initial conditions and ranged between approximately 5 and 15 time units.

Case	$Re_{\tau,0}$	$Re_{\tau,max}$	λ_0	$Ri_{\tau,0}$	Pr	α_0
1	540	570	0.5	30	0.71	8
2	540	610	1	101	0.71	8
3	540	660	2	284	0.71	8
4	225	285	2	175	0.71	8
5	360	445	2	233	0.71	8
6	360	410	1	82	0.71	8
7	360	410	1	64	0.5	8
8	360	415	1	117	1	8
9	360	410	1	74	0.71	4
10	360	410	1	97	0.71	16
11	360	360	0	0	0.71	8

TABLE 1. Simulation parameters defined in terms of initial heated equilibrium state.

Grid	$Re_{\tau,0}$	$N_x \times N_y \times N_z$	$L_x \times L_y \times L_z$
A	225	$480 \times 240 \times 162$	$2\pi \times \pi \times 1$
B	360	$768 \times 384 \times 200$	$2\pi \times \pi \times 1$
C	540	$1152 \times 576 \times 264$	$2\pi \times \pi \times 1$
D	360	$1152 \times 576 \times 264$	$2\pi \times \pi \times 1$

TABLE 2. Grids and domain sizes used for each Reynolds number.

As discussed above, the friction velocity increases as the flow destratifies and adapts to the changes in the turbulent shear stress profile. As a result the actual friction Reynolds number of the time evolving simulations increases. This increase is significant, especially for the high λ_0 cases. The maximum Reynolds number reached in each case is shown in table 1.

Simulations were performed using the PUFFIN code (Kirkpatrick 2002). The equations are discretised in space using a finite volume formulation on a non-uniform, staggered, Cartesian grid. The grid is uniform in the x and y directions. Here, the grid cell sizes in viscous wall units are $\Delta x_0^+ = \Delta y_0^+ = 2.95$. In the z direction the grid is stretched from $\Delta z_0^+ = 0.36$ at the bottom boundary, to $\Delta z_0^+ = 2.2$ for $z = 0.4$–0.8 and then down to $\Delta z_0^+ = 0.9$ at the upper boundary. These values are based on the initial Reynolds number of the simulation. For $\lambda_0 = 2$ cases, in which the friction velocity increases by approximately 20 % during the simulation, these Δ^+ values will also increase by approximately 20 %. The number of cells in each direction depends on $Re_{\tau,0}$ and is given in table 2.

A domain with dimensions $2\pi \times \pi \times 1$ in the x, y and z directions, respectively, was used for all simulations. Williamson *et al.* (2015) present results for the heated equilibrium flow on domains of size up to $8\pi \times 4\pi \times 1$. The differences between the results on the $8\pi \times 4\pi \times 1$ and $2\pi \times \pi \times 1$ domain for the flow parameters that will be discussed in this paper were found to be negligible.

The spatial discretisation uses fourth-order central differences for the advection terms in the momentum and energy equations. The fourth-order interpolations are computed using the scheme of Hokpunna & Manhart (2010). All other terms in the momentum, energy and pressure correction equations are discretised using second-order central differences. The equations are integrated in time using a second-order accurate fractional step method. The momentum and energy equations

are integrated using a second-order hybrid Adams–Bashforth/Adams–Moulton scheme in which the diffusion terms are solved implicitly while all other terms are solved explicitly. Mass conservation is enforced using the pressure-correction method of van Kan (1986) and Bell, Colella & Glaz (1989). The time step Δt was adjusted automatically to ensure that the maximum CFL (Courant–Friedrichs–Lewy) number $(\Delta t u_i/\Delta x_i)$ in the domain remained in the range 0.18–0.2. Here Δx_i is the cell width in the direction of the velocity component u_i.

Resolution relative to the Kolmogorov scale η can be estimated for Case 3 from the plot of Kolmogorov scale given in figure 9. For this case the grid size in the x and y directions is $\Delta x = \Delta y = 5.5 \times 10^{-3}$ while in the z direction the grid varies from $\Delta z = 7 \times 10^{-4}$ at the bottom boundary, to $\Delta z = 4 \times 10^{-3}$ for $z = 0.4$–0.8 and then to $\Delta z = 1.7 \times 10^{-3}$ at the upper boundary. Vertical profiles of the Kolmogorov scale for the equilibrium and time-evolving flows for Case 3 (figure 9) show that the minimum values of η range from $\eta \approx 2.2 \times 10^{-3}$ close to the bottom boundary to $\eta \approx 4 \times 10^{-3}$ in the central region of the channel and $\eta \approx 8 \times 10^{-3}$ close to the top surface. Thus the grid cell size relative to Kolmogorov scale ranges from approximately $\Delta x/\eta = \Delta y/\eta \approx 2$ close to the bottom boundary, to $\Delta x/\eta = \Delta y/\eta \approx 1.5$ in the central region and then $\Delta x/\eta = \Delta y/\eta \approx 0.5$ close to the upper surface. In the vertical direction $\Delta z/\eta \approx 0.3$ close to the bottom boundary, $\Delta z/\eta \approx 1$ in the central region and $\Delta z/\eta \approx 0.2$ close to the upper surface. Similar ratios apply to the other cases. Since the highest Prandtl number case uses $Pr = 1$, the Batchelor scale, given by $\lambda_B = \eta/Pr^{1/2} \geqslant \eta$ for all cases. With our fourth-order spatial discretisation scheme and this degree of resolution the simulations are expected to resolve scales of motion of the order of the Kolmogorov and Batchelor scales.

To check the accuracy of the solutions Case 4 was rerun with Grid D which has spatial and temporal resolution one and a half times higher than that used for the remaining simulations. The increased resolution was found to have an indiscernible effect on the results indicating that the errors due to the numerical discretisation schemes with the grids used are negligible.

4. Overview of the flow evolution

Figures 2 and 3 show the time evolution of the temperature and vorticity fields for Case 3 for which $Re_{\tau,0} = 540$; $\lambda_0 = 2$; $Pr = 0.71$; $\alpha_0 = 8$. The temperature fields are at different scales in order to clearly show features. The vorticity field contours show the absolute value of the vorticity vector, $|\boldsymbol{\omega}|$. The initial temperature state shows that the channel is weakly stratified in the lower half of the channel and becomes progressively more strongly stratified as the upper surface is approached. In the initial state the vorticity field exhibits characteristic features of turbulent channel flow up to a height of $z \approx 0.5$, whereas in the region $z = 0.5$–0.8 the turbulence is intermittent, and the strongly stratified region above $z = 0.8$ is essentially laminar. As the flow evolves the turbulence in the flow becomes noticeably more energetic as the stratification breaks down and the temperature field mixes through the channel. In particular, the flow for $\hat{t} = 1.5$–7 contains a large number of shear instabilities that have features, such as overturns in the temperature field and braided cat's eyes in the vorticity field, that are qualitatively similar to Kelvin–Helmholtz instabilities (see Smyth & Moum 2000, for example). At the end of the flow evolution the flow returns to a less energetic state.

Figure 4 shows the buoyancy profiles for each of the initial equilibrium states. Here buoyancy is calculated as $\lambda_0\langle\phi(z) - \phi_b\rangle$, where ϕ_b is the temperature at the bottom of the channel and the angled brackets $\langle\cdot\rangle$ indicate averaging over both horizontal planes

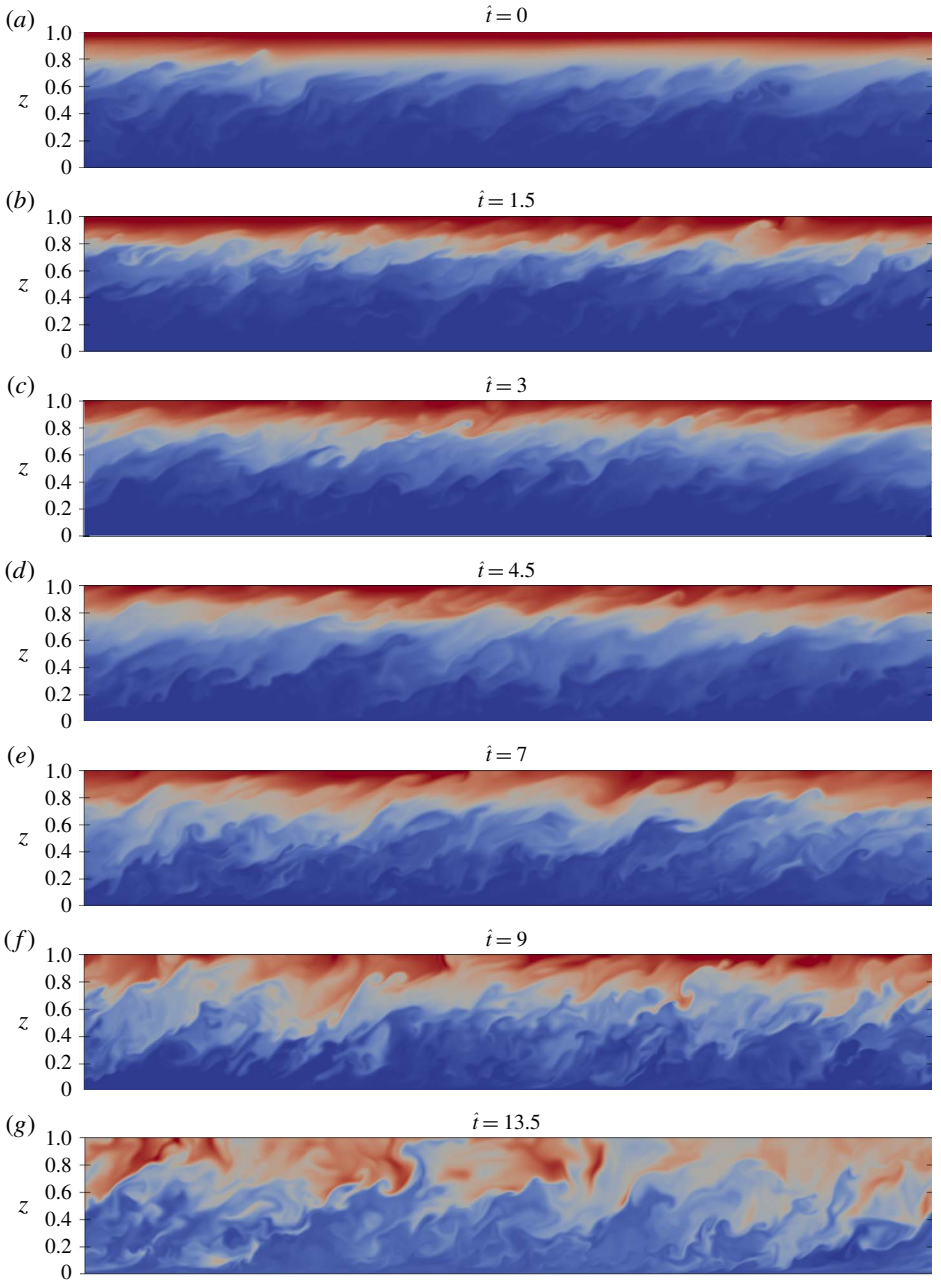

FIGURE 2. (Colour online) Evolution of the temperature field in the x–z plane during the destratification process for Case 3: $Re_{\tau,0} = 540$; $\lambda_0 = 2$; $Pr = 0.71$; $\alpha_0 = 8$. The colour scale varies in order to highlight features. Flow is from left to right.

and time. Increasing the stability parameter λ_0 of the equilibrium state increases the surface buoyancy directly via the presence of λ_0 in $\lambda_0\langle\phi - \phi_b\rangle$. It is further increased indirectly due to the increased stability. In the initial equilibrium state the radiative heat source must be balanced by the combination of turbulent and molecular heat

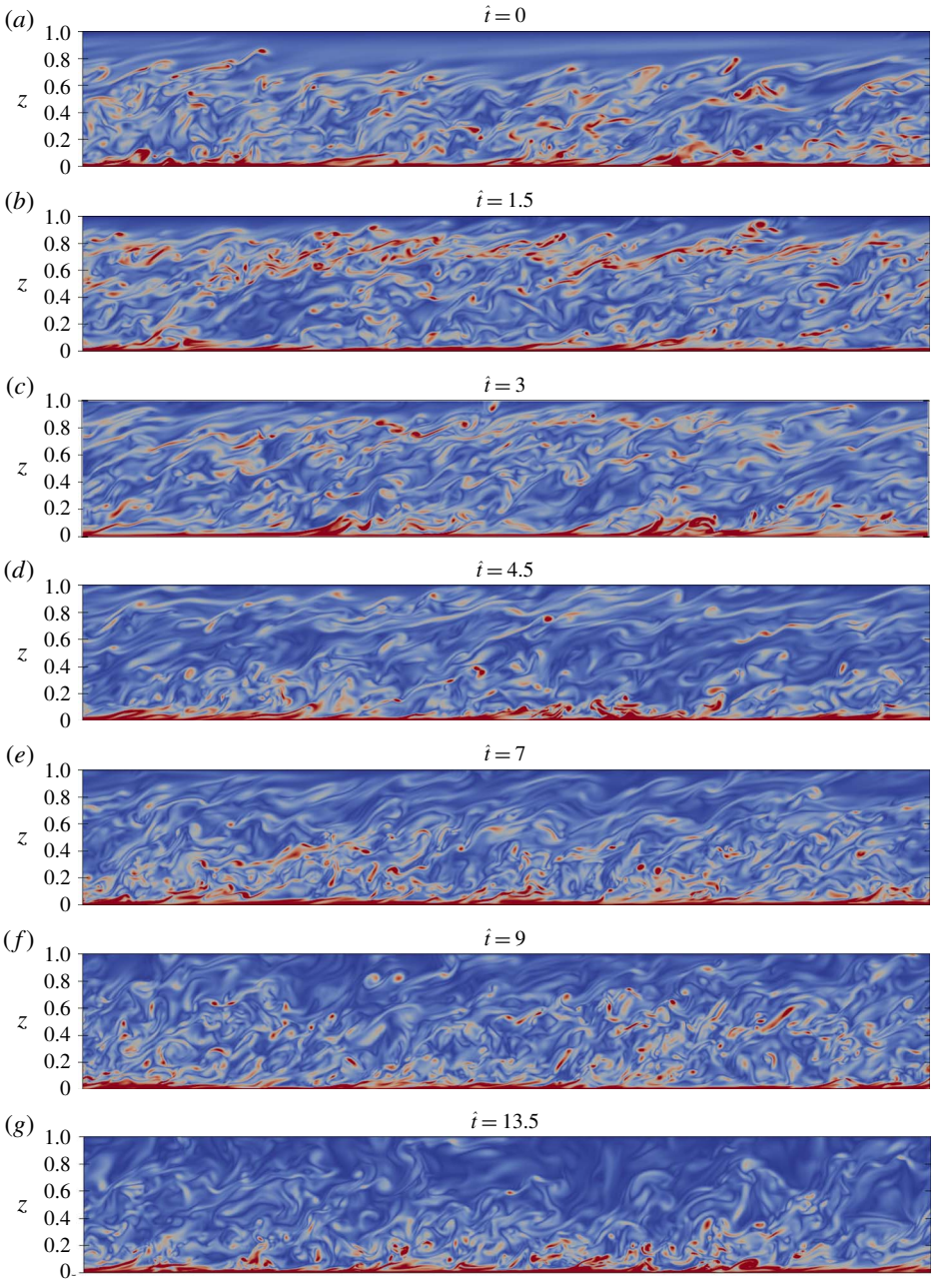

FIGURE 3. (Colour online) Evolution of the vorticity field in the $x - z$ plane during the destratification process for Case 3: $Re_{\tau,0} = 540$; $\lambda_0 = 2$; $Pr = 0.71$; $\alpha_0 = 8$. The colour scale is the same in all images. Flow is from left to right.

fluxes in order to maintain a steady state. As λ_0 increases, the turbulent heat flux in the near-surface region decreases. As a result the vertical temperature gradient must increase in order to provide the increased molecular heat flux required to balance the radiative heat source.

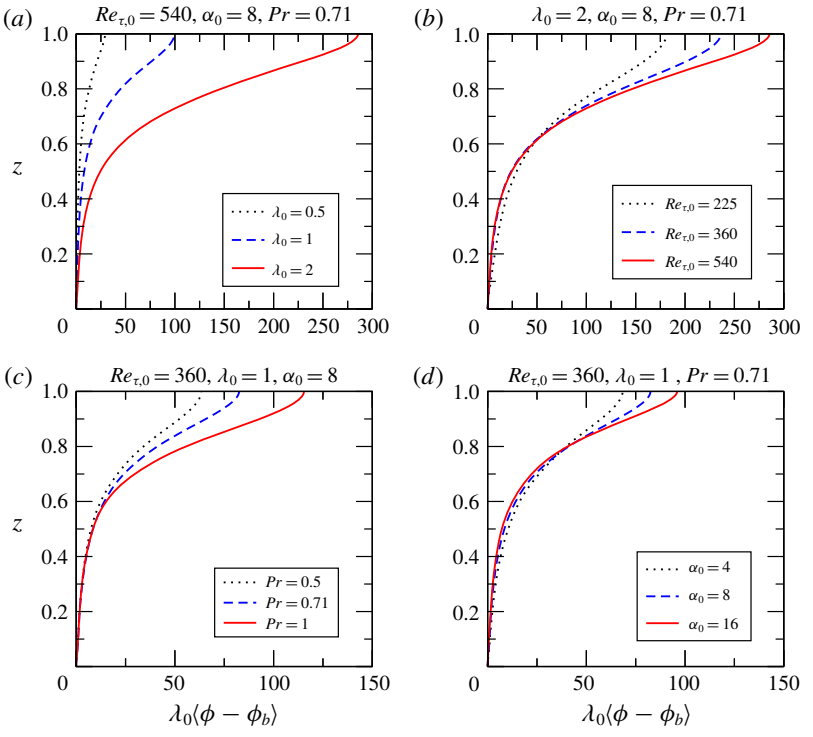

FIGURE 4. (Colour online) Equilibrium state buoyancy profiles for Cases 1–10.

Increasing Reynolds number $Re_{\tau,0}$ also increases the surface buoyancy. This can be understood by considering the case of constant $\tilde{u}_{\tau,0}$ and $\tilde{h}_0$. In this situation increasing $Re_{\tau,0}$ implies decreasing molecular diffusivity. As with the indirect effect of λ_0 above, a larger temperature gradient is then required in order to provide the necessary molecular heat flux. Increasing Pr leads directly to lower molecular diffusivity, again requiring a larger temperature gradient, and hence increasing surface buoyancy and stability.

The turbidity parameter α_0 changes the vertical distribution of the radiative heat source. As α_0 increases, the absorption of radiation close to the surface increases while less radiation is absorbed in lower layers leading to a higher temperature gradient and increased stability close to the surface.

We refer the reader to Williamson *et al.* (2015) for a detailed discussion of the turbulence characteristics of the heated equilibrium flow states.

After removal of the heat source the flow evolves over time from an initial stratified state toward a fully mixed state with a uniform temperature. Figure 5 shows this destratification process in the form of time series of the friction Richardson number Ri_τ. Clearly the initial conditions affect the time required for destratification of the channel to occur, with the time required increasing as the friction Richardson number in the initial state $Ri_{\tau,0}$ increases. In the following sections we will discuss the effect of the initial state, determined by $Re_{\tau,0}$, λ_0, Pr and α_0, as well as the governing flow parameters, Re_τ, Ri_τ and Pr on the evolution of the flow during the destratification process and the resultant effects on destratification rate.

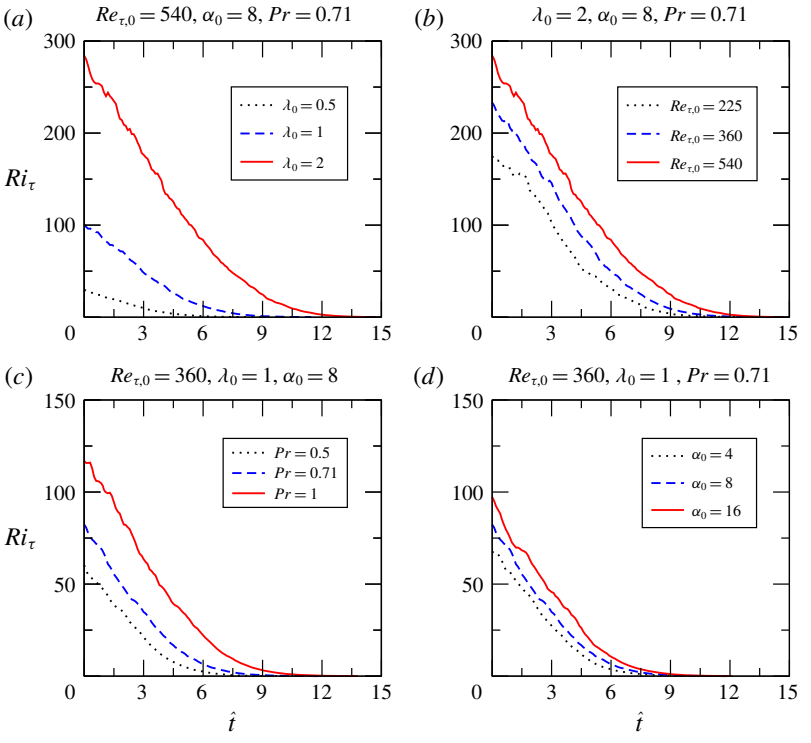

FIGURE 5. (Colour online) Value of Ri_τ as a function of time for Cases 1–10.

5. Vertical profiles

Vertical profiles showing the transient response of selected flow statistics for Case 3 ($Re_{\tau,0} = 540$; $\lambda_0 = 2$; $Pr = 0.71$; $\alpha_0 = 8$) are presented in figure 6. Statistics are shown for the initial state, and then at five times during the evolution of the flow. The times chosen correspond approximately to the flow field visualisations shown in figures 2 and 3. The statistics for the initial equilibrium state were calculated over 30 time units with realisations sampled at 0.5 time unit intervals. This was not possible for the statistics measured during the transient flow, however, in order to improve convergence of the statistics the values given in the plots were obtained by averaging over intervals of one time unit, using flow realisations sampled at intervals of 0.1 time units in addition to averaging over horizontal planes.

Panels (*a*,*b*) show $\langle \hat{u} \rangle$ and $\langle u \rangle$, the mean streamwise velocity normalised in terms of the initial friction velocity $u_{\tau,0}$, and time-varying friction velocity u_τ respectively. The former is the velocity that is actually generated in the simulation before the results are renormalised (see appendix A). Panel (*c*) shows mean temperature $\langle \phi \rangle$. Panels (*d*,*e*) show profiles of turbulent shear stress $\langle u'w' \rangle$ and turbulent heat flux $\langle \phi'w' \rangle$. Panel (*f*) shows the non-dimensional vertical eddy diffusivity,

$$k_h = \frac{-\langle \phi'w' \rangle}{\partial \langle \phi \rangle / \partial z}, \tag{5.1}$$

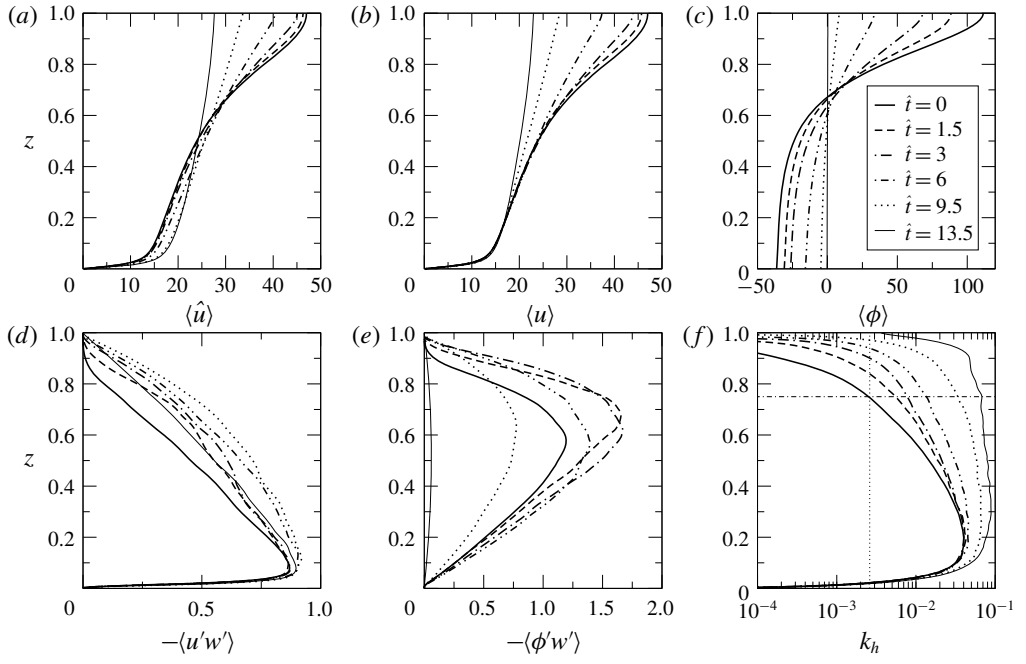

FIGURE 6. Vertical profiles showing the transient response of selected flow statistics at various times for Case 3. Here the thin dotted line corresponds to $k_h = \sigma$, while the thin dashed line corresponds to $z = 0.75$.

which is related to the dimensional eddy diffusivity,

$$\tilde{k}_h = \frac{-\langle \tilde{\phi}' \tilde{w}' \rangle}{\partial \langle \tilde{\phi} \rangle / \partial \tilde{z}}, \tag{5.2}$$

through

$$k_h = \frac{\tilde{k}_h}{\tilde{u}_\tau \tilde{h}}. \tag{5.3}$$

Here fluctuating quantities relative to the horizontal mean $\langle \cdot \rangle$ are denoted with primes, (for example w' and ϕ').

As the flow evolves, the initial temperature stratification is broken down by turbulent mixing and viscous diffusion and the system approaches a state with a uniform mean temperature of $\langle \phi \rangle = 0$, corresponding to zero total potential energy. The downwards turbulent heat flux has a maximum in the range $z = 0.5 - 0.7$. This region of low turbulent heat flux divergence corresponds to the region in which the temperature remains relatively constant at $\langle \phi \rangle = 0$ throughout the flow evolution.

In the initial state, the relatively high degree of stratification in the upper portion of the channel leads to reduced turbulent mixing in this region. This is apparent in the profiles of $\langle u'w' \rangle$, $\langle \phi'w' \rangle$ and k_h, which show a notable depression in magnitude in the near-surface region. As a result, the momentum transport required to balance the streamwise pressure gradient in this region must be provided predominantly by viscous shear, leading to a substantial increase in the mean streamwise velocity close to the surface relative to the final unstratified flow.

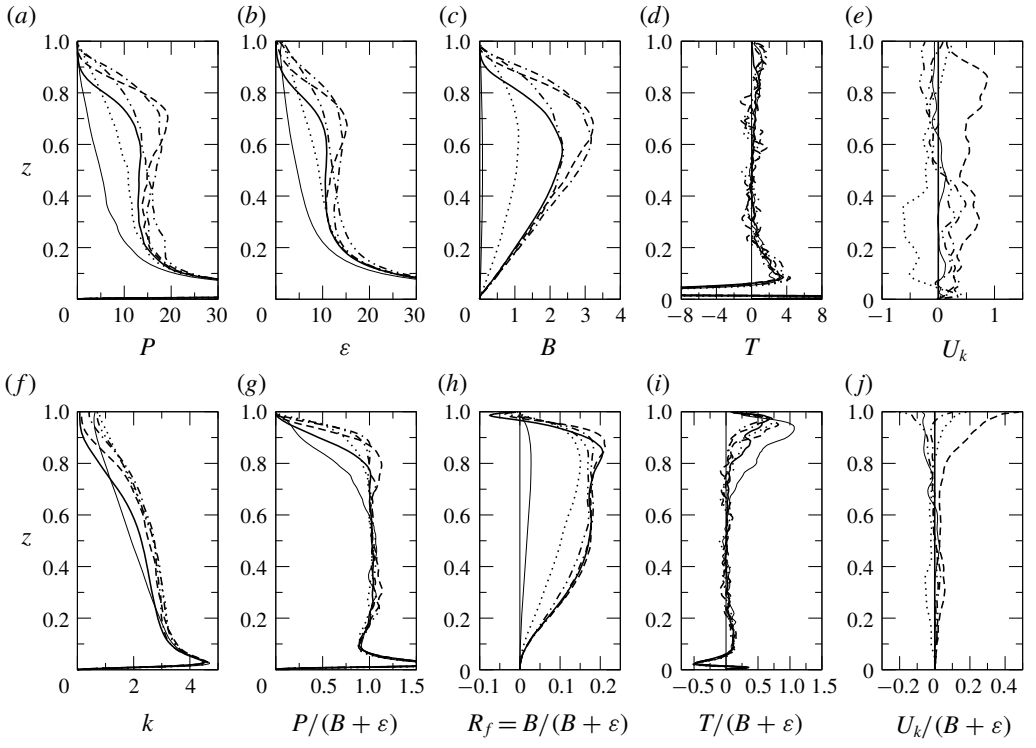

FIGURE 7. Transient response of dominant terms in the turbulent kinetic energy equation for Case 3. Legend as for figure 6.

In the early stages of the destratification process the turbulent shear stress $\langle u'w' \rangle$ increases substantially, before gradually decreasing to the neutral flow profile. As can be seen from (*a*), this change in the balance between turbulent and viscous shear leads to a redistribution of velocity over the height of the channel, with the near-surface region slowing down, while the velocity close to the bottom surface increases. It is this change that leads to the increase in the coefficient of friction C_f and friction velocity u_τ. The inflected initial velocity profile implies a surplus of mean flow kinetic energy, $K(z, \hat{t}) = 1/2\langle u \rangle^2(z, \hat{t})$, in the initial flow relative to the final state.

The turbulent heat flux $-\langle \phi' w' \rangle$ also increases substantially, particularly in the upper half of the channel before gradually decreasing again as the process proceeds. As will be discussed in detail below, $-\langle \phi' w' \rangle$ provides a pathway for conversion of mean flow kinetic energy and energy due to the pressure gradient into potential energy. The eddy diffusivity k_h increases substantially across the channel as the flow destratifies due to the increase in $-\langle \phi' w' \rangle$ relative to the mean temperature gradient.

Figure 7 show the transient response of the dominant terms in the turbulent kinetic energy equation. For this flow, which is homogeneous on $x - y$ planes, the turbulent kinetic energy equation can be written as

$$\frac{\partial k}{\partial t} = \frac{\partial}{\partial z}\left[-\frac{1}{2}\langle w' u_i' u_i' \rangle - \langle w' p' \rangle + 2\nu \langle s_{i3} u_i' \rangle\right] - \langle u' w' \rangle \frac{\partial \langle u \rangle}{\partial z} + \gamma \langle \phi' w' \rangle - 2\nu \langle s_{ij} s_{ij} \rangle, \quad (5.4)$$

where turbulent kinetic energy $k = 1/2\langle u_i' u_i' \rangle$ and s_{ij} is the strain rate due to velocity fluctuations given by

$$s_{ij} = \frac{1}{2}\left(\frac{\partial u_i'}{\partial x_j} + \frac{\partial u_j'}{\partial x_i}\right). \tag{5.5}$$

For this flow the dominant terms are the unsteady term $U_k = \partial k/\partial t$, transport due to turbulent fluctuations $T = -1/2\partial\langle w' u_i' u_i' \rangle/\partial z$, shear production $P = -\langle u'w' \rangle \partial\langle u \rangle/\partial z$, downwards buoyancy flux (or buoyancy destruction) $B = -\gamma\langle \phi' w' \rangle$ and dissipation rate $\varepsilon = 2\nu\langle s_{ij} s_{ij} \rangle$. Panels (*a–f*) show P, ε, B, T, U_k and k, while in (*g–j*) the terms P, B, T and U_k are presented as ratios of $B + \varepsilon$.

As discussed above, conversion of turbulent kinetic energy into potential energy occurs through the downward buoyancy flux $-\gamma\langle \phi' w' \rangle$ or equivalently the buoyancy destruction term B. The remainder of the turbulent kinetic energy is converted into internal energy through viscous dissipation ε. In a real flow this increase in internal energy can be viewed as raising the potential energy of the system (see Winters *et al.* 1995). The Oberbeck–Boussinesq form of the governing equations used for this study neglects the transfer of energy from viscous dissipation to internal energy, so there is no increase in temperature and hence E_p as a result of dissipation.

In the initial state, shear production, buoyancy destruction and viscous dissipation are in balance across a region from $z = 0.2$–0.8 indicating that this region is in a state of local energetic equilibrium. This balance can be seen most clearly in the profile of $P/(B + \varepsilon)$ which is approximately equal to one in this region implying $P \approx B + \varepsilon$.

Sudden removal of the radiative heat source, or potential energy sink, at the start of the transient simulation leads to a step change in the energy balance within the channel, resulting in a rapid increase in turbulent kinetic energy, particularly in the near-surface region, during the initial stage of the flow evolution ($\hat{t} = 0$–3). Turbulent kinetic energy then remains relatively constant at this elevated state over the period $\hat{t} = 3$–9.5 before decreasing again towards neutral conditions in the late stages of the process. The rapid increase in k during $\hat{t} = 0$–3 is reflected in the profile of the unsteady term U_k at $\hat{t} = 1.5$ shown in (*e*), which reaches a maximum value of approximately 0.75 at this time before returning to values close to zero for the remainder of the flow evolution. As seen from the profile of $U_k/(B + \varepsilon)$ in (*j*), in the central region of the channel even this maximum value is small relative to other terms.

The dominant budget terms, P, ε and B, in the central and upper part of the channel also increase during the initial period ($\hat{t} = 1.5$) as shown in (*a–c*). The profile of $P/(B + \varepsilon)$ in (*g*) shows a distinct increase above the value of 1 for $z = 0.75$–0.9 indicating a surplus of shear production in this region, which accounts for the significant U_k at this time. This shear production can be seen as a distinct band of high vorticity in the flow field visualisations shown in figure 3. By $\hat{t} = 3$, local energetic equilibrium has been restored and the local equilibrium region $P/(B + \varepsilon) \approx 1$ has extended up to approximately $z = 0.9$. The region $z = 0.2$–0.9 then remains in local equilibrium until $\hat{t} \approx 8$ (see § 8) after which the extent gradually starts to decrease as turbulent transport T starts to dominate above $z = 0.7$.

Thus, when the radiative heat source is removed, the flow 'relaxes' rapidly into a new state in which the laminar surface layer becomes turbulent and the region of energetic equilibrium extends up close to the surface. This new state is reached very early in the destratification process (by $\hat{t} = 3$ for Case 3). The fact that a large portion of the flow remains in local equilibrium for most of the flow evolution implies that local turbulent fluxes should be a function of global gradients in these regions. This is explored further below.

The normalised buoyancy flux $B/(B+\varepsilon)$ shown in figure 7(*h*) is equivalent to the generalised form of the flux Richardson number defined by Ivey & Imberger (1991) as

$$R_f = B/(B+\varepsilon). \tag{5.6}$$

Ivey & Imberger (1991) interpret this as the ratio of the rate of conversion of turbulent kinetic energy k into background potential energy E_b, to the rate at which net mechanical energy is being made available for turbulence generation. As such it is often considered to represent the local mixing efficiency. Venayagamoorthy & Koseff (2016) point out, however, that this definition does not correctly account for the effect of counter-gradient fluxes that occur in strongly stratified flows. An example of this can be seen in (*h*), which shows that R_f is negative in the strongly stratified region close to the surface in the early stages of the flow evolution. When the flow is in local equilibrium, R_f is equal to the standard form of the flux Richardson number, defined as the ratio of buoyancy destruction to shear production, that is

$$Ri_f = B/P. \tag{5.7}$$

The profiles of R_f show a number of distinct regions. In the initial equilibrium state R_f is approximately constant over the range $z = 0.4$–0.75, with a value $R_f \approx 0.17$. This value of R_f persists until the late stages of the flow evolution and is similar to the critical value $R_{f,c} \approx 0.18$–0.2 estimated from experimental measurements by Britter (1974) and the theoretically derived value of $R_{f,c} \sim 0.15$ determined by Ellison (1957). Thus we consider $R_{f,c} = 0.17$ to represent the critical value for our flow. In this central region, vertical turbulent motions are constrained predominantly by the buoyancy length scale, l_b, so that turbulent fluxes are unaffected by height z. This corresponds to the 'z-less' scaling regime in Monin–Obukhov theory.

In the region close to the bottom wall, proximity to the solid boundary places an additional spatial constraint on turbulent motions, so that turbulent fluxes become a function of both l_b and z. This can be seen in the profiles. In the equilibrium state and for times up to $\hat{t} = 6$, R_f decreases approximately linearly with z for $z < 0.4$. For later times the region affected by z expands upwards. As the flow destratifies, l_b increases and its constraining effect on turbulent motions decreases accordingly. As a result, the region in which z is the dominant length scale expands. (Please note that in the discussion above we have used l_b to denote a generic buoyancy length scale. We will provide more precise definitions of a number of buoyancy length scales below.)

In the equilibrium state, in the region $z = 0.75$–0.85, R_f increases to a peak of $R_f \approx 0.2$. As can be seen from figure 6, this is the region where both velocity shear and temperature gradient are highest. Visualisations of the equilibrium state flow fields in (*a*) of figures 2 and 3 show that this region contains isolated incursions by shear instabilities resembling Kelvin–Helmholtz billows. A similar peak of $R_f \approx 0.21$ is seen in the profile at $\hat{t} = 1.5$. In this case it is slightly higher at $z = 0.9$. At this time figures 2 and 3 show the presence of an intense layer of shear instabilities for $z = 0.75$–0.85 with incursions up to $z = 0.9$. By $\hat{t} = 3$ the peak in R_f is very small and the visualisations show vorticity extending to the upper surface of the channel, and for all later times the peak has disappeared. Winters *et al.* (1995) found that pure Kelvin–Helmholtz (K–H) instabilities lead to a significant increase in R_f. Thus the peak in R_f seen in the early stages of our flow can be attributed to incursions by Kelvin–Helmholtz-like instabilities occurring at the intermittency boundary between the turbulent flow in the body of the channel and laminar surface layer.

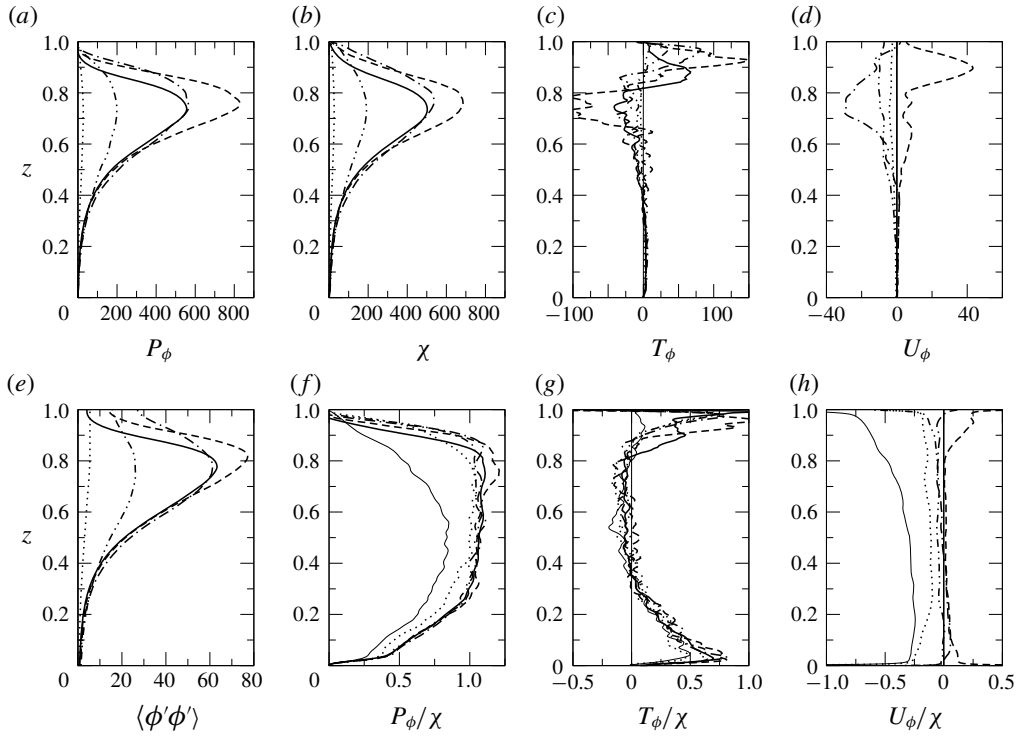

FIGURE 8. Transient response of dominant terms in the temperature variance equation for Case 3. Legend as for figure 6.

Figure 8 shows the transient response of dominant terms in the temperature variance equation for Case 3. For our flow the temperature variance equation can be written as

$$\frac{\partial\langle\phi'^2\rangle}{\partial t} = \frac{\partial}{\partial z}\left[-\langle w'\phi'^2\rangle + \sigma\frac{\partial\langle\phi'^2\rangle}{\partial z}\right] - 2\langle\phi' w'\rangle\frac{\partial\langle\phi\rangle}{\partial z} - 2\sigma\left\langle\frac{\partial\phi'}{\partial x_j}\frac{\partial\phi'}{\partial x_j}\right\rangle. \tag{5.8}$$

Similar to the turbulent kinetic energy equation, for this flow the dominant terms are the unsteady term $U_\phi = \partial\langle\phi'^2\rangle/\partial t$, turbulent transport $T_\phi = -\partial\langle w'\phi'^2\rangle/\partial z$, production $P_\phi = -2\langle\phi' w'\rangle\partial\langle\phi\rangle/\partial z$ and dissipation rate $\chi = 2\sigma\langle(\partial\phi'/\partial x_j)^2\rangle$. Panels (*a–e*) show P_ϕ, χ, T_ϕ, U_ϕ and $\langle\phi'^2\rangle$, while in (*f–h*) the terms P_ϕ, T_ϕ and U_ϕ are presented as ratios of χ.

As with the turbulent kinetic energy, a rapid increase in temperature variance $\langle\phi'^2\rangle$ is seen during the initial stage ($\hat{t} = 0$–3) particularly in the near-surface region as this region transitions from a laminar to a turbulent state. This is reflected in a region of positive U_ϕ in the upper half of the channel at $\hat{t} = 1.5$. This burst of activity is short-lived, however, with the peak $\langle\phi'^2\rangle$ decreasing substantially by $\hat{t} = 3$ and a corresponding negative U_ϕ at this time. After $\hat{t} = 3$ the temperature variance decreases progressively until it is essentially zero at the end of the destratification process. Unlike turbulent kinetic energy, with adiabatic boundaries and no internal heat source, the only source of production of temperature variance is the internal temperature gradient. As the flow destratifies this temperature gradient decays leading to a decay

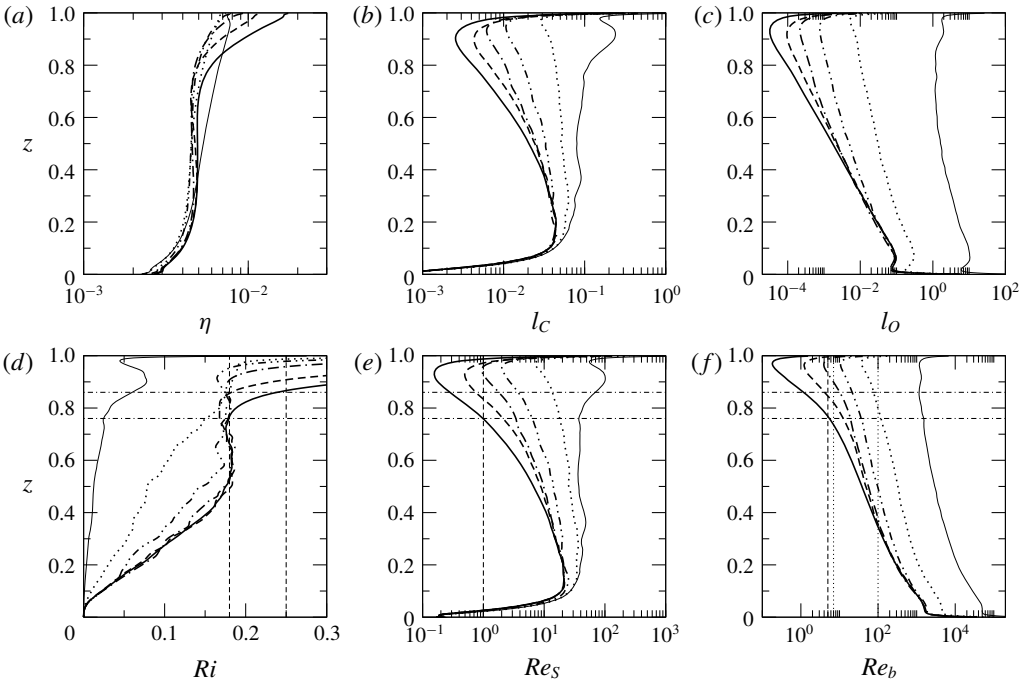

FIGURE 9. Transient response of turbulent length scales and related parameters for Case 3. Legend as for figure 6. (*d*) The thin dashed lines correspond to $Ri = 0.18$ and $Ri = 1/4$. (*e*) The thin dashed line corresponds to $Re_S = 1$. (*f*) The thin dashed line corresponds to $Re_b = 5$, while the two thin dotted lines correspond to $Re_b = 7$ and $Re_b = 100$. The thin dot-dashed lines (*d–f*) correspond to $z = 0.76$ and $z = 0.86$.

in the production term P_ϕ. Throughout the process there is turbulent transport T_ϕ out of the central region of the channel and into the near-wall and near-surface regions.

During the period up to $\hat{t} = 9.5$ the production and dissipation terms remain in balance so that $P_\phi/\chi \approx 1$ over the region $z = 0.25$–0.9, similar to that seen for the turbulent kinetic energy budget terms. This is somewhat surprising considering the decay in $\langle\phi'^2\rangle$; however, P_ϕ and χ remain large in comparison with T_ϕ and U_ϕ during this period so the decay in $\langle\phi'^2\rangle$ is due to a relatively small difference in two large terms. In the late stages of the process this local equilibrium is lost as dissipation exceeds production, $\chi > P_\phi$.

Figure 9 shows profiles of turbulence length scales and some non-dimensional parameters that can be written in terms of these length scales. Panels (*a–c*) show: the Kolmogorov scale η, the Corrsin scale l_C, and the Ozmidov scale l_O, which are defined as

$$\eta = \left(\frac{\nu^3}{\varepsilon}\right)^{1/4}, \quad l_C = \left(\frac{\varepsilon}{S^3}\right)^{1/2}, \quad l_O = \left(\frac{\varepsilon}{N^3}\right)^{1/2}. \tag{5.9a–c}$$

The Kolmogorov scale characterises the smallest scales of turbulence, while the Corrsin scale is indicative of the scale above which turbulence is affected by background shear, and the Ozmidov scale, the scale above which turbulence is affected by buoyancy.

Panel (*d*) shows the gradient Richardson number

$$Ri = N^2/S^2, \tag{5.10}$$

where the buoyancy frequency N is given by $N^2 = \gamma\,\partial\langle\phi\rangle/\partial z$, and mean vertical shear, $S = \partial\langle u\rangle/\partial z$. Panel (*e*) shows the shear Reynolds number (see Chung & Matheou 2012),

$$Re_S = \frac{\varepsilon}{\nu S^2}, \tag{5.11}$$

and panel (*f*) the local buoyancy Reynolds number (see Gargett, Osborn & Nasmyth 1984; Smyth & Moum 2000),

$$Re_b = \frac{\varepsilon}{\nu N^2}. \tag{5.12}$$

As discussed by Brethouwer *et al.* (2007) and Chung & Matheou (2012), it is useful to interpret these three non-dimensional parameters as ratios of turbulence length scales, that is,

$$Ri = \left(\frac{l_C}{l_O}\right)^{4/3}, \quad Re_S = \left(\frac{l_C}{\eta}\right)^{4/3}, \quad Re_b = \left(\frac{l_O}{\eta}\right)^{4/3}. \tag{5.13a–c}$$

Typically $l_O > l_C > \eta$, thus Ri represents the degree of separation between the smallest scales affected by background shear and the smallest scales affected by buoyancy, while Re_S represents the degree of separation between the smallest scales affected by shear and the smallest scales of motion, and Re_b the separation between the smallest scales affected by buoyancy and the smallest scales of motion.

Shih *et al.* (2005) define three regimes for Re_b in stably stratified turbulent shear flows: a diffusive regime for $Re_b < 7$ in which turbulence is strongly damped and $k_h/\nu < 1$, an intermediate regime $7 < Re_b < 100$ in which k_h/ν is related linearly to Re_b, that is $k_h/\nu = 0.2Re_b$, and an energetic regime $Re_b > 100$ in which the effects of stratification become progressively weaker as Re_b increases and k_h/ν approaches its neutral flow value.

Profiles of Re_b in figure 9 show that Re_b decreases with increasing z. This is seen to be due primarily to a decrease in l_O as a result of increasing buoyancy frequency with height. In the initial state, Re_b covers all three regions described above, with the energetic regime seen for $z = 0$–0.35, the intermediate regime for $z \approx 0.35$–0.75 and the diffusive regime for $z > 0.75$. As can be seen from the profile of k_h in figure 6, the region above $z = 0.75$ also corresponds to the region in which $k_h < \sigma$ in our flow.

The initial state profile for Ri also shows three distinct regimes spanning three regions across the channel in a manner similar to that seen for the flux Richardson number, R_f. For $z = 0$–0.5, Ri increases from $Ri = 0$ at the wall to a value of $Ri \approx 0.18$. For $z = 0.5$–0.76, Ri is approximately constant at what appears to be a critical value of $Ri_c \approx 0.18$. Above $z = 0.76$, Ri increases significantly.

Comparable values of Ri_c for flows similar to the central region of our channel are reported by other authors. Based on simulations of stratified channel flow with the stratification maintained by constant density boundary conditions at the top and bottom surfaces, Garcia-Villalba & del Alamo (2011) estimated $Ri_c \approx 0.2$. For stationary homogeneous stratified sheared turbulence, Shih *et al.* (2000) estimated $Ri_c \approx 0.2$ while Chung & Matheou (2012) give $Ri_c \approx 0.17$. For stratified plane Couette flow, Zhou, Taylor & Caulfield (2017) found the critical value of Ri_c to

be 0.21, which is approached as the ratio of the channel height to Monin–Obukhov length scale approaches zero.

While the central region of our flow is similar to the flows listed above, the near-surface region is quite different. Here we have a strongly stratified layer that is essentially laminar and separated from the solid lower wall by a turbulent boundary layer. In the near-surface region the mean velocity and temperature profiles (see figure 6) contain an inflection and hence are similar to the canonical conditions under which Kelvin–Helmholtz and Holmboe instabilities form. Howland, Taylor & Caulfield (2018) investigated marginal stability associated with the formation of K–H waves from laminar initial conditions and showed the marginal stability limit to be $Ri_m = 1/4$. In fact Kaminski, Caulfield & Taylor (2017) have shown that Kelvin–Helmholtz-like billows can form for Ri up to 0.4 in the presence of perturbations that are sufficiently large and that have the optimal structure for amplification.

Figure 9(*e*) shows that, in the equilibrium state, $Re_S < 1$ for $z > 0.76$, which also corresponds to the height for which $Ri > 0.18$. $Re_S < 1$ implies $l_C < \eta$, so this is a reasonable criterion by which to define what we will refer to as 'laminar flow'. As seen in the profile of k_h in figure 6, this is also very close to the point at which $k_h = \sigma$. Given that we have laminar flow above $z = 0.76$, we would expect the critical Richardson number to be close to the marginal stability limit, $Ri_m = 1/4$; however, as seen in figure 9(*d*,*e*), we have a region of laminar flow ($Re_S < 1$) for $0.76 < z < 0.86$, in which $0.18 < Ri < 1/4$.

This apparent inconsistency between our results and the theoretical analysis of Howland *et al.* (2018) gives a clue to the mechanism underlying the 'relaxation' process that we have suggested occurs in the initial stages of the evolution of our flow. An important point of difference between conditions in the near-surface region of our equilibrium state flow and those in the analysis of Howland *et al.* (2018) is that our flow is subject to a volumetric heat source that decays exponentially with distance from the upper surface and so acts as a potential energy sink. As a result, small temperature perturbations that are linearly unstable and would grow into nonlinear instabilities in the unheated flow, are absorbed by the potential energy sink before they are able to do so. This has the effect of depressing the Richardson number stability limit so that a region of the flow that would be unstable with no heat source is in fact stable. When the heat source is removed, however, conditions in the region $z = 0.76$–0.86 suddenly become conducive to the formation and growth of shear instabilities.

Evidence for this can be clearly seen in the visualisations of temperature and vorticity fields at $\hat{t} = 1.5$ in (*b*) of figures 2 and 3, which show a proliferation of the distinctive temperature overturns and braided cat's eye vorticity structures characteristic of K–H waves. These Kelvin–Helmholtz-like structures can be seen (albeit with weaker intensity) in the images up to $\hat{t} = 7$. The burst of activity during the initial relaxation period is also evident in the sudden increase in the production of kinetic energy P and temperature variance P_ϕ at $\hat{t} = 1.5$ seen in this region in figures 7 and 8. The result is a rapid transition of this region to turbulent flow with $P > B + \varepsilon$ and $P_\phi > \chi$ at this time as was discussed above.

The intense activity also results in rapid mixing as is evident from the sudden increase in B at $\hat{t} = 1.5$. This mixing expands the region in which $Ri < Ri_m$ so that, by $\hat{t} = 3$, $Ri < Ri_m$ for $z < 0.95$. The region of turbulent flow expands in line with this with Re_S reaching a minimum of $Re_S = 1$ at $z = 0.95$ at $\hat{t} = 3$. For $\hat{t} > 3$, $Re_S > 1$ up to the top of the channel and we consider the initial relaxation period and transition of the near-surface region to turbulent flow to be complete.

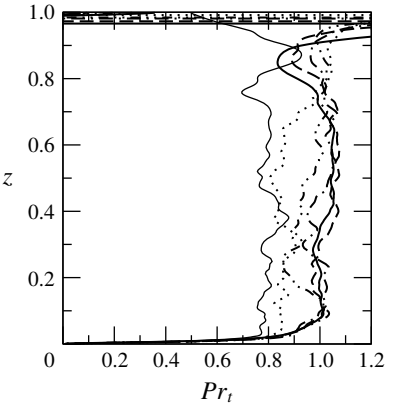

FIGURE 10. Transient response of turbulent Prandtl number for Case 3. Legend as for figure 6.

Kelvin–Helmholtz instabilities are a classic example of energy transfers in sheared stratified flows and have been used extensively as a canonical flow to study the energetics of mixing processes in this context (see Winters *et al.* 1995; Caulfield & Peltier 2000; Salehipour & Peltier 2015; Kaminski *et al.* 2017; Howland *et al.* 2018, for example). These studies typically use mathematically prescribed initial mean vertical velocity and temperature profiles, and apply artificial perturbations in order to catalyse the formation of the K–H instability. The time evolution of the resulting flow is then studied using stability analysis or numerical simulation.

Our flow is an example of a real flow in which an analogous situation occurs. The equilibrium state is stabilised by the internal heat source, generating a laminar near-surface region with velocity and temperature profiles determined by the mathematical form of heat source. A wide spectrum of 'natural' perturbations are supplied by the turbulence in the lower regions of the channel. Sudden removal of the heat source then allows these perturbations to grow and become unstable where conditions for instability exist.

The energy transfers from mean flow kinetic energy to available potential energy and then to background potential energy described in studies such as those of Winters *et al.* (1995) and Caulfield & Peltier (2000) also occur in the near-surface region of our flow. Our flow is more complicated, however, because the initial conditions in the central and lower regions of the channel are turbulent, so that turbulent kinetic energy generated at the lower boundary also takes part in the energy transfer process. This will be discussed further in § 6.

Figure 10 shows evolution of the turbulent Prandtl number,

$$Pr_t = \frac{k_m}{k_h}, \tag{5.14}$$

where the vertical eddy viscosity k_m is calculated as

$$k_m = -\frac{\langle u'w' \rangle}{\partial \langle u \rangle / \partial z}. \tag{5.15}$$

Garcia-Villalba & del Alamo (2011) found that $Ri_f \approx Ri$ in the regions of their stably stratified channel flow for which $Ri < Ri_c$. This implies that the turbulent Prandtl

number $Pr_t = Ri/Ri_f \approx 1$. Our simulations give similar behaviour, with $Pr_t \approx 1$ in the region from $z = 0.1$ to 0.8 in the initial equilibrium state, with the range extending up to $z = 0.95$ as the flow in the near-surface layer becomes turbulent in response to removal of the heat source. As the flow approaches the neutral state, Pr_t decreases towards a neutral value of $Pr_t \approx 0.8$, which is similar to the value $Pr_t \approx 0.74$ estimated by Chung & Matheou (2012).

6. Bulk flow energetics

This section presents results for bulk energy transfers within the flow. In the following, all parameters are plotted at time intervals of $\Delta\hat{t} = 0.1$ with the values of parameters calculated by averaging over horizontal planes only (not time). Here, and throughout this paper, an overline $\overline{\cdot}$ will be used to indicate this type of averaging. When used in this context, primes indicate fluctuations relative to this type of mean.

While non-dimensionalising in terms of the time-varying friction velocity u_τ is useful when discussing scalings between non-dimensional parameters, in the context of a discussion of the actual time evolution of the flow it is more useful to present results in terms of dependent variables non-dimensionalised in terms of the initial friction velocity $u_{\tau,0}$. In this form, the results can be related directly to the changes in a physical flow subject to the same boundary conditions. As described in appendix A, variables non-dimensionalised in terms of $u_{\tau,0}$ are denoted with a hat $\hat{\cdot}$.

As discussed above, the destratification process can be viewed as a transfer of energy from mean flow kinetic energy to potential energy via buoyancy fluxes. The evolution equation for total potential energy E_p is

$$\frac{\mathrm{d}E_p}{\mathrm{d}\hat{t}} = \mathcal{B}(\hat{t}) + \mathcal{M}(\hat{t}), \tag{6.1}$$

where the domain-averaged total potential energy is calculated as

$$E_p(\hat{t}) = -\frac{1}{V}\int_V \hat{\gamma}\hat{\phi}(\boldsymbol{x}, \hat{t}) z \,\mathrm{d}V, \tag{6.2}$$

and the domain-averaged turbulent and molecular buoyancy fluxes are

$$\mathcal{B}(\hat{t}) = -\frac{1}{h}\int_0^h \hat{\gamma}\overline{\hat{\phi}'\hat{w}'}\,\mathrm{d}z \quad \text{and} \quad \mathcal{M}(\hat{t}) = \frac{1}{h}\int_0^h \hat{\gamma}\frac{\partial\overline{\hat{\phi}}}{\partial z}\,\mathrm{d}z. \tag{6.3a,b}$$

Here V is the domain volume. For consistency with the previous definition of B these fluxes are positive downwards, so that a positive flux is associated with an increase in potential energy. The total potential energy that has been transferred by each of these fluxes by a particular time is then given by

$$\mathcal{B}^*(\hat{t}) = \int_0^{\hat{t}} \mathcal{B}(\hat{t}^*)\,\mathrm{d}\hat{t}^* \quad \text{and} \quad \mathcal{M}^*(\hat{t}) = \int_0^{\hat{t}} \mathcal{M}(\hat{t}^*)\,\mathrm{d}\hat{t}^*. \tag{6.4a,b}$$

Figure 11(*a*) shows the change in total potential energy ΔE_p over time relative to the initial conditions, plotted alongside $\mathcal{B}^*$ and $\mathcal{M}^*$. Also shown is the sum of these two fluxes, $\mathcal{B}^* + \mathcal{M}^*$. Potential energy E_p increases over the duration of the simulation, with the most rapid change occurring early in the simulation and very little change after $\hat{t} = 9$. It is balanced by the sum of the buoyancy fluxes $\mathcal{B}^* + \mathcal{M}^*$. While turbulent

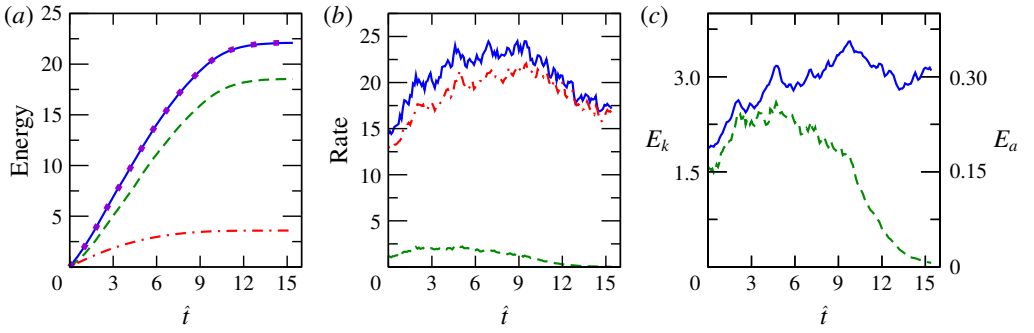

FIGURE 11. (Colour online) Domain-averaged components of the turbulent energy transfer system for Case 3 as functions of time. (*a*) Shows: ΔE_p (blue solid line), $\mathcal{B}^*$ (green dashed line), $\mathcal{M}^*$ (red dot-dashed line) and $\mathcal{B}^* + \mathcal{M}^*$ (violet dotted line). (*b*) Shows: $\mathcal{P}$ (blue solid line), $\mathcal{B}$ (green dashed line) and $\mathcal{E}$ (red dot-dashed line). (*c*) Shows: E_k (blue solid line) and E_a (green dashed line). Please note the alternate axis for E_a in this plot.

buoyancy flux $\mathcal{B}$ dominates this energy transfer, the molecular buoyancy flux $\mathcal{M}$ also plays a significant role, contributing approximately 15 % of the total flux for this case.

Shear production provides the pathway for transfer of energy from the mean flow field into the turbulent flow field. Within the turbulent flow field, turbulent kinetic energy is transferred to potential energy via buoyancy fluxes and to internal energy via turbulent dissipation. Figure 11(*b*) shows domain-averaged production, $\mathcal{P}$, turbulent buoyancy flux $\mathcal{B}$, and viscous dissipation $\mathcal{E}$, where

$$\mathcal{P} = -\frac{1}{h}\int_0^h \overline{\hat{u}'\hat{w}'}\frac{\partial \bar{\hat{u}}}{\partial z}\,\mathrm{d}z \quad \text{and} \quad \mathcal{E}(\hat{t}) = \frac{1}{h}\int_0^h 2\hat{\nu}\overline{\hat{s}_{ij}\hat{s}_{ij}}\,\mathrm{d}z. \tag{6.5a,b}$$

The energy transfer rates shown reflect the activity of shear instabilities discussed in § 5. Shear production $\mathcal{P}$ increases rapidly over the initial relaxation period, $\hat{t} = 0$–3, in which there is rapid formation of shear instabilities in the near-surface region. It then continues to increase gradually until $\hat{t} = 9$, after which it decreases back to a level similar to its initial value. The time $\hat{t} = 9$ corresponds approximately to the time when shear instabilities become noticeably less prevalent in the visualisations. These trends are mirrored by the buoyancy flux $\mathcal{B}$ and dissipation $\mathcal{E}$. In the final state $\mathcal{B}$ is close to zero and $\mathcal{P} \approx \mathcal{E}$.

Available potential energy, E_a, is the potential energy change due to adiabatic or reversible mixing and, as such, is the component of potential energy that could be transferred back into kinetic energy (Lorenz 1955). This is in contrast to background potential energy E_b, which is generated as the result of irreversible diabatic mixing. Winters *et al.* (1995) define E_b as the minimum potential energy that can be achieved as the result of an adiabatic redistribution of the density or, in our case, temperature field. For a redistributed temperature field $\hat{\phi}(z_*)$, where $z_*(\boldsymbol{x}, \hat{t})$ is the height in the redistributed state of the fluid parcel at $(\boldsymbol{x}, \hat{t})$, the domain-averaged background potential energy is given by

$$E_b = -\frac{1}{V}\int_V \hat{\gamma}\hat{\phi}z_*(\boldsymbol{x}, \hat{t})\,\mathrm{d}V. \tag{6.6}$$

E_a is then determined from the identity

$$E_a = E_p - E_b. \tag{6.7}$$

Available potential energy E_a is shown in (*c*). In the initial state E_a is small but positive due to turbulent fluctuations of the temperature field as well as mild overturns in the shear layer at $z \approx 0.8$ as can be seen in figures 2 and 3. In the early stages of the flow, E_a increases rapidly to a peak at $\hat{t} \approx 2$ and then remains relatively constant until $\hat{t} \approx 6$ after which it decreases over the remainder of the process to a final value of approximately zero. Thus the peak in E_a coincides with the initial relaxation period ($\hat{t} = 0$–3), which, as discussed above, is characterised by destabilisation of the near-surface region through the formation of K–H-like instabilities, while the sudden increase in the rate of decay at $\hat{t} = 9$ corresponds to the time at which these instabilities disappear from the visualisations.

Studies of Kelvin–Helmholtz instabilities (see Winters *et al.* 1995, for example) have shown that they lead to a similar time response for E_a as the initial overturn lifts heavier fluid adiabatically, before the subsequent breakdown of this structure generates smaller scale motions that drive irreversible mixing. In our flow E_a remains relatively small compared with the overall change in E_p. This indicates that most of the reversible buoyancy flux is rapidly transferred to E_b via irreversible mixing due to interaction with turbulent eddies from the turbulent region of the channel below. Similar small values of E_a relative to ΔE_p have been observed by Brucker & Sarkar (2007) and Kaminski & Smyth (2019) in studies of shear instabilities in initially turbulent flows.

Domain-averaged turbulent kinetic energy E_k, also shown in (*c*), shows a rapid increase during $\hat{t} = 0$–5 after which it remains relatively constant. The higher levels of turbulent kinetic energy, E_k and available potential energy E_a during the early periods of the flow evolution provide an intermediate stage in the transfer of energy from mean flow kinetic energy, E_K, to background potential energy E_b.

7. Relationships between local flow parameters in the central region

In this section we return to the relationships between local flow parameters, with a focus on the central region of the channel ($z = 0.3$–0.7). As with the previous section, all parameters are plotted at time intervals of $\Delta\hat{t} = 0.1$ with the values of parameters calculated by averaging over horizontal planes only.

As discussed above, in this paper the eddy diffusivity k_h was calculated as the ratio of turbulent temperature flux to the vertical gradient of mean temperature (5.2). A number of alternative models for eddy diffusivity are commonly used. These include the models of Osborn & Cox (1972) and Osborn (1980), which were derived in the context of oceanographic studies as a means of estimating k_h from measurements of dissipation rates of turbulent kinetic energy and temperature variance respectively, and allow k_h to be estimated when the turbulent flux is not known. Ivey, Winters & Koseff (2008) refer to the formulation for k_h given in (5.2) as the 'direct' approach, and those of Osborn & Cox (1972) and Osborn (1980) as 'indirect' approaches. We give a brief outline of these two models below.

The model of Osborn (1980) is derived by assuming local energetic equilibrium, $P = B + \varepsilon$, and approximating the buoyancy flux as $B = R_f/(1 - R_f)\varepsilon$. Combining this with (5.12) gives

$$k_h/\nu = \frac{R_f}{1 - R_f} Re_b = \Gamma Re_b, \tag{7.1}$$

where $\Gamma = R_f/(1-R_f)$. Using a critical value for the flux Richardson number of $R_{f,c} = 0.17$, this gives an upper limit for Γ of $\Gamma = 0.2$. Thus an upper limit for k_h can be estimated based on measurements of ε and N. We will follow the common practice of referring to the 'Osborn model' as (7.1) with $\Gamma = 0.2$.

The model of Osborn & Cox (1972) is derived from the temperature variance equation. Assuming local equilibrium in temperature variance, that is, $P_\phi = \chi$, leads to

$$k_h/\nu = \frac{\chi}{2\nu(\partial\overline{\phi}/\partial z)^2}. \tag{7.2}$$

Winters *et al.* (1995) note that none of these models differentiate between reversible and irreversible mixing. To address this, Winters & D'Asaro (1996) proposed a new model using an isoscalar coordinate system that calculates the diffusivity associated only with irreversible mixing. This concept was extended by Caulfield & Peltier (2000), who defined a related irreversible mixing efficiency. Salehipour & Peltier (2015) recast the diascalar diffusivity of Winters & D'Asaro (1996) into what they refer to as an 'Osborn-like' expression that is equivalent but easier to compute. They then compared the eddy diffusivity calculated according to the direct model (5.2), as well as the Osborn (7.1) and Osborn–Cox (7.2) models, to their diascalar diffusivity for data generated by DNS of inhomogeneously stratified sheared turbulence. Amongst these models, they found the eddy-diffusivity calculated by the Osborn–Cox model to be closest to the diascalar diffusivity.

Recently Ivey, Bluteau & Jones (2018) combined the Osborn and Osborn–Cox models to derive a model to estimate the flux Richardson number,

$$R_f = \frac{1}{1+D}, \tag{7.3}$$

where the dimensionless 'length scale ratio' parameter D is given by

$$D = \frac{2(\partial\overline{\phi}/\partial z)^2\varepsilon}{N^2\chi}. \tag{7.4}$$

This model assumes that $P_\phi = \chi$, the flow is unaffected by the presence of boundaries and $Ri < 0.25$.

Figure 12 shows a comparison of the various mixing models discussed above with our DNS data for Case 3 measured at a height of $z = 0.6$ over the duration of the transient simulation. Panel (*a*) compares k_h/ν as a function of Re_b calculated using the direct model with the Osborn and Osborn–Cox models. For $Re_b < 100$ all three models give approximately the same value of k_h/ν. This is consistent with the results of Shih *et al.* (2005) who found that, for homogeneous sheared stratified turbulence, the Osborn model holds well only in their intermediate regime $7 < Re_b < 100$. The direct and Osborn–Cox models remain in good agreement up to $Re_b \approx 1500$ after which they start to diverge. Panel (*b*) shows that this corresponds to the point in the simulation when the assumption of $P_\phi/\chi \approx 1$ implicit in the Osborn–Cox model begins to break down. Panel (*c*) shows R_f as a function of D compared with the model of Ivey *et al.* (2018). There is good agreement between the DNS data and the model up to $D \approx 20$. As can be seen from (*d*), $D = 20$ corresponds to $Re_b \approx 1500$, and hence, again, the point where the assumptions underlying this model begin to break down.

Another model for eddy diffusivity based on the Osborn model has recently been suggested by Zhou *et al.* (2017). This model was developed in the context of stratified

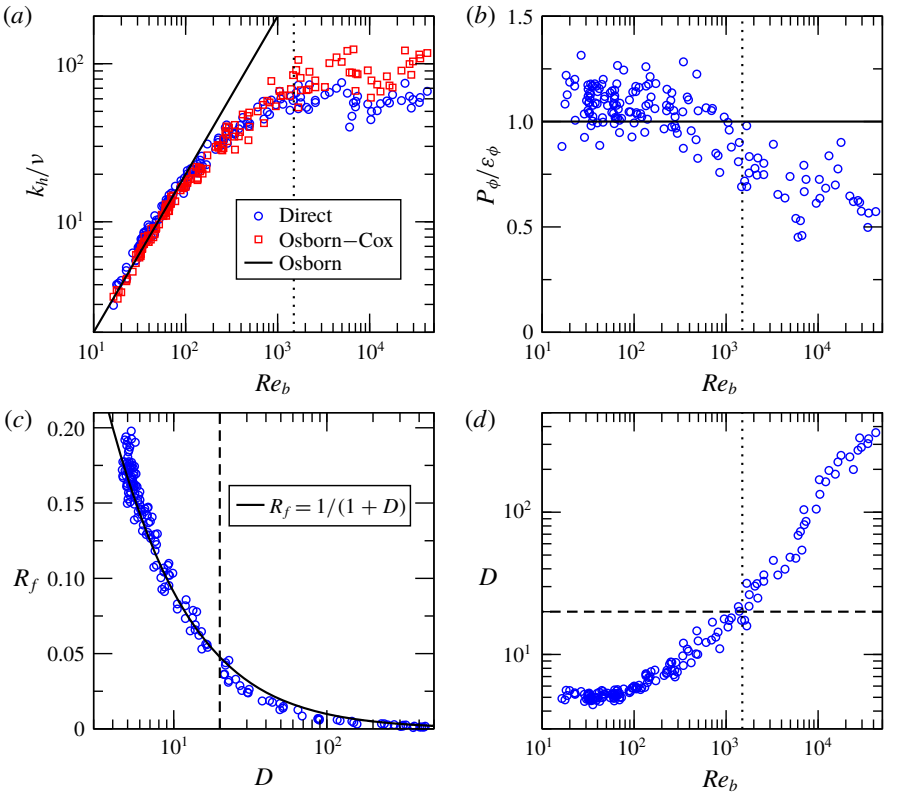

FIGURE 12. (Colour online) A comparison of various mixing models for Case 3 at $z = 0.6$. (*a*) Shows k_h/ν calculated by the direct (5.2), Osborn (7.1) and Osborn–Cox (7.2) models plotted against Re_b. (*b*) Shows P_ϕ/χ plotted against Re_b. (*c*) Shows R_f as a function of D compared with the model of Ivey *et al.* (2018) (7.3). (*d*) Shows D as a function of Re_b.

plane Couette flow, which is characterised by a central region in which turbulent fluxes are approximately constant. Noting that in this region $Ri \approx Pr_t R_f$ and $Pr_t \approx 1$, substituting $Ri \approx R_f$ into (7.1) they proposed modelling k_h/ν as

$$k_h/\nu = Re_b \frac{Ri}{1 - Ri}. \tag{7.5}$$

Figure 13(*a*) compares our measured values of k_h/ν with values calculated using (7.5) at different heights across the channel. The model gives a good prediction of k_h/ν across the central region of the channel and remains accurate down to $z = 0.1$, close to the lower solid wall. Prediction close to the upper surface at $z = 0.9$ is poor. This is expected since assumptions underpinning this model are not satisfied in this region.

The model of Zhou *et al.* (2017) diverges from the data somewhat for high $Re_b Ri/(1 - Ri)$, which may be due to the fact that it assumes $Pr_t = 1$, whereas in our flow we have shown that Pr_t decreases to $Pr_t \approx 0.8$ once stratification becomes weak. The model can be modified to include Pr_t explicitly by approximating R_f as $R_f \approx Ri/Pr_t$ in (7.1). This gives an alternative model,

$$k_h/\nu = Re_b \frac{Ri}{Pr_t - Ri}. \tag{7.6}$$

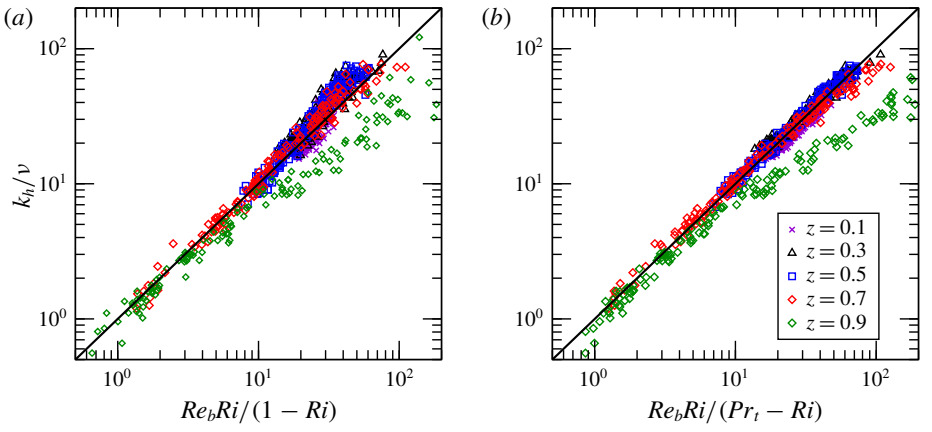

FIGURE 13. (Colour online) Comparison of data with models given in (7.5), and (7.6) at different heights across the channel for Case 3.

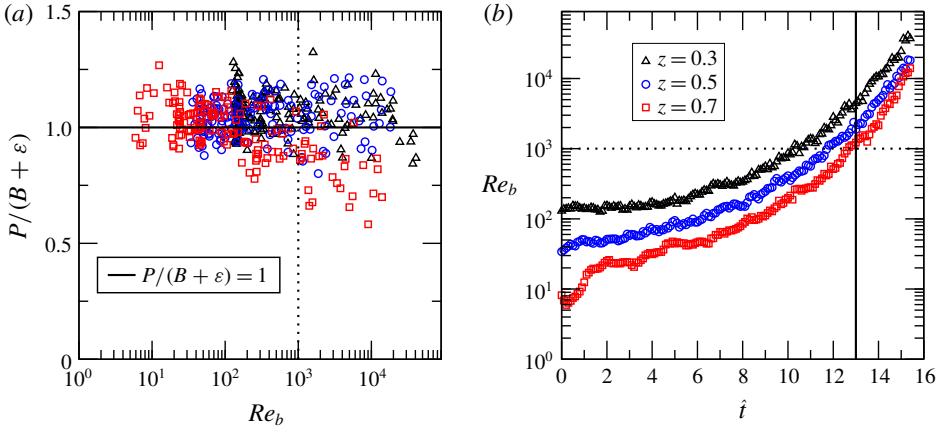

FIGURE 14. (Colour online) Relationships between $P/(B+\varepsilon)$, Re_b and $\hat{t}$ for Case 3 at $z=0.3$, 0.5 and 0.7.

Figure 13(*b*) compares our measured values of k_h/ν with values calculated using our modified model (7.6). This model offers an improvement over that of Zhou *et al.* (2017), particularly in the weakly stratified regime. This improvement comes at the expense of having to measure or estimate Pr_t.

In § 5 we defined the central region of the channel as comprising $z=0.3$–0.7 on the basis that, in this region, the balance $P\approx(B+\varepsilon)$ holds until late in the destratification process. Figure 14 shows relationships between $P/(B+\varepsilon)$, Re_b and time $\hat{t}$ for Case 3 measured over the duration of the transient simulation at heights $z=0.3$, 0.5 and 0.7. Panel (*a*) shows that, at $z=0.3$ and $z=0.5$, $P/(B+\varepsilon)\approx 1$ for the entire simulation, while at $z=0.7$, $P/(B+\varepsilon)$ starts to drop below 1 for $Re_b \gtrapprox 1000$. In (*b*) it can be seen that at $z=0.7$ the flow passes $Re_b=1000$ at $\hat{t}=13$. Thus the region $z=0.3$–0.7 remains in energetic equilibrium until the very late stages of the flow evolution.

Figure 15 shows relationships between k_h/ν, Re_b, Ri and R_f for Case 3 at heights $z=0.3$, 0.5 and 0.7. The parameter relationships at different heights overlap, indicating

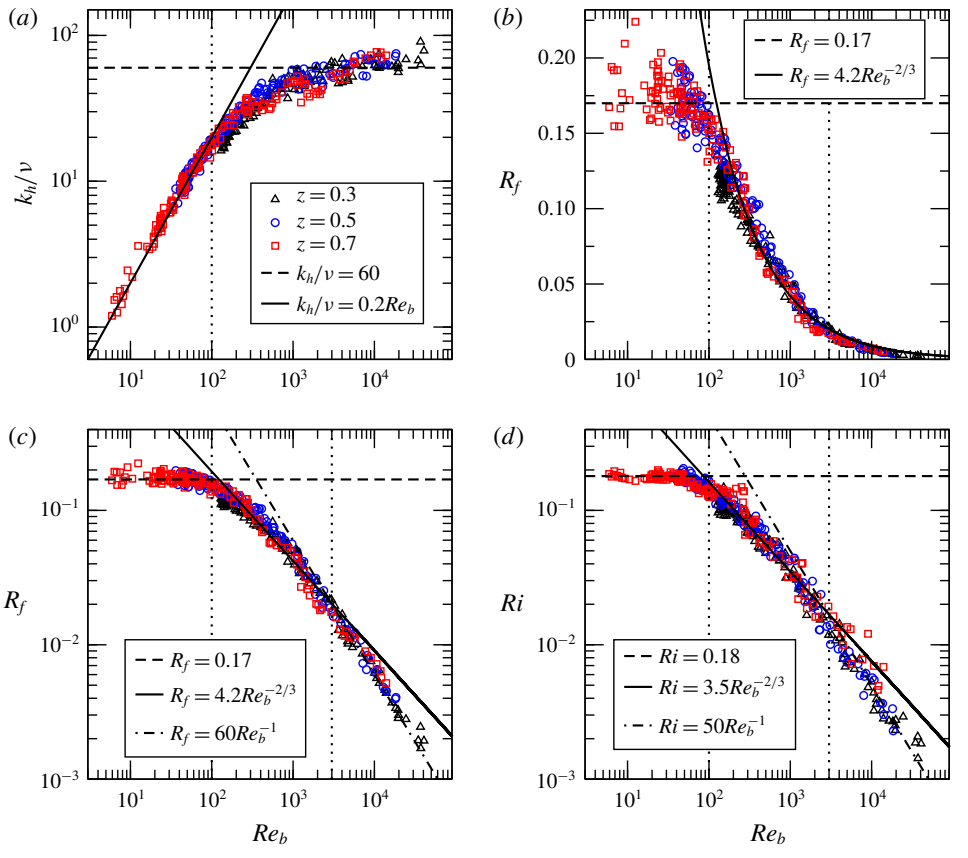

FIGURE 15. (Colour online) Relationships between k_h/ν, Re_b, R_f and Ri for Case 3 at $z = 0.3,\ 0.5$ and 0.7.

the dynamic balances within the flow are similar across the central region of the channel. Most of the deviations seen are for data from the early stages of the flow evolution when the flow is relaxing as described above.

The plot of k_h/ν against Re_b in (*a*) shows that our data adhere closely to the Osborn (1980) relationship $k_h/\nu = \Gamma Re_b$ with $\Gamma = 0.2$ for $Re_b < 100$ (the intermediate and diffusive regimes of Shih *et al.* (2005)) at all heights. For $Re_b > 100$ (the energetic regime of Shih *et al.* (2005)) k_h/ν approaches an asymptotic value of $k_h/\nu \approx 60$. Again, this asymptotic value is independent of z.

Panels (*b*,*c*) show R_f plotted against Re_b on log-linear and log-log scales, with the former emphasising trends in the data for low to intermediate Re_b, while the latter allowing easier interpretation of data at high Re_b. For $Re_b < 100$, R_f remains constant at $R_{f,c} \approx 0.17$, while for $Re_b > 100$, R_f decreases with increasing Re_b. Thus the transition from constant to Re_b-dependent R_f corresponds to the transition from the intermediate to the energetic regime.

The relationship between R_f and Re_b has received considerable attention in the literature (see Walter *et al.* 2014; Mater & Venayagamoorthy 2014*a*,*b*, for example) due to its importance in geophysical measurements and modelling. Scotti & White (2016) discuss the relationship between Re_b and $Ri_f (\approx R_f)$ and note that the two parameters approach a power law relationship of the form $Ri_f = CRe_b^n$ at high Re_b for

a data from a wide range of geophysical and small scale flows. They argue that, while n has generally been found to lie in the range $-1/2$ to $-2/3$ (see Bluteau, Jones & Ivey 2013; Walter *et al.* 2014, for example), there is no justification for a universal exponent. The existence of a universal exponent implies that Ri_f depends on a single non-dimensional parameter, whereas Mater & Venayagamoorthy (2014*a*,*b*) show that Ri_f must depend on more than one parameter. Scotti & White (2016) present scaling arguments that demonstrate that Ri_f is also a function of a 'hidden' scale that depends on the nature of the flow. For Monin–Obukhov (M–O) layers in a semi-bounded flow, this scale is the ratio of the height z above the bottom solid boundary to the Obukhov length scale L (that is the M–O stability parameter $\zeta = z/L$), whereas, in bounded flows such as channel flow, the scale is an externally imposed confinement scale that is related to the domain height h. For stratified plane Couette flow they show that Ri_f is expected to approach an inverse linear relationship $Ri_f \sim Re_b^{-1}$ for large Re_b.

Our data support these arguments. For moderate Re_b in the range $200 < Re_b < 3000$, the data fit well to a $-2/3$ power law with $R_f = 4.2Re_b^{-2/3}$, while for $Re_b > 3000$ the data approach a -1 power law with $R_f = 60Re_b^{-1}$. For $Re_b < 3000$, buoyancy length scales such as the Ozmidov scale l_O are small in comparison to the confinement scale l_c associated with the channel height h, so the confinement due to the finite height of the channel has a negligible effect on the turbulence dynamics. For $Re_b > 3000$, as the buoyancy length scale becomes comparable with and then greater than l_c, the effects of confinement influence the turbulence dynamics and mixing efficiency. These effects are reflected in the scaling of R_f with Re_b. This can be seen from the profiles of l_O in figure 9. Noting from figure 14 that, for $z = 0.5$, $Re_b = 3000$ corresponds to $\hat{t} \approx 13.5$, the profile of l_O in figure 9 shows that, at this stage, $l_O = O(1)$, implying $l_O \approx l_c$. (Note that all of our length scales are non-dimensionalised by channel height.)

Panel (*d*) shows Ri plotted against Re_b. The data for Ri show very similar trends to those seen for R_f. This is expected given that, for equilibrium conditions, $Ri \approx Pr_t R_f$ and Pr_t remains relatively constant. In the strongly stratified regime for $Re_b < 100$, $Ri \approx Ri_c = 0.18$. For $200 < Re_b < 3000$, Ri scales according to $Ri = 3.5Re_b^{-2/3}$ while for large Re_b it approaches $Ri = 50Re_b^{-1}$. The ratio of the coefficients in the asymptotic relations for R_f and Ri is approximately 0.8, which is consistent with our finding above (see figure 10) that Pr_t approaches a neutral flow value of $Pr_{t,n} \approx 0.8$.

A power law relationship of the form $Ri = CRe_b^{-1}$ for large Re_b was also derived by Chung & Matheou (2012), who use scaling arguments to show that

$$Ri \sim (\kappa l_c/\eta)^{4/3} Re_b^{-1}. \tag{7.7}$$

Here κ is the von Kármán constant and l_c an externally imposed vertical confinement length scale which, similar to above, is non-dimensionalised in terms of the vertical dimension of their computational domain L_z. Using the fact that $R_f \equiv Pr_t^{-1} Ri$, they show that k_h/ν is expected to approach an asymptotic value of

$$k_h/\nu \approx (\kappa l_c/\eta)^{4/3} Pr_{t,n}^{-1}, \tag{7.8}$$

where $Pr_{t,n}$ is the turbulent Prandtl number in neutral conditions.

Within this framework, the asymptotic relation for our data, $Ri = 50Re_b^{-1}$, compared with (7.7), gives $(\kappa l_c/\eta)^{4/3} \approx 50$. For our flow case the non-dimensional Kolmogorov scale η varies; however, figure 9 shows that, within the central region of the channel, it is of order $\eta \approx 5.5 \times 10^{-3}$ as the flow approaches neutral conditions. Using a value $\kappa = 0.41$ for the von Kármán constant, this gives an estimate of the equivalent confinement

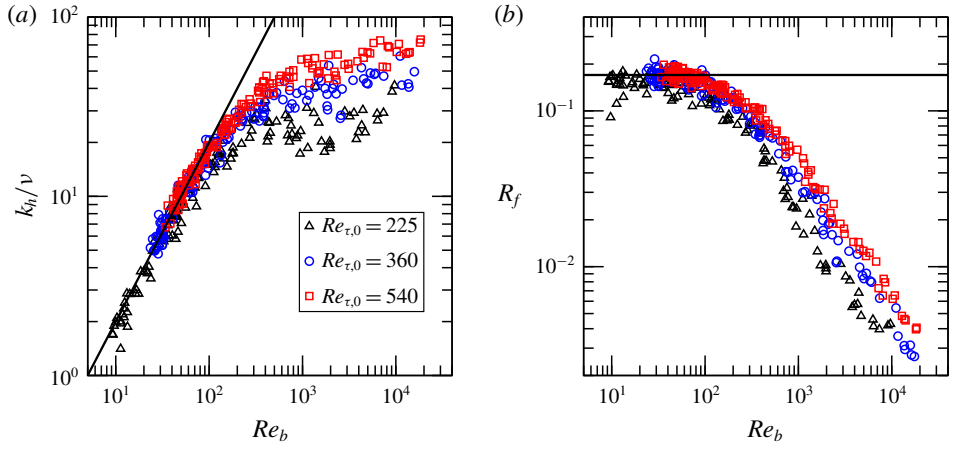

FIGURE 16. (Colour online) Eddy diffusivity normalised by viscosity k_h/ν and flux Richardson number R_f plotted against buoyancy Reynolds number Re_b at $z = 0.5$ for Cases 3, 4 and 5.

scale in our flow of $l_c \approx 0.25$, which is the same as the value Chung & Matheou (2012) found for homogeneous sheared stratified turbulence. Substituting this into (7.8) and using our value $Pr_{t,n} = 0.8$ gives $k_h/\nu \approx 60$, which is the asymptotic value seen in our data for Case 3.

In unstratified channel flow the Kolmogorov scale non-dimensionalised by channel height varies with Re_τ according to

$$\eta \sim Re_\tau^{-3/4}, \tag{7.9}$$

so we expect this dependence to be reflected in the asymptotic value of k_h/ν. This is confirmed in figure 16(*a*), which shows k_h/ν plotted against Re_b for the $Re_{\tau,0} = 225$, 360 and 540 cases at a height of $z = 0.5$. The asymptotic value of k_h/ν increases with Re_τ, consistent with a decreasing Kolmogorov scale. The value of Re_b at which the flow transitions away from the linear Osborn relationship $k_h/\nu = \Gamma Re_b$ is also not constant, but increases with increasing Re_τ. Panel (*b*) demonstrates that the relationship between R_f and Re_b is also Re_τ-dependent. Although not shown, a similar Re_τ-dependence was also observed for Ri.

Dividing (7.8) by Re_τ gives

$$\frac{(k_h/\nu)}{Re_\tau} \sim \frac{1}{Re_\tau}\left(\frac{\kappa l_c}{\eta}\right)^{4/3} Pr_{t,n}^{-1}. \tag{7.10}$$

Rearranging and noting that, in our non-dimensionalisation scheme, $(k_h/\nu)/Re_\tau \equiv \tilde{k}_h/(\tilde{u}_\tau \tilde{h}) \equiv k_h$ gives

$$k_h \sim \left(\frac{\kappa l_c}{\eta/Re_\tau^{-3/4}}\right)^{4/3} Pr_{t,n}^{-1}. \tag{7.11}$$

Equation (7.9) implies that the right-hand side of (7.11) is a constant. To determine this constant we consider the $Re_{\tau,0} = 540$ case shown in figure 15, for which the asymptotic value of k_h/ν was found to be $k_h/\nu \approx 60$. The actual Reynolds number

Case	$Re_{\tau,0}$	$Re_{\tau,max}$	λ_0	$Ri_{\tau,0}$	Pr	α_0
3	540	660	2	284	0.71	8
4	225	285	2	175	0.71	8
7	360	410	1	64	0.5	8
9	360	410	1	74	0.71	4

TABLE 3. Simulation parameters for the reduced case set.

during the later stages of the simulation is $Re_\tau \approx 660$, which implies an asymptotic value for the non-dimensional eddy diffusivity $k_{h,c} \approx 0.1$. From the analysis above this value should be independent of Re_τ. The value of $k_{h,c}$ deduced from our results is very similar to the values of approximately 0.09–0.1 given by Kim & Moin (1989) for the outer layer of turbulent channel flow at $Re_\tau \approx 180$ with a passive scalar at Pr between 0.71 and 2.

The analysis above suggests a relationship between k_h, Re_b and Re_τ of the form $k_h = f(Re_b/Re_\tau)$. Hence, we define a parameter

$$\mathcal{Q} = \frac{Re_b}{Re_\tau}. \tag{7.12}$$

In the weakly stratified regime, where $\tilde{k}_h/\tilde{\nu}$ becomes independent of Re_b but scales as $\tilde{k}_h/\tilde{\nu} \sim Re_\tau$, using $k_h \equiv \tilde{k}_h/(\tilde{\nu}Re_\tau)$ removes this Re_τ-dependence. (For clarity, we have written $\tilde{k}_h/\tilde{\nu}$ in terms of dimensional variables here. Please note that, within our non-dimensionalisation scheme, $k_h/\nu \equiv \tilde{k}_h/\tilde{\nu}$.) In the strongly stratified regime where $\tilde{k}_h/\tilde{\nu}$ scales linearly with Re_b and is independent of Re_τ, the effect of Re_τ within the parameter $\mathcal{Q}$ is removed via cancellation, and the relation is equivalent to the linear Osborn model,

$$k_h \equiv \frac{\tilde{k}_h}{\tilde{\nu}}\frac{1}{Re_\tau} = \Gamma\frac{Re_b}{Re_\tau} \rightarrow \frac{\tilde{k}_h}{\tilde{\nu}} = \Gamma Re_b. \tag{7.13}$$

Thus, this parameter combines the effect of an externally imposed vertical confinement scale h, which constrains turbulent motions in the weakly stratified regime – the 'hidden scale' for bounded flows of Scotti & White (2016) – with the local turbulence parameterisation provided by Re_b in the strongly stratified regime where the buoyancy scale l_O provides the dominant constraint.

Figure 17 shows relationships between k_h, $\mathcal{Q}$, R_f and $P/(B+\varepsilon)$ at $z = 0.5$. Data are plotted for Cases 3, 4, 7 and 9. As shown in table 3, these cases give a range of each parameter ($Re_{\tau,0}$ ranging from 225 to 540, λ_0 from 1 to 2, Pr from 0.5 to 0.71, α_0 from 4 to 8). This reduced set of cases will be used in many of the following figures because it can be shown more compactly than the full data set while still highlighting any parameter dependencies. Figure 17 is similar to figures 14 and 15; however, here we have plotted flow parameters against $\mathcal{Q}$ rather than Re_b and compare results across all parameters.

The data for k_h as a function of $\mathcal{Q}$ shown in (*a*) collapse convincingly for the high and low Reynolds number cases (Cases 3 and 4) with this scaling. Given that $k_h \equiv (k_h/\nu)/Re_\tau$ and the Osborn relationship (7.1) is linear, this relationship is maintained for low $\mathcal{Q}$, that is,

$$k_h = \Gamma\mathcal{Q}, \tag{7.14}$$

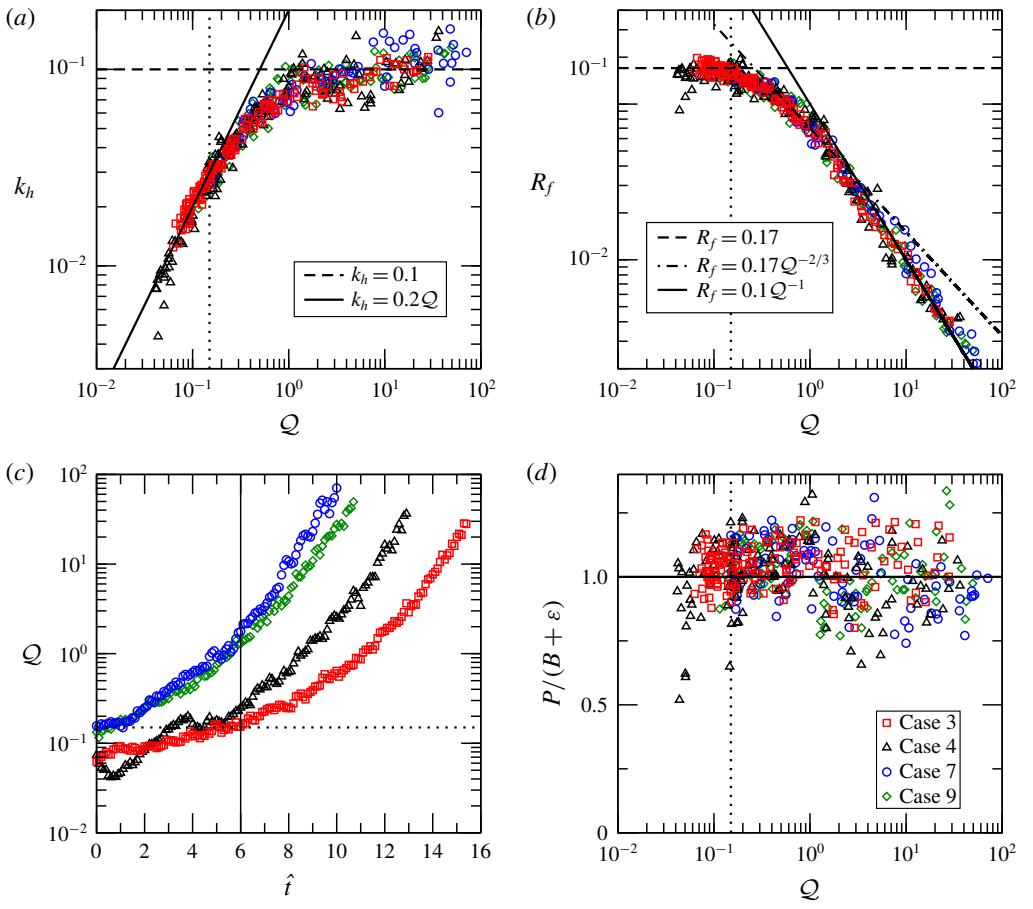

FIGURE 17. (Colour online) Relationships between k_h, $\mathcal{Q}$, R_f and $P/(B+\varepsilon)$ at $z = 0.5$ for Cases 3, 4, 7 and 9. The dotted line is $\mathcal{Q} = \mathcal{Q}_{tr} = 0.15$.

with $\Gamma = 0.2$. The point at which the flow transitions away from the linear regime is independent of Re_τ, with a value of $\mathcal{Q}_{tr} \approx 0.15$. For $\mathcal{Q} \gtrapprox \mathcal{Q}_{tr}$, k_h approaches a single asymptotic value of $k_{h,c} \approx 0.1$, as suggested by the analysis above. This is in contrast to the scaling of k_h/ν with Re_b (figure 16) for which the asymptotic value has a strong dependence on Re_τ.

The data for Case 9, in which $\lambda_0 = 1$ and $\alpha_0 = 4$, compared with $\lambda_0 = 2$ and $\alpha_0 = 8$ for Cases 3 and 4, also collapse; λ_0 and α_0 affect the flow only through their influence on initial conditions such as vertical gradients of mean velocity and temperature. We expect this to be accounted for by a local turbulence parameter such as Re_b.

While there is quite a lot of scatter in the data, it appears that, for the low Prandtl number case (Case 7), k_h is somewhat higher than the other cases in the very weakly stratified regime $\mathcal{Q} \gtrapprox 5$. There also appears to be a Pr-dependence in the relationship between R_f and $\mathcal{Q}$ shown in (*b*) for $\mathcal{Q} \gtrapprox 5$. Due to its effect on molecular diffusivity, Pr affects the balance between turbulent and molecular heat fluxes in the flow, which in turn affects the mean temperature gradient. As a result it is expected to have an influence on flux and gradient-based parameters.

The dotted lines in each panel show the value $\mathcal{Q}_{tr} = 0.15$ at which k_h transitions from the linear regime governed by the Osborn relation to the nonlinear energetic regime. As with the Re_b scaling, $\mathcal{Q}_{tr}$ also corresponds to the point at which R_f transitions away from its critical value of 0.17. At moderate $\mathcal{Q}$ in the range $0.2 < \mathcal{Q} < 3.5$, R_f follows a $-2/3$ power law with $R_f = 0.07\mathcal{Q}^{-2/3}$. For $\mathcal{Q} > 3.5$, R_f approaches an inverse linear relationship of the form $R_f = 0.1\mathcal{Q}^{-1}$. These are analogous to the relationships between Re_b, and R_f discussed above.

Although not shown, similar trends and collapse of the data were observed when Ri is plotted as a function of $\mathcal{Q}$, with $Ri = Ri_c = 0.18$ for $\mathcal{Q}_{tr} \lessapprox 0.15$, and approaching an inverse linear relationship of the form $Ri = 0.08\mathcal{Q}^{-1}$ for high $\mathcal{Q}$, as expected based on $Ri \approx Pr_t R_f$.

In (*c*) it can be seen that, for Case 3 at the mid-channel height, the flow passes the transitional value $\mathcal{Q}_{tr} = 0.15$ at time $\hat{t} = 6$ which is relatively early in the flow evolution. Panel (*d*) shows that local energetic equilibrium is maintained for the entire destratification process at this height for all cases. These two panels are included primarily for the purpose of comparison with the near-surface region that will be discussed in § 8.

While k_h is important in the context of turbulence modelling, a more relevant parameter in our case is the total vertical heat flux, since this flux ultimately determines the rate at which the channel destratifies. This was demonstrated in § 6 where it was shown that the rate of change of domain-averaged potential energy E_p is equal to the sum of the domain-averaged turbulent and molecular buoyancy fluxes, $\mathcal{B}$ and $\mathcal{M}$. At a local level, the heat flux also determines local time evolution of the flow. The total heat flux through a horizontal layer at height z and time $\hat{t}$ is given by

$$F = -\sigma \frac{\partial \overline{\phi}}{\partial z} + \overline{\phi' w'} \equiv -(\sigma + k_h) \frac{\partial \overline{\phi}}{\partial z}. \tag{7.15}$$

As will be discussed in § 11, it is useful to normalise this flux by the temperature difference across the channel, $\Delta\phi$, to give a normalised total heat flux,

$$\mathcal{F} = \frac{1}{\Delta\phi} \left(-\sigma \frac{\partial \overline{\phi}}{\partial z} + \overline{\phi' w'} \right), \tag{7.16}$$

where $\Delta\phi$ is defined as $\Delta\phi = \overline{\phi}(h) - \overline{\phi}(0)$.

Figure 18 shows the normalised total flux $\mathcal{F}$ plotted against $\mathcal{Q}$ for Cases 1–10. Changing the stability parameter of the initial state λ_0 results in different initial points in ($\mathcal{Q}$, $\mathcal{F}$) space for the initial flow conditions. This indicates that, in the initial equilibrium flow, $\mathcal{F}$ depends on both $\mathcal{Q}$ and λ_0. After an initial relaxation period, however, the trajectories converge, so that, in the subsequent stages of the destratifying flow, $\mathcal{F}$ depends only on $\mathcal{Q}$. This is consistent with our argument that λ_0 is not a governing parameter for the destratifying flow. Its effect is confined to the initial conditions and the relaxation period at the start of the flow evolution (see § 5).

The data in (*b*,*d*) show that $\mathcal{F}$ scales with $\mathcal{Q}$, independent of Re_τ and α_0. There is, however, a clear dependence on Pr seen in (*c*). This is consistent with the Pr-dependence seen in k_h and R_f.

Thus it appears that local turbulent mixing in the central region of the channel is a function of $\mathcal{Q}$ and Pr. The fact that the flux parameters $\mathcal{F}$ and R_f depend on both $\mathcal{Q}$ and Pr makes intuitive sense, since $\mathcal{Q}$ incorporates the effects of turbulent fluctuations, buoyancy and the large scale mean shear in the channel, while Pr represents the effects molecular viscosity and thermal diffusivity.

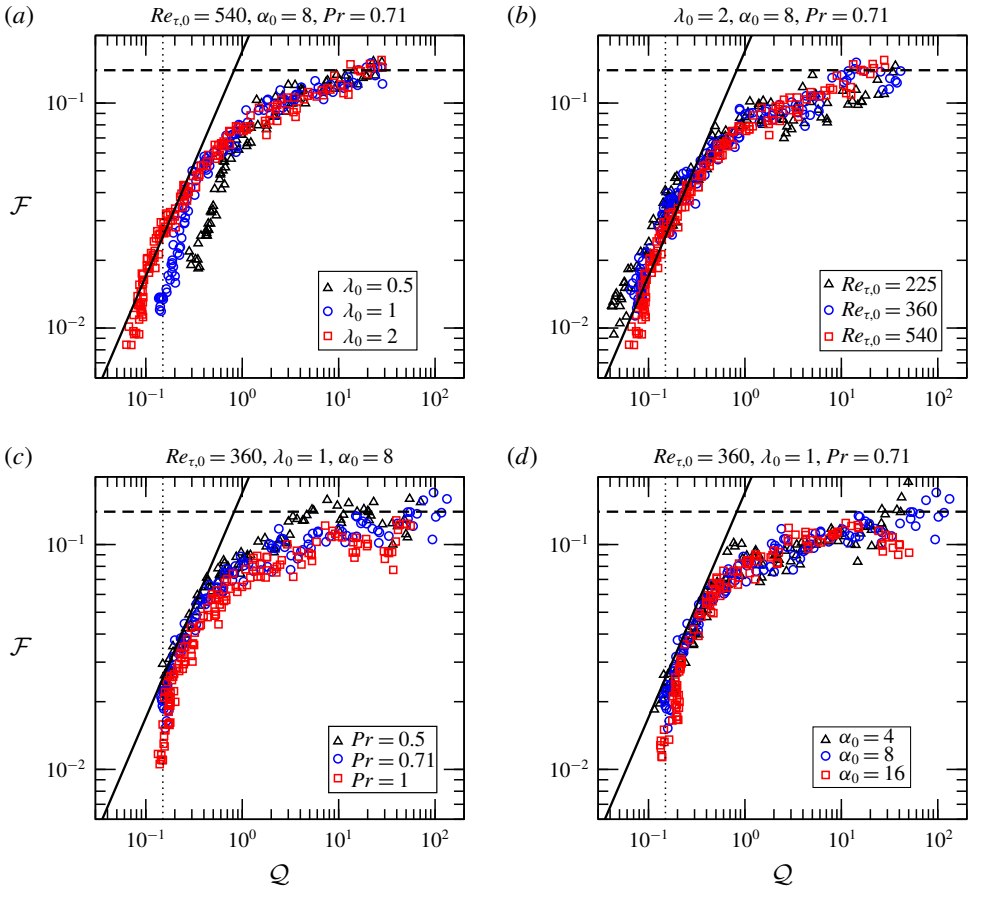

FIGURE 18. (Colour online) Normalised total flux $\mathcal{F}$ plotted against $\mathcal{Q}$ at $z = 0.5$ for Cases 1–10. The solid line is $\mathcal{F} = 0.17\mathcal{Q}$. The dashed line represents the asymptotic value $\mathcal{F} = 0.14$. The dotted line is $\mathcal{Q} = \mathcal{Q}_{tr} = 0.15$.

The effect of vertical location within the channel is shown in figure 19, which shows k_h and R_f as functions of $\mathcal{Q}$ at various heights across the channel for Case 3. Both k_h and R_f are independent of height in the central region but attenuated in the near-wall and near-surface regions, due to the constraining effects on the turbulent motions of the nearby boundaries as discussed in § 5. This deviation does not occur for low $\mathcal{Q}$ where the buoyancy length scale is small relative to the distance from the boundary and hence acts as the dominant constraint.

8. Relationships between local flow parameters in the near-surface region

We now consider the near-surface region which, for consistency with our previous definition of the central region, we define as $z = 0.7$–1. For neutral flow, Hunt & Graham (1978) and Calmet & Magnaudet (2003) have shown that the depth of the region affected by the free surface is related to the integral length scale l_∞, which they found to be approximately $l_\infty \approx 0.2h$. Hunt & Graham (1978) suggest that turbulence in this region is dissipated by a viscous sublayer at the surface characterised by a length scale l_ν that scales according to $l_\nu/l_\infty \sim Re_\infty^{-1/2}$, where $Re_\infty = U_b l_\nu/\nu$. This

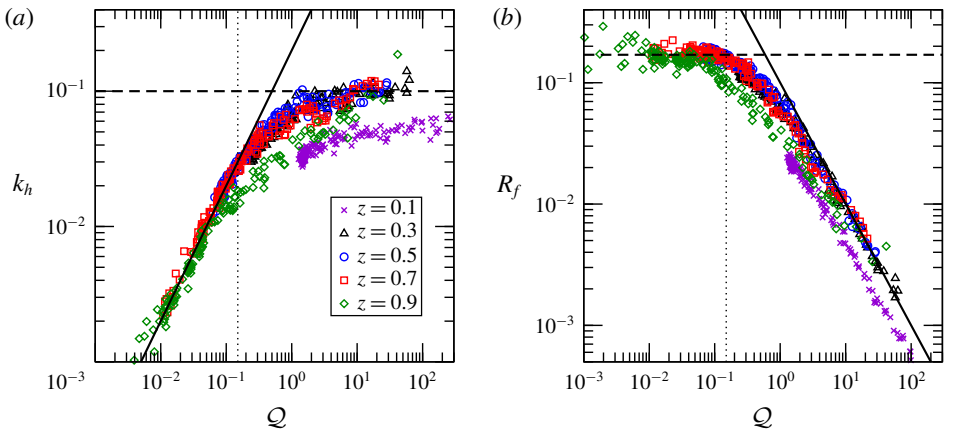

FIGURE 19. (Colour online) Values of k_h and R_f plotted against $\mathcal{Q}$ at various heights for Case 3. (*a*) The dashed line is $k_h = 0.1$ and the solid line $k_h = \Gamma\mathcal{Q}$. (*b*) The dashed line is $R_f = 0.17$ and the solid line $R_f = 0.1\mathcal{Q}^{-1}$.

implies a Reynolds number dependence for $z \gtrapprox 0.8$. Williamson *et al.* (2015) report a significant Reynolds number dependence in horizontal turbulence intensity components for both neutral and stratified cases. In our simulations, the radiative thermal forcing applied to the initial state flow means that the near-surface region is also the region most strongly affected by stratification, and, for $\lambda_0 \geqslant 1$, the region above $z = 0.8$ is essentially laminar in the initial state at the relatively low values of Re_τ investigated in this paper.

Figure 20 shows the same relationships for Cases 3, 4, 7 and 9 as figure 17 except, in this case, the relationships are plotted at a height of $z = 0.9$, which is well within the near-surface region, rather than at $z = 0.5$.

The relationship between k_h and $\mathcal{Q}$ in (*a*) shows similar trends to that seen at $z = 0.5$, with the Osborn relationship $k_h = \Gamma\mathcal{Q}$ maintained for low $\mathcal{Q}$, and k_h approaching $k_{h,c} = 0.1$ at high $\mathcal{Q}$. The transition value, $\mathcal{Q}_{tr,s}$, is, however, significantly lower, with a value of $\mathcal{Q}_{tr,s} = 0.05$ compared to the value, $\mathcal{Q}_{tr,c} = 0.15$, observed across the central region. (Here we use subscripts '*s*' and '*c*' to distinguish between the near-surface and central regions.) To aid interpretation, these two points are represented on the graphs as dotted lines. Consistent with the discussion above, there is also a Reynolds number dependence, with k_h for the $Re_{\tau,0} = 225$ case (Case 4) significantly lower than for the $Re_{\tau,0} = 540$ case (Case 3).

The molecular diffusivity σ for the three Reynolds numbers is shown as dot-dashed lines with the same colour coding as the data points. In all cases the initial state of the flow has $k_h \ll \sigma$ at this height, indicating that initially the flow is laminar at this height according to our definition of laminar in § 5. This is consistent with the discussion above, and with the flow field visualisations shown in (*a*) of figures 2 and 3. We will refer to this as the laminar–turbulent transition point, $\mathcal{Q}_{lt}$. The $Re_{\tau,0} = 540$ case crosses this laminar–turbulent transition point at $\mathcal{Q}_{lt} = 0.012$, which is also shown on all plots as a dotted line.

As can be seen in (*d*), the laminar–turbulent transition corresponds to the flow reaching a state of local energetic equilibrium, which is maintained until $\mathcal{Q} = \mathcal{Q}_{tr,s} = 0.05$ after which $P/(B + \varepsilon)$ decays. Thus it appears that, in contrast to the situation in the central region, the transition away from the Osborn linear

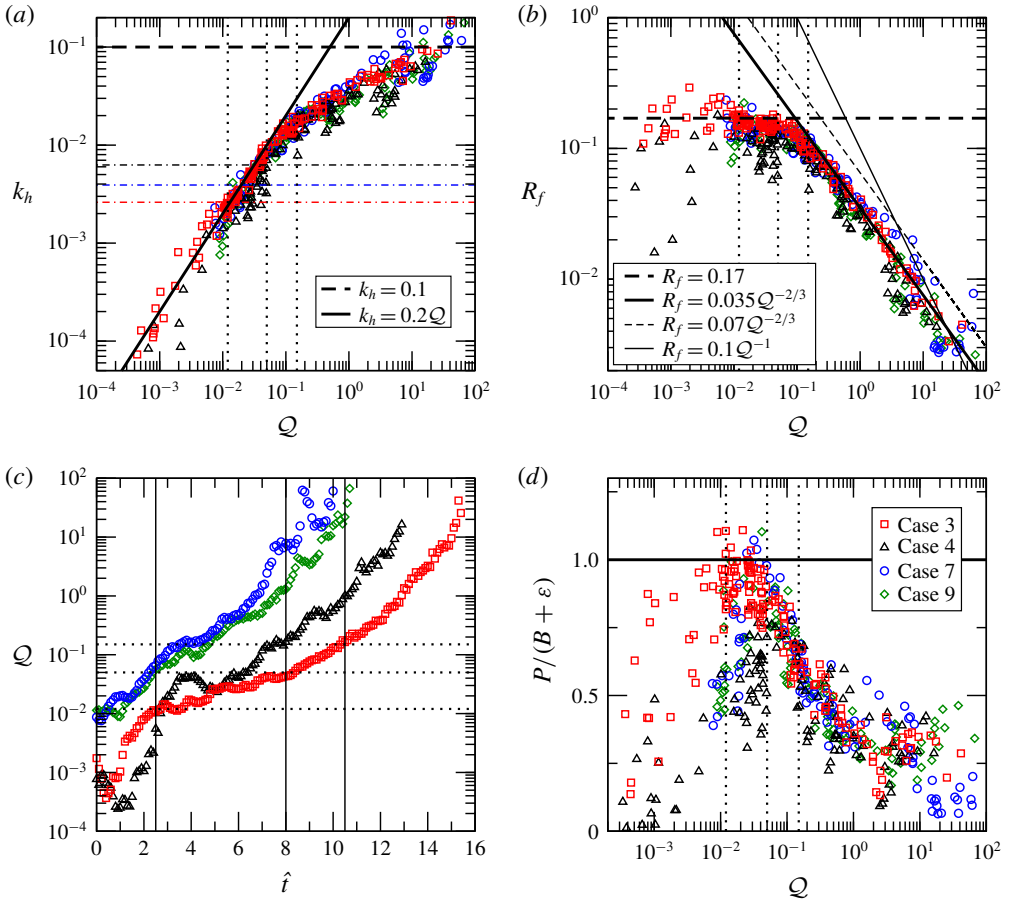

FIGURE 20. (Colour online) Relationships between k_h, $\mathcal{Q}$, R_f and $P/(B+\varepsilon)$ at $z=0.9$ for Cases 3, 4, 7 and 9. The dotted lines are $\mathcal{Q}_{lt}=0.012$ (the laminar–turbulent transition point for Case 3), $\mathcal{Q}_{tr,s}=0.05$ for $z=0.9$ and $\mathcal{Q}_{tr,c}=0.15$ for $z=0.5$. The dot-dashed lines in (*a*) show $k_h=\sigma$. The thin lines in (*b*) show the lines of best fit for the data at $z=0.5$.

relation, $k_h=\Gamma\mathcal{Q}$, in the near-surface region is associated with a transition away from local equilibrium, rather than a transition to the energetic turbulence regime.

The relationship between R_f and $\mathcal{Q}$ shown in (*b*) shows similar trends to that seen at $z=0.5$. The lines of best fit for the data at $z=0.5$ are shown as thin lines on the figure. For low $\mathcal{Q}$, R_f is maintained at the same critical value of $R_{f,c}=0.17$ seen at $z=0.5$, before transitioning at $\mathcal{Q}=\mathcal{Q}_{tr,s}$ to a power law relationship, $R_f=0.035\mathcal{Q}^{-2/3}$. The coefficient $C=0.035$ here is half the coefficient $C=0.07$ seen at $z=0.5$, indicating a significant reduction in mixing efficiency. Interestingly, there is no indication of a transition from the $-2/3$ power law to a -1 power law as seen in the central region. Instead the data follow $R_f=0.035\mathcal{Q}^{-2/3}$ for their entire range. It may be that our simulations do not reach high enough $\mathcal{Q}$ for this transition to occur. Also in contrast to the data at $z=0.5$, at $z=0.9$ a Reynolds number dependence is apparent, with R_f lower for the $Re_{\tau,0}=225$ case (Case 4).

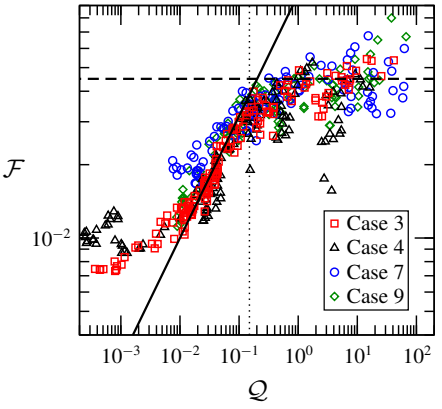

FIGURE 21. (Colour online) Normalised total flux $\mathcal{F}$ plotted against $\mathcal{Q}$ at $z = 0.9$ for Cases 3, 4, 7 and 9. The solid line is $\mathcal{F} = 0.1\mathcal{Q}^{1/2}$. The dashed line represents the asymptotic value $\mathcal{F} = 0.05$. The dotted line is $\mathcal{Q} = \mathcal{Q}_{tr} = 0.15$.

As can be seen from (*c*), for Case 3 the turbulent transition point, $\mathcal{Q}_{lt} = 0.012$, corresponds to a time $\hat{t} \approx 2.5$, while $\mathcal{Q}_{tr,s}$ and $\mathcal{Q}_{t,c}$ correspond to $\hat{t} = 8$ and $\hat{t} = 10.5$ respectively. Referring to the flow field visualisations in figures 2 and 3, at $\hat{t} = 1.5$ the region of intense shear production associated with the initial flow relaxation is approaching $z = 0.9$. By $\hat{t} = 3$ the flow in the region surrounding $z = 0.9$ contains the distinctive Kelvin–Helmholtz-like shear instabilities that persist through to the images at $\hat{t} = 7$. From (*d*) it is seen that the period $\hat{t} = 2.5$–8 is the period in which the flow at $z = 0.9$ is in local equilibrium. After $\hat{t} = 8$ local equilibrium conditions break down in the near-surface region. The visualisations at $\hat{t} = 9$ show that the K–H-like instabilities have almost disappeared by this time.

As with the central region, a Prandtl number dependence is seen in the weakly stratified regime for both k_h and R_f at this height.

Figure 21 shows the normalised total flux $\mathcal{F}$ as a function of $\mathcal{Q}$ for Cases 3, 4, 7 and 9 at a height of $z = 0.9$. With regard to parameter dependence, the dependence on Pr seen at $z = 0.5$ is not apparent at $z = 0.9$. Similarly the dependence on λ_0 in the initial state and early relaxation period is less distinct. There may be a dependence on Re_τ in the late stages of the flow evolution with a slight reduction in $\mathcal{F}$ with Re_τ apparent, although the large scatter in the $Re_{\tau,0} = 225$ data makes this impossible to state with certainty. This would be consistent with the trends seen in k_h in figure 20, although varying Re_τ could also result in a change in the mean temperature gradient $\partial\overline{\phi}/\partial z$ that could offset a variation in k_h.

We conclude that at $z = 0.9$ the heat flux is primarily dependent on $\mathcal{Q}$ with a possible dependence on Re_τ due to a reduction in k_h due to the effect of proximity to the surface. At higher Reynolds numbers this effect would diminish as the viscous length scale l_ν in the near-surface region decreases.

9. Monin–Obukhov similarity scaling

Given that we have shown that the turbulence dynamics in our flow can be described in terms of $\mathcal{Q}$, and that this parameter is functionally similar to the inverse of an Obuhkov stability parameter, it is interesting to compare our results with classical Monin–Obukhov theory. Monin–Obukhov similarity scaling (Monin 1970)

was originally developed to describe exchange processes in the surface layer of the atmospheric boundary layer and has been widely used to describe both stable and unstable atmospheric boundary layers Foken (2006). The theory proposes a universal length scale,

$$L = \frac{u_\tau^3}{\kappa b_s}, \tag{9.1}$$

where b_s is the surface buoyancy flux. The Monin–Obukhov length scale, L, is the scale above which buoyancy is strongly felt, and is hence related to the Ozmidov scale. Velocity and temperature profiles within the surface layer are then written as universal functions of a stability parameter $\zeta = z/L$ where z is the height above the bottom solid surface. Here z acts as a confinement scale that places a limit on the maximum size of turbulent eddies. Turbulence is significantly affected by buoyancy effects for $\zeta > 1$.

Recently, Monin–Obukhov theory has also been extended to characterise turbulence in homogeneous stratified shear flows (Chung & Matheou 2012) and stratified plane Couette flows (Deusebio, Caulfield & Taylor 2015; Zhou *et al.* 2017). As described in § 2, a modified Obukhov length scale $\mathcal{L}$ forms the basis of the parameter $\lambda = h/\mathcal{L}$ used in Williamson *et al.* (2015) and the current work to characterise buoyancy effects in the equilibrium state of stably stratified channel flow with an internal heat source.

The original Monin–Obukhov theory was developed for the situation in which turbulent fluxes of momentum and heat are constant, as occurs in the atmospheric surface layer. As described by Zhou *et al.* (2017), these fluxes are also approximately constant in the central region of stratified plane Couette flow. Based on this, they developed a number of scalings for turbulence parameters as functions of L. As seen from the vertical profiles of turbulent fluxes shown in figure 6(*d*,*e*), our flow does not have a constant flux region, however, in the region $z = 0.5$–0.7 the vertical gradient of $\langle \phi' w' \rangle$ is small due to the turning point in this profile, while the vertical gradient of $\langle u' w' \rangle$ is modest.

Flores & Riley (2011) showed that the Obukhov length scale normalised by the viscous length scale,

$$L^+ = \frac{L}{\delta_\nu}, \tag{9.2}$$

defines the intermittency boundary for stably stratified boundary layers. Here $\delta_\nu = \nu/u_\tau$. For $L^+ \lessapprox 100$, turbulence becomes laminar with turbulent patches. Deusebio *et al.* (2015) found the intermittency boundary to be $L^+ \approx 200$ for stratified plane Couette flow.

Using scaling analysis, Zhou *et al.* (2017) show that

$$Re_b \sim \kappa \frac{l_h}{l_m} \frac{u_\tau L}{\nu} = \kappa \frac{l_h}{l_m} L^+. \tag{9.3}$$

Here l_m and l_h are mixing lengths for momentum and temperature respectively and their ratio is equal to the turbulent Prandtl number, $l_m/l_h = Pr_t$, giving

$$Re_b \sim \kappa Pr_t^{-1} L^+. \tag{9.4}$$

Scotti & White (2016) use similar arguments to derive

$$Re_b \sim \kappa (1 - Ri_f) L^+. \tag{9.5}$$

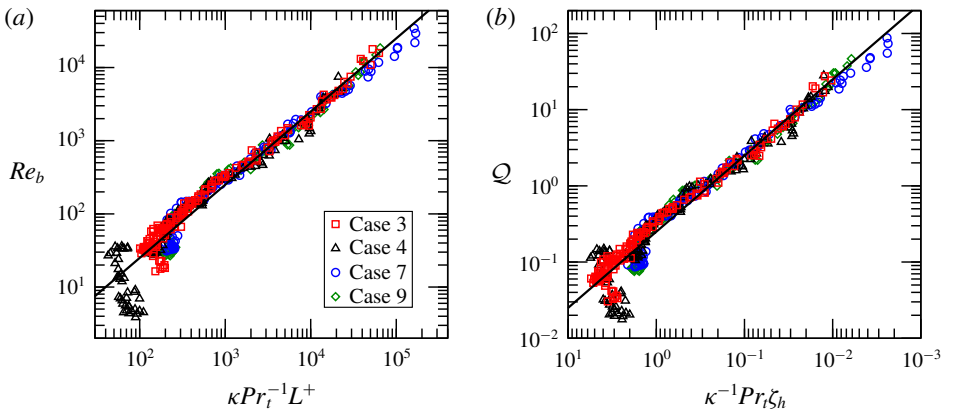

FIGURE 22. (Colour online) Monin–Obukhov scalings for Re_b and $\mathcal{Q}$ for Cases 3, 4, 7 and 9 at a height of $z = 0.6$. The solid line in (*a*) is $Re_b = 0.25\kappa Pr_t^{-1} L^+$. The solid line in (*b*) is $\mathcal{Q} = 0.25\kappa Pr_t^{-1} \zeta_h^{-1}$.

Given κ, Pr_t and $1 - Ri_f$ are close to unity, these scalings imply

$$\frac{Re_b}{L^+} \approx O(1). \tag{9.6}$$

Arguing that $Pr_t \approx 1$, Zhou *et al.* (2017) compare Re_b with L^+ for their DNS data and demonstrate that the data collapse reasonably well to the linear relationship $Re_b = \kappa L^+$ over a wide range for Reynolds, Richardson and Prandtl numbers.

In our flow both boundaries are adiabatic and there is no internal heat source. In order to define an Obukhov length scale we use the maximum of the layer-averaged total downwards buoyancy flux at a given time, that is,

$$b_{max}(\hat{t}) = \mathrm{Max}\left(\gamma\left[\sigma\frac{\partial\langle\phi\rangle}{\partial z} - \langle\phi' w'\rangle\right]\right), \tag{9.7}$$

so that

$$L = \frac{u_\tau^3}{\kappa b_{max}}, \tag{9.8}$$

and

$$L^+ = \frac{L u_\tau}{\nu} = \frac{L}{h} Re_\tau. \tag{9.9}$$

Figure 22(*a*) shows Re_b plotted against $\kappa Pr_t^{-1} L^+$ at a height of $z = 0.6$, comparing our DNS results with the scaling (9.4) of Zhou *et al.* (2017). (The scaling of Scotti & White (2016) in (9.5) gives similar trends.) Data are plotted for our reduced parameter set: Cases 3, 4, 7 and 9.

The height $z = 0.6$ was chosen because it is in the middle of the region $z = 0.5$–0.7 in which our flow approximates a constant flux layer. In contrast to Zhou *et al.* (2017), we have included the factor Pr_t^{-1} because, in our flow, Pr_t changes over time. After the initial relaxation period the data collapse to a linear relationship of the form $Re_b = 0.25\kappa Pr_t^{-1} L^+$.

An equivalent scaling for $\mathcal{Q}$ is derived by dividing (9.4) by Re_τ and combining with (9.9) to give

$$\mathcal{Q} = \frac{Re_b}{Re_\tau} \sim \kappa Pr_t^{-1} \frac{L}{h}. \tag{9.10}$$

The ratio of the channel height to the Obukhov length h/L is equivalent to the Obukhov stability parameter calculated with respect to the height of the channel, so we will refer to it as $\zeta_h = h/L$, giving

$$\mathcal{Q} = \kappa Pr_t^{-1} \zeta_h^{-1}. \tag{9.11}$$

The stability parameter ζ_h represents the ratio of the large scale motions in the channel relative to the Obukhov length scale and hence characterises the stability of the channel as a whole. It is analogous to λ for the heated equilibrium flow. The relation in (9.11) highlights the nature of $\mathcal{Q}$, as representing a ratio of buoyancy and inertial length scales.

Figure 22(*b*) shows our DNS data for $\mathcal{Q}$ plotted against $\kappa Pr_t^{-1}\zeta_h^{-1}$ at a height of $z = 0.6$. The solid line is $\mathcal{Q} = 0.25\kappa Pr_t^{-1}\zeta_h^{-1}$ which represents the scaling (9.11). Again, the data collapse well to this scaling.

Monin–Obukhov theory gives a functional form for Ri in terms of ζ as

$$Ri = \zeta \Phi_h / \Phi_m^2, \tag{9.12}$$

where $\Phi_h(\zeta)$ and $\Phi_m(\zeta)$ are the M-O stability functions, which must be determined empirically. A number of different fits to atmospheric field data have been proposed. We adopt the commonly used relations of Dyer (1974), which, for stable stratification are

$$\Phi_m = \Phi_h = 1 + 5\zeta. \tag{9.13}$$

Figure 23(*a*) shows Ri plotted against ζ for Cases 3, 4, 7 and 9 at a height of $z = 0.6$. The solid line is (9.12) with stability functions given in (9.13). Our data fit the Monin–Obukhov scaling remarkably well, especially for the high Reynolds number case (Case 3).

Another parameter commonly used to describe stably stratified turbulence is the horizontal turbulent Froude number, $Fr_h = \varepsilon/(Nu_h^2)$ where u_h is a turbulent horizontal velocity scale (see Brethouwer *et al.* 2007, for example). Zhou *et al.* (2017) show that for stratified plane Couette flow,

$$Fr_h \sim \frac{\varepsilon}{Nu_\tau^2}, \tag{9.14}$$

and then use Monin–Obukhov scalings to derive

$$Fr_h^2 \sim \kappa \frac{l_h}{l_m^2} L = Ri. \tag{9.15}$$

Figure 23(*b*) shows Fr_h calculated using (9.14) as a function of Ri for Cases 3, 4, 7 and 9 at a height of $z = 0.6$. The solid line is $Fr_h = 0.5Ri^{-1/2}$. Our data fit the scaling well for $Ri < Ri_c = 0.18$.

As discussed above, our channel flow does not have a constant flux layer, so relationships in terms of bulk Obukhov scales are not expected to be independent of height across a substantial portion of the channel. An alternative is to use a local

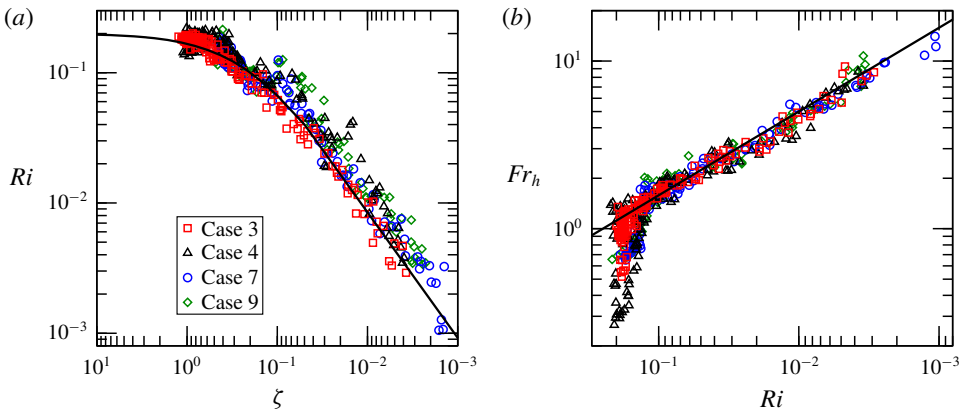

FIGURE 23. (Colour online) Monin–Obukhov scaling for Ri and Fr_h for Cases 3, 4, 7 and 9 at a height of $z = 0.6$. The solid line in (a) is (9.12) with stability functions given in (9.13). The solid line in (b) is $Fr_h = 0.5Ri^{-1/2}$.

Obukhov scaling. Based on analysis of the budgets of turbulent kinetic energy and temperature variance, Nieuwstadt (1984) derived a local Obukhov length scale,

$$\Lambda(z) = \frac{1}{\kappa}\frac{\overline{u'w'}^{3/2}}{\overline{b'w'}}, \tag{9.16}$$

where $\overline{b'w'}$ is the buoyancy flux through a horizontal layer, and showed that this length scale can be used to characterise atmospheric turbulence outside the surface layer. This length scale can be used to form a Reynolds number,

$$Re_\Lambda(z) = \Lambda\frac{\overline{u'w'}^{1/2}}{\nu}, \tag{9.17}$$

which is the local equivalent of L^+. Using an assumption of local energetic equilibrium, Williamson *et al.* (2015) show that

$$Re_b \approx \kappa Pr_t^{-1}(1 - R_f)Re_\Lambda. \tag{9.18}$$

Figure 24 shows Re_b as a function of $\kappa Pr_t^{-1}(1 - R_f)Re_\Lambda$. Panel ($a$) shows data for Cases 3, 4, 7 and 9 at a height of $z = 0.6$, while panel (b) shows data for Case 3 at various heights. The data for all cases collapse convincingly with this scaling. The results are also independent of z for $z = 0.3$–0.7. At $z = 0.9$ the data follow the scaling up to $Re_b \approx 100$ but then diverge. As seen in § 8, $Re_b \approx 100$ corresponds to the point in the flow evolution where the flow moves away from local equilibrium at this height, so that the assumptions underlying the derivation of (9.18) no longer hold.

10. Relationships between local flow parameters and friction Richardson number

For channel flow it is useful to find relationships between local flow parameters and bulk flow parameters since bulk parameters are often what is measured in field studies or predicted by large scale models. By analogy to the gradient Richardson number

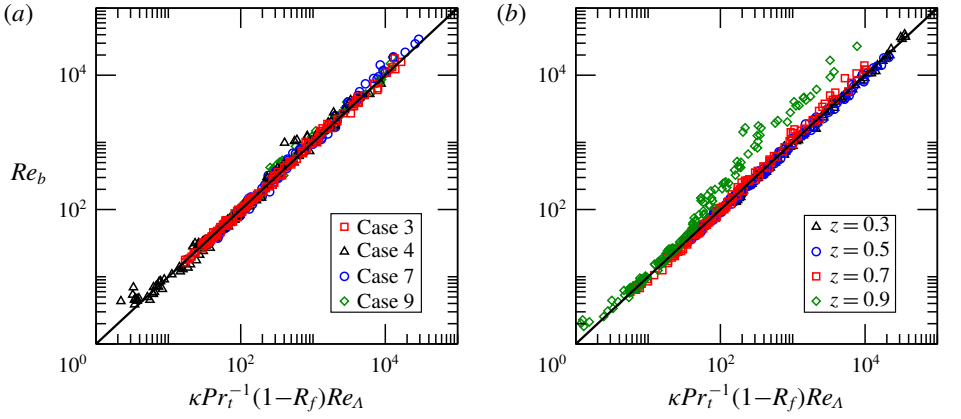

FIGURE 24. (Colour online) Local Monin–Obukhov scaling for Re_b in terms of Re_Λ. (*a*) Shows data for Cases 3, 4, 7 and 9 at a height of $z = 0.6$. (*b*) Shows data for Case 3 at various heights. The solid lines are $Re_b = \kappa Pr_t^{-1}(1 - R_f)Re_\Lambda$.

Ri, the friction Richardson number Ri_τ can be interpreted as the ratio of the mean buoyancy gradient in the channel to the mean shear at the wall, that is,

$$Ri_\tau = \frac{\gamma \Delta\phi}{h} \Big/ \left(\frac{u_\tau}{h}\right)^2. \tag{10.1}$$

As such, it is a bulk measure of the strength of stratification within the channel relative to the shear.

Figure 25 shows $\mathcal{Q}$, R_f, k_h and $\mathcal{F}$ plotted against Ri_τ at $z = 0.5$ for Cases 3, 4, 7 and 9. The short initial 'ramps' seen in the trajectories where the data do not collapse correspond to the early stage in which the flow relaxes in response to sudden removal of the heat source. As discussed above, during this early period the flow is also affected by the value of the stability parameter λ_0 for the initial state. Excluding the ramps, the data for each of the parameters collapse convincingly when plotted against Ri_τ.

In (*a*) it can be seen that $\mathcal{Q}$ follows relationships of the form

$$\mathcal{Q} = CRi_\tau^n, \tag{10.2}$$

where the exponent $n = -2/3$ for $Ri_\tau > 2$ and -1 for $Ri_\tau < 2$. Thus there is clearly a close relationship between the local parameter $\mathcal{Q}$, which has been found above be a dominant parameter governing local turbulence dynamics, and the bulk parameter Ri_τ. At this height in the channel the dotted line representing $\mathcal{Q}_{tr} = 0.15$ intersects the data at approximately $Ri_\tau = 100$. Thus the transition away from the linear Osborn relationship, $k_h = \Gamma\mathcal{Q}$, occurs for $Ri_\tau > 100$ at this height.

The $\mathcal{Q} = Ri_\tau^{-1}$ power law for the very weakly stratified regime ($Ri_\tau < 2$) can be explained with the following scaling argument. Expanding $\mathcal{Q}$ gives

$$\mathcal{Q} = \frac{Re_b}{Re_\tau} = \frac{\varepsilon}{\nu N^2}\frac{\nu}{u_\tau h} = \frac{\varepsilon}{u_\tau N^2 h}. \tag{10.3}$$

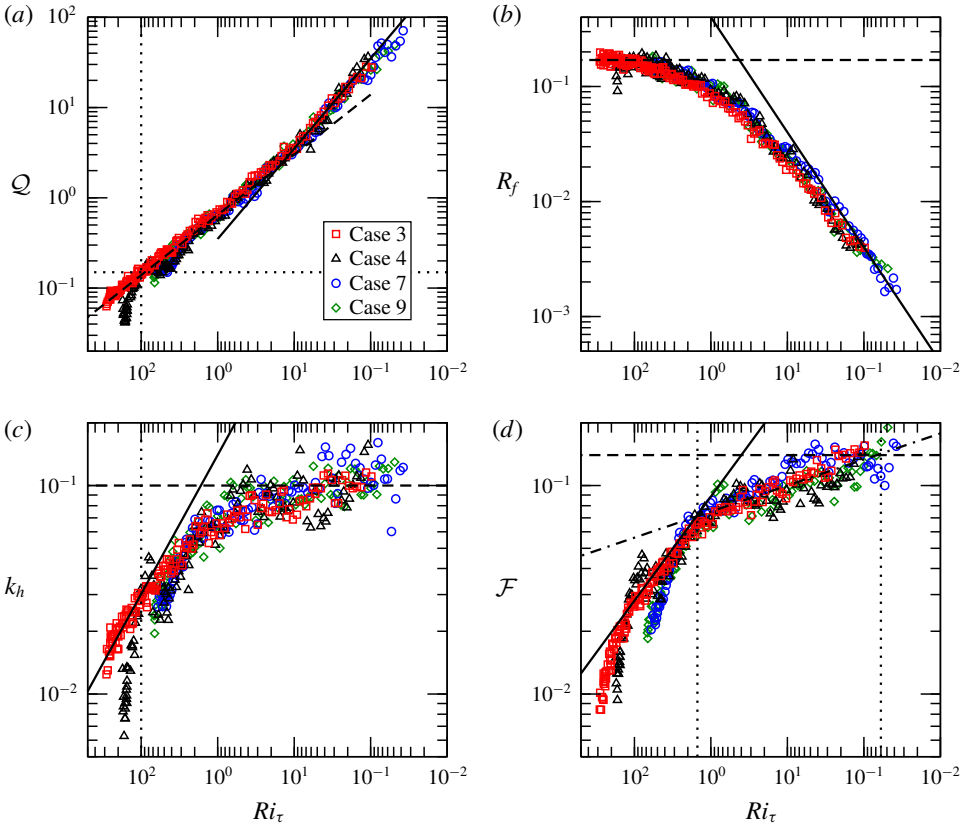

FIGURE 25. (Colour online) $\mathcal{Q}$, R_f, k_h and $\mathcal{F}$ plotted against Ri_τ at $z = 0.5$ for Cases 3, 4, 7 and 9. In (*a*) the dashed line is $\mathcal{Q} = 3Ri_\tau^{-2/3}$ and the solid line $\mathcal{Q} = 3.3Ri_\tau^{-1}$. In (*b*) the dashed line is $R_f = R_{f,c} = 0.17$ and the solid line $R_f = 0.04Ri_\tau$. In (*c*) the dashed line is $k_h = k_{h,c} = 0.1$ and the solid line $k_h = 0.65Ri_\tau^{-2/3}$. In (*d*) the dashed line is $\mathcal{F} = 0.14$, the dot-dashed line $\mathcal{F} = 0.1Ri_\tau^{-1/8}$ and the solid line $\mathcal{F} = 0.28Ri_\tau^{-1/2}$. The dotted lines in (*a*,*c*) correspond to $Ri_\tau = 100$ and $\mathcal{Q} = \mathcal{Q}_{tr} = 0.15$. The dotted lines in (*d*) represent $Ri_\tau = 15$ and $Ri_\tau = 0.06$. Note that the values of Ri_τ are plotted from highest to lowest.

Buoyancy frequency scales with the average buoyancy gradient across the channel $N^2 \sim \gamma \Delta\phi/h$, and for weakly stratified flow $\varepsilon \sim u_\tau^3/h$, which gives

$$\mathcal{Q} \sim \frac{u_\tau^2}{\gamma \Delta\phi h} = Ri_\tau^{-1}. \tag{10.4}$$

The relationship between R_f and Ri_τ shown in (*b*) is qualitatively similar to the relationship between R_f and $\mathcal{Q}$ shown in figure 17 and approaches a power law relationship $R_f = 0.035Ri_\tau$ for small Ri_τ. This is consistent with the fact that R_f was found to approach an asymptotic relationship of the form and $R_f \sim \mathcal{Q}^{-1}$ for large $\mathcal{Q}$, while from (*a*), $\mathcal{Q} \sim Ri_\tau^{-1}$ for small Ri_τ. The transition towards this relationship is gentler in the case of R_f and Ri_τ due to the fact that $\mathcal{Q} \sim Ri_\tau^{-2/3}$ for $Ri_\tau > 2$. The linear relationship between R_f and Ri_τ implies that local fluxes and large scale gradients approach a linear relationship as the stratification becomes very weak.

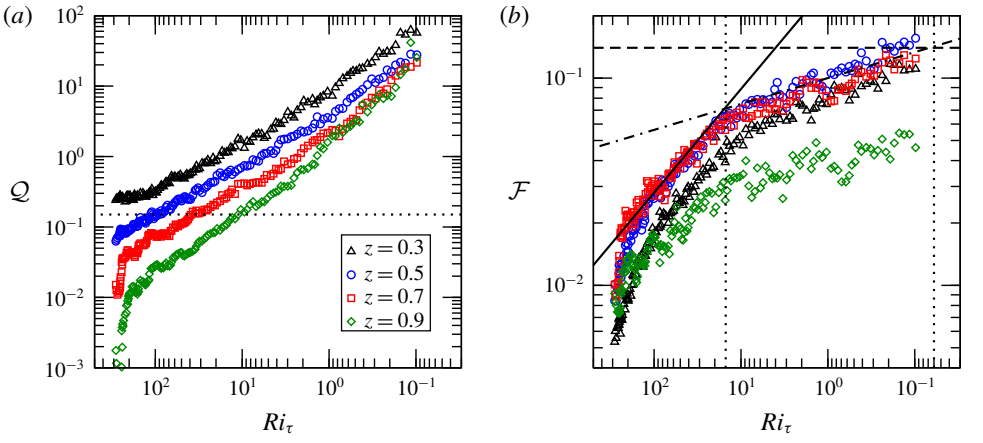

FIGURE 26. (Colour online) $\mathcal{Q}$ and $\mathcal{F}$ plotted against Ri_τ at various heights for Case 3. The lines are the same as those given in figure 25 and represent the best fit to the data at $z = 0.5$.

The relationship between k_h and Ri_τ shown in (*c*) is similar to the relationship between k_h and $\mathcal{Q}$ shown in figure 17. For $Ri_\tau > 100$ (that is the linear Osborn region, $\mathcal{Q} < \mathcal{Q}_{tr} = 0.15$) it follows a power law relationship, $k_h = 0.65 Ri_\tau^{-2/3}$, which is consistent with the combination of $k_h \sim \mathcal{Q}$ and $\mathcal{Q} \sim Ri_\tau^{-2/3}$.

The data for $\mathcal{F}$ shown in (*d*) follow similar trends to that of k_h. Here we have delineated two regions. For $Ri_\tau > 15$, data for $\mathcal{F}$ fit well to the relationship $\mathcal{F} = 0.28 Ri_\tau^{-1/2}$. For $Ri_\tau < 15$, $\mathcal{F}$ follows the relationship $\mathcal{F} = 0.1 Ri_\tau^{-1/8}$ as it approaches its asymptotic value of $\mathcal{F} = 0.14$. These two functions intersect at $Ri_\tau = 0.06$.

Consistent with the results presented in § 7, the relationships between the local parameters k_h, R_f, $\mathcal{F}$ and $\mathcal{Q}$ and the bulk parameter Ri_τ appear to be independent of Re_τ, λ_0 and α_0, while there is a dependence of k_h, R_f and $\mathcal{F}$ on Pr in the very weakly stratified regime ($Ri_\tau < 2$). The relationship between $\mathcal{Q}$ and Ri_τ, however, appears to be independent of Pr. This is consistent with the scaling argument presented in (10.3)–(10.4) above.

Since Ri_τ is a bulk parameter, the relationships between local parameters and Ri_τ are not independent of height within the channel. This can be seen in figure 26, which shows $\mathcal{Q}$ and $\mathcal{F}$ plotted against Ri_τ at various heights across the channel for Case 3. The curves of $\mathcal{Q}$ shown in (*a*) show a monotonic decrease in $\mathcal{Q}$ with height from $z = 0.3$ to $z = 0.9$. In the central region of the channel ($0.3 < z < 0.7$) the curves of $\mathcal{Q}$ follow similar gradients, indicating that the exponent remains unchanged in this region. In the near-surface region at $z = 0.9$ the exponents in the power law relationship are somewhat higher. The curves for $\mathcal{F}$ shown in (*b*) are of particular interest in the context of the destratification of the flow. The rate of change of temperature in a horizontal layer is equal to the flux divergence, or $\partial F/\partial z$. Thus the difference between the $\mathcal{F}(z, Ri_\tau)$ curves for two different heights gives an indication of the rate of change of temperature in the layer between those two heights relative to the bulk temperature difference across the channel at that time.

11. Destratification rate

The finding in the previous section that the vertical heat flux $\mathcal{F}$ scales with Ri_τ suggests that the bulk destratification rate in the channel should also be related to Ri_τ.

Noting that the flow is horizontally homogeneous, the energy equation, (2.25), can be averaged in $x-y$ planes to give an equation for the rate of change of the horizontally averaged temperature,

$$\frac{\partial\overline{\phi}}{\partial t}=\sigma\frac{\partial^2\overline{\phi}}{\partial z^2}-\frac{\partial(\overline{\phi'w'})}{\partial z}. \tag{11.1}$$

As with the full set of governing equations, (2.23)–(2.25), due to the fact that dependent variables here are non-dimensionalised in terms of the time-varying friction velocity u_τ, this equation cannot be integrated in time. It does, however, give a function for the time rate of change, $\partial\overline{\phi}/\partial t$, relative to a characteristic friction time scale, $\tilde{t}_\tau=\tilde{h}/\tilde{u}_\tau$, determined from flow conditions at a particular instant in 'measured time', $\hat{t}$. Thus, t is used only within differentials ∂t and dt, while $\hat{t}$ refers to the point in time within the process at which the particular set of flow conditions occur.

The first term on the right-hand side of (11.1) represents molecular diffusion, while the second term is the turbulent heat flux, which, as noted above, can be modelled in terms of the turbulent diffusivity k_h and the temperature gradient to give

$$\frac{\partial\overline{\phi}}{\partial t}=\frac{\partial}{\partial z}\left([\sigma+k_h(z,\hat{t})]\frac{\partial\overline{\phi}}{\partial z}\right). \tag{11.2}$$

Defining the total diffusivity as $k_t(z,\hat{t})=\sigma+k_h(z,\hat{t})$ gives

$$\frac{\partial\overline{\phi}}{\partial t}=\frac{\partial}{\partial z}\left(k_t(z,\hat{t})\frac{\partial\overline{\phi}}{\partial z}\right). \tag{11.3}$$

This is a one-dimensional heat diffusion equation for which we require a solution subject to adiabatic boundary conditions, $\partial\overline{\phi}/\partial z=0$ at $z=0$ and 1, and the temperature profile at a particular time $\hat{t}$ (see figure 6). Dimensional analysis indicates that the rate of change of the temperature difference across the channel $\Delta\phi$ at time $\hat{t}$ is characterised by a diffusion time scale of the form,

$$t_d(\hat{t})=\frac{k_*(\hat{t})}{h^2}, \tag{11.4}$$

where $k_*(\hat{t})$ is a representative diffusivity across the channel at time $\hat{t}$. This gives an equation for the destratification rate,

$$\frac{\mathrm{d}(\Delta\phi)}{\mathrm{d}t}=-k_*(\hat{t})\frac{\Delta\phi}{h^2}. \tag{11.5}$$

We define a normalised destratification rate as

$$\mathcal{D}(\hat{t})=-\frac{1}{\Delta\phi(\hat{t})}\frac{\mathrm{d}(\Delta\phi(\hat{t}))}{\mathrm{d}t}. \tag{11.6}$$

Combining this with (11.5), gives

$$\mathcal{D}(\hat{t})=k_*(\hat{t})/h^2. \tag{11.7}$$

Clearly the representative diffusivity $k_*(\hat{t})$ must be a function of $k_t(z,\hat{t})$, however, because $k_t(z,\hat{t})$ varies with z, and sits within the outer differentiation operator $\partial/\partial z(\cdot)$ in (11.3), it will also be a function of the temperature gradient profile $\partial\overline{\phi}(z,\hat{t})/\partial z$.

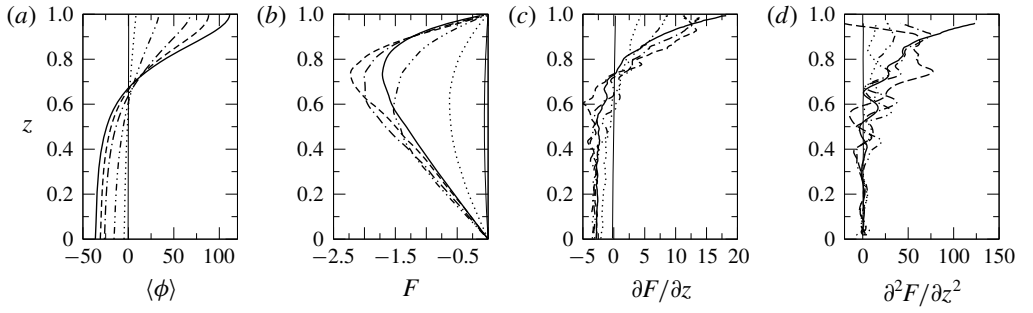

FIGURE 27. Destratification profiles for Case 3. Legend as for figure 6.

In order to investigate this relationship more closely we recast the horizontally averaged energy equation (11.1) in terms of the total heat flux through a horizontal layer at height z, defined in § 7 as

$$F = -\sigma \frac{\partial \overline{\phi}}{\partial z} + \overline{\phi' w'} \equiv -k_t \frac{\partial \overline{\phi}}{\partial z}. \tag{11.8}$$

Substituting into (11.1) gives

$$\frac{\partial \overline{\phi}(z, \hat{t})}{\partial t} = -\frac{\partial F(z, \hat{t})}{\partial z}, \tag{11.9}$$

and then differentiating both sides with respect to z gives

$$\frac{\partial^2 \overline{\phi}(z, \hat{t})}{\partial z \partial t} = -\frac{\partial^2 F(z, \hat{t})}{\partial z^2}. \tag{11.10}$$

Integrating this expression across the channel,

$$\frac{\mathrm{d}}{\mathrm{d}t} \int_0^h \frac{\partial \overline{\phi}(z, \hat{t})}{\partial z} \, \mathrm{d}z = -\int_0^h \frac{\partial^2 F(z, \hat{t})}{\partial z^2} \, \mathrm{d}z, \tag{11.11}$$

gives

$$\frac{\mathrm{d}(\Delta \phi)}{\mathrm{d}t}(\hat{t}) = -\frac{1}{h} \int_0^h \frac{\partial^2 F(z, \hat{t})}{\partial z^2} \, \mathrm{d}z, \tag{11.12}$$

which can be recast in terms of $\mathcal{D}$ and $\mathcal{F}$ as

$$\mathcal{D}(\hat{t}) = \frac{1}{h} \int_0^h \frac{\partial^2 \mathcal{F}(z, \hat{t})}{\partial z^2} \, \mathrm{d}z. \tag{11.13}$$

Figure 27 shows vertical profiles of $\langle \phi \rangle$, F, $\partial F/\partial z$ and $\partial^2 F/\partial z^2$ for Case 3. Here, like $\langle \phi \rangle$, the fluxes were averaged over one time unit as well as horizontal planes in order to improve convergence of statistics, as was done for the vertical profiles presented in § 5. For convenience the angled brackets are not shown. These profiles give an overview of the mechanics of the destratification process from the perspective of horizontal layers.

Panel (*a*) shows that the height $z \approx 0.65$ represents a nodal plane for the process. Above this height the temperature $\langle\phi\rangle$ decreases with time, while below this height the temperature increases. The temperature at $z \approx 0.65$ remains constant.

The total heat flux F shown in (*b*) is downwards across the entire channel, with heat being transferred down the temperature gradient.

As noted above, the flux divergence, $\partial F/\partial z$, shown in (*c*) is equal to the time rate of change of temperature at a given horizontal layer, $\partial\overline{\phi}/\partial t$. This panel shows that the layers close to the surface generally have the highest rate of temperature change and that this rate of change decreases with time.

The profile at $\hat{t} = 0$ also represents the flux divergence profile for the heated equilibrium state. Here the heated equilibrium flow is statistically stationary so $\partial\overline{\phi}(z, \hat{t})/\partial t = 0$ and the flux divergence balances the radiative heat source. As a result, the profile of $\partial F/\partial z$ is exponential matching the Beer–Lambert law.

The profile of $\partial^2 F/\partial z^2$ is shown in (*d*). As this is a second derivative and there is limited scope for averaging in the time evolving flow, the raw profile is very noisy. We have filtered this noise by applying a thirty point running average so that the trends can be seen. Consequently, data are truncated close to the top and bottom of the channel.

As discussed above, the representative diffusivity $k_*(\hat{t})$ and destratification rate $\mathcal{D}(\hat{t})$ at time $\hat{t}$ are equal to the integral of $\partial^2 F/\partial z^2$ across the channel divided by $\Delta\phi(\hat{t})$. Thus the profile of $\partial^2 F/\partial z^2$ gives an indication of the regions of the channel that make the most significant contributions to $k_*(\hat{t})$ and $\mathcal{D}(\hat{t})$. The profiles indicate that, for most of the destratification process, the region above $z = 0.3$ makes the most significant contribution, while the region close to the lower wall boundary makes only a very small contribution. The dominant contribution comes from the region $z = 0.6$–0.9.

In previous sections we have shown that in the central region, $z = 0.3$–0.7, $\mathcal{F}$ is a function of Ri_τ and Pr, while in the near-surface region (at least up to $z = 0.9$) it is a function of Ri_τ only. From (11.13) it is clear that the normalised destratification rate $\mathcal{D}$ is a function of $\mathcal{F}$. Thus we expect $\mathcal{D}$ also to be a function of Ri_τ and Pr.

Figure 28 shows the normalised destratification rate $\mathcal{D}$ as a function of Ri_τ for all simulation cases. Apart from the initial ramps that correspond to the early relaxation period, the data collapse well for all cases. The Prandtl number dependence seen in $\mathcal{F}$ is reflected in $\mathcal{D}$, with higher destratification rates at lower Pr in the weakly stratified regime.

Based on this we suggest the following empirical power law approximations to the data over three ranges:

$$\mathcal{D} = 1.1; \quad Ri_\tau < 0.06, \tag{11.14a,b}$$

$$\mathcal{D} = 0.78 Ri_\tau^{-1/8}; \quad 0.06 \leqslant Ri_\tau \leqslant 15, \tag{11.15a,b}$$

$$\mathcal{D} = 2.1 Ri_\tau^{-1/2}; \quad Ri_\tau > 15. \tag{11.16a,b}$$

As expected, there are clear similarities in the relationship between $\mathcal{D}$ and Ri_τ and that between $\mathcal{F}(z, \hat{t})$ and Ri_τ shown in figure 25. The exponents in the power law relations and the values of the transitional values of Ri_τ are the same. Clearly the range of data for $Ri_\tau < 0.06$ are very limited. The value of $\mathcal{D} = 1.1$ given for this range was determined using Case 11 in which $\lambda_0 = 0$ and hence $Ri_\tau = 0$. For this case the average destratification rate was found to be 1.1. These relations do not include any dependence on Prandtl number. Accurate determination of such a dependence would require simulations over a larger Pr range and is left to a future study.

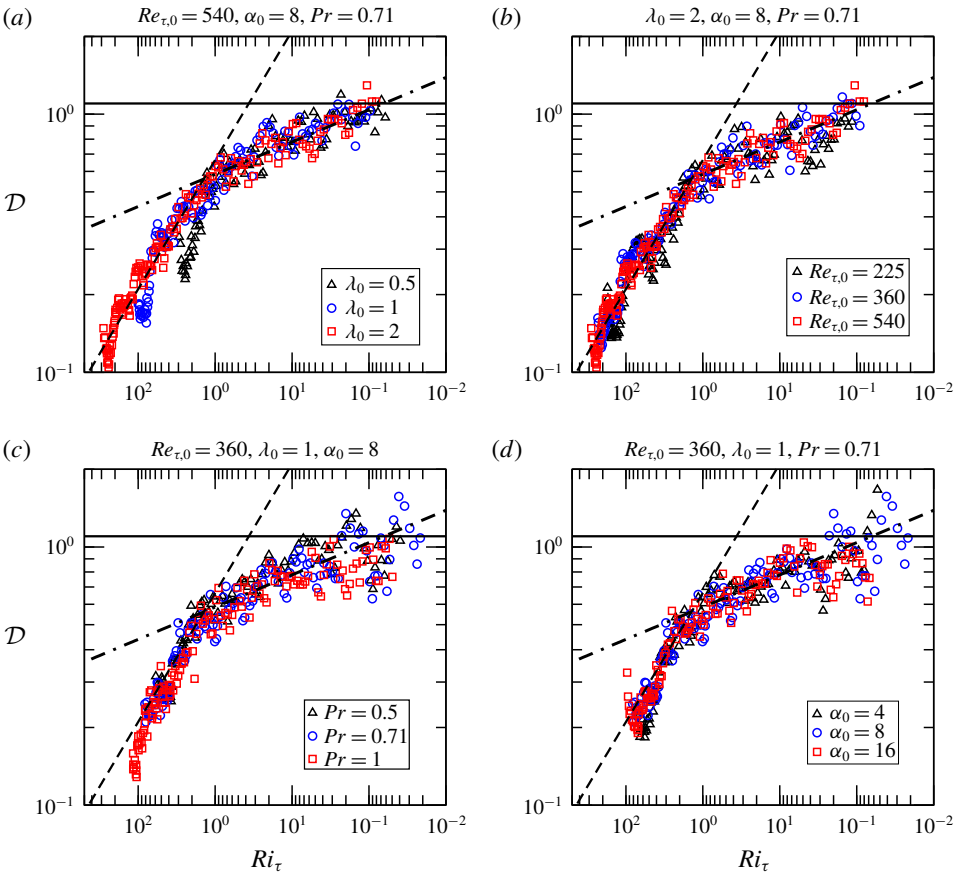

FIGURE 28. (Colour online) Normalised destratification rate $\mathcal{D}$ plotted against Ri_τ for Cases 1–10. The solid line is $\mathcal{D} = 1.1$, the dot-dashed line $\mathcal{D} = 0.78Ri_\tau^{-1/8}$, and the dashed line $\mathcal{D} = 2.1Ri_\tau^{-1/2}$.

12. Concluding remarks

This paper has presented a study of destratification of thermally stratified open channel flow after removal of the heat source. The radiative heat source in the initial heated equilibrium state acts as a sink for potential energy and is in balance with turbulent kinetic energy generated by shear within the channel. This leads to a flow in which turbulence in the central region of the channel is in a state of energetic equilibrium, with shear production balanced by viscous dissipation and buoyancy flux.

Stable stratification due to the heat source reduces turbulent momentum fluxes. Due to the exponential nature of the heat source, this effect is most pronounced close to the upper surface. As a result, a laminar surface layer forms close to the top of the channel leading to a strongly inflected mean velocity profile and associated shear layer in this region. Due to the inflected velocity profile, the stratified flow contains a surplus of mean flow kinetic energy relative to a neutral flow with the same streamwise pressure gradient.

Sudden removal of the heat source leads to a change in the energy balance within the channel. As a result, energy transfers must readjust to the new conditions. The flow undergoes an initial relaxation period during which the laminar layer close to

the surface destabilises driving a rapid transition to turbulence. The resultant increase in shear production opens up a pathway by which energy is transferred from mean flow kinetic energy to the turbulent kinetic energy field, and from there via reversible and irreversible buoyancy fluxes into background potential energy. For the remainder of the destratification process energy transfers along this pathway are approximately in balance and the region of energetic equilibrium seen in the initial state extends up close to the surface before gradually contracting again as the process proceeds.

We proposed the following explanation for the rapid destabilisation of the laminar surface layer seen during the initial relaxation period. In the initial state the potential energy sink provides an extra stabilising influence on the laminar surface layer by absorbing small perturbations before they are able to grow and become unstable. As a result, the lower section of this layer has a gradient Richardson number that is well below the critical gradient Richardson number $Ri_m = 1/4$ determined by Howland *et al.* (2018) for marginal stability of an unheated fluid layer with respect to Kelvin–Helmholtz instabilities. Removal of the heat source results in the lower section of the laminar surface layer suddenly becoming unstable to small perturbations, leading to the rapid formation of K–H-like instabilities.

This proposed mechanism is supported by visualisations of the flow, which show that a layer of intense Kelvin–Helmholtz-like shear instabilities forms within this region during the initial stages of the flow evolution. Quantitative evidence is seen in a localised increase in flux Richardson number in this layer and as well as an increase in available potential energy, both of which are have been found by authors such as Winters *et al.* (1995) to be associated with Kelvin–Helmholtz instabilities. The enhanced mixing efficiency due to the K–H-like instabilities causes vigorous entrainment of the overlying laminar layers leading to a rapid transition to turbulence up to the top of the channel.

The central region of the channel, $0.3 \lessapprox z \lessapprox 0.7$, remains in energetic equilibrium until late in the destratification process. In this region the flow exhibits behaviour similar to that seen in homogeneous stratified shear flow. For low Re_b, the normalised eddy diffusivity $k_h/\nu \equiv \tilde{k}_h/\tilde{\nu}$ scales linearly with Re_b, $k_h/\nu = \Gamma Re_b$ where $\Gamma = 0.2$, in accordance with the model of Osborn (1980). For high Re_b, k_h/ν approaches asymptotic values that are consistent with the scaling relationship $k_h/\nu \approx (\kappa l_c/\eta)^{4/3} Pr_{t,n}^{-1}$ derived by Chung & Matheou (2012) for homogeneous stratified shear flow. These relationships are, however, dependent on Re_τ.

For channel flow, since η scales with Re_τ, this asymptotic value varies with Re_τ. From the scaling relationship of Chung & Matheou (2012) above, we show that this effect can be accounted for by reformulating the relations in terms of a non-dimensional eddy diffusivity $k_h \equiv \tilde{k}_h/(\tilde{u}_\tau \tilde{h})$ and a non-dimensional parameter, $\mathcal{Q} \equiv Re_b/Re_\tau$. This scaling gives the correct dependence of k_h/ν on Re_τ in the weakly stratified regime ($\mathcal{Q} \gg \mathcal{Q}_{tr} = 0.15$), approaching a single asymptotic value $k_{h,c} \approx 0.1$, while reverting to the Re_τ-independent linear Osborn model, $k_h = \Gamma \mathcal{Q}$, in strongly stratified conditions ($\mathcal{Q} \lessapprox \mathcal{Q}_{tr} = 0.15$).

Using $\mathcal{Q}$ also accounts for Re_τ effects on other local parameters such as the flux Richardson number R_f and gradient Richardson number Ri. For strongly stratified conditions, $\mathcal{Q} < 0.15$, R_f remains constant at a critical value of $R_{f,c} \approx 0.17$, while for very weakly stratified conditions it approaches an inverse linear relation, $R_f = 0.1\mathcal{Q}^{-1}$. The exponent here differs from the exponent $n = -1/2$ to $-2/3$ commonly reported for geophysical flows; however, it is consistent with the theoretical analysis of Scotti & White (2016), who demonstrate that there is no justification for a universal relationship between R_f and Re_b. In the context of bounded flows, R_f must also be

affected by the externally imposed confinement scale, with this effect becoming more dominant as the ratio of buoyancy length scale to confinement scale increases.

Within the central region of the channel all these relationships are shown to be independent of height as well as the parameters Re_τ, λ_0 and α_0. The data do, however, indicate a dependence on Pr in the weakly stratified regime. We suggest that this is due to the effect of Pr on the ratio between turbulent and viscous heat fluxes and the mean vertical temperature gradient within the channel.

We also investigated these parameter relationships in upper region of the channel, $0.7 \lessapprox z \lessapprox 1$. At a height, $z = 0.9$, qualitatively similar relationships are observed to those seen in the central region; however, k_h and R_f are reduced as a result of constraints imposed on turbulent motions due to the proximity to the surface. Nevertheless, k_h and R_f are found to scale with $\mathcal{Q}$ independent of λ_0, and α_0. As expected there is, however, some dependence on Re_τ and Pr in this region as viscous effects become important.

Given that the overarching aim of this paper is to determine the destratification rate, we defined a normalised total heat flux, $\mathcal{F} = F/\Delta\phi$, where $\Delta\phi$ is the temperature difference across the channel and F the sum of the turbulent and molecular heat fluxes. This flux also scales with $\mathcal{Q}$ and exhibits a Prandtl number dependence in a manner similar to k_h.

As described by Williamson *et al.* (2015), the stability of the heated equilibrium flow is governed by a parameter λ_0 formed as the ratio of the channel height h to an Obukhov length scale $\mathcal{L}$ based on the radiative heat source. In the destratifying flow there is no heat source and the flow is evolving in time. We found, however, that an Obukhov length scale formed using the friction velocity u_τ and the maximum total buoyancy flux in the channel at a given time is useful in describing local turbulence. We compared our data to a variety of scalings based on Monin–Obukhov theory and found good agreement with these scalings.

Williamson *et al.* (2015) show that the equilibrium flow is governed by four parameters, $Re_{\tau,0}$, λ_0, Pr and α_0. For the destratifying flow in which the heat source is removed, λ_0 no longer determines the stability of the flow. Given the similarity in form between λ_0 and a friction Richardson number Ri_τ, we proposed that Ri_τ can be used to describe the stability of the destratifying flow. Analysis of our DNS data shows that this is indeed the case, with local turbulence quantities $\mathcal{Q}$, k_h, R_f and $\mathcal{F}$ scaling with Ri_τ, independent of Re_τ, λ_0 and α_0. Again, there is a small dependence on Pr in the weakly stratified regime. Noting that, within the context of our non-dimensionalisation scheme, $\mathcal{Q}$ and k_h have an implicit dependence on Re_τ, we conclude that the destratifying flow is governed by bulk parameters Ri_τ, Re_τ and Pr, with λ_0 and α_0 having an effect only through the initial conditions and during the brief initial relaxation period.

Finally, based on these relationships we used scaling analysis to show that the bulk destratification rate $\mathcal{D}$ in the channel is expected to be a function of Ri_τ and Pr. Our DNS data indicate that this is indeed the case. Based on these data we have determined approximations to this function in the form of power law relationships, $\mathcal{D} \approx CRi_\tau^{-n}$.

Given the small range of Prandtl numbers used in this study we have not been able to determine a scaling relationship for this parameter. We can, however, state that destratification rate decreases with increasing Pr. A quantitative scaling relationship might be determined through a future study in which simulations or experiments are performed over a larger range of Pr.

Similarly, whilst a dependence of destratification rate on Reynolds number is not apparent in our results, again, these results are for a small range of relatively

low Reynolds numbers. The Reynolds number of typical stratified river flows is significantly higher ($Re_\tau = O(10\,000)$), so even a small Reynolds number dependence would have an effect.

Thus, before using the destratification scaling relationship proposed here for predicting destratification in rivers, it is necessary to first assess its validity against field or experimental measurements taken at values of Re_τ and Pr comparable with actual thermally stratified river flows.

Acknowledgements

The authors gratefully acknowledge the support of the Australian Research Council (ARC). The research in this paper was supported by ARC Discovery Project DP150100912. The authors also acknowledge the National Computational Infrastructure (NCI) which is supported by the Australian Government, and the Sydney Informatics Hub and high performance computing cluster, Artemis, at the University of Sydney, for providing high performance computing resources and services that have contributed to the research results reported within this paper. Finally, we would also like to thank the reviewers for useful suggestions that have strengthened this paper.

Appendix A

This appendix discusses our approach for dealing with a time-varying coefficient of friction.

As the flow destratifies, changes in the balance between turbulent and laminar shear stresses within the channel result in the mean velocity profile evolving from an initial inflected profile towards a non-inflected neutral boundary layer profile. This leads to an increase in the coefficient of friction, $C_f = 2(\tilde{u}_\tau/\tilde{U}_b)^2$.

Because our simulations are driven by a constant pressure gradient, this change in C_f leads to an increase in the actual friction velocity $\hat{u}_\tau(\hat{t})$ measured at the bottom boundary in the simulations. Here $\hat{\cdot}$ is used to refer to the actual value of a variable measured in the simulation. The increased wall shear stress then decelerates the flow leading to a decrease in the bulk velocity. Eventually $\hat{u}_\tau$ decreases again towards a value of unity that is in balance with the applied pressure gradient. The increase in $\hat{u}_\tau$ depends primarily on λ_0, reaching peak values of approximately 1.06, 1.11 and 1.23 for the $\lambda_0 = 0.5$, 1 and 2 cases, respectively.

Whilst in our simulations the channel height $\hat{h}$ remains constant at $\hat{h} = h_0$, in a physical channel flow the height of the fluid in the channel will typically also vary in response to a change in C_f, so we have included the possibility of time-varying $\hat{h}(\hat{t})$ explicitly in our formulation to allow comparison with physical flows.

The governing equations given in § 2.2 are non-dimensionalised in terms of the time-varying length scale $\tilde{h}(\tilde{t})$ and velocity scale $\tilde{u}_\tau(\tilde{t})$, and the temperature scale associated with the initial equilibrium state $\tilde{\Phi}_{N,0}$. Due to the time-varying scales, these equations cannot actually be solved directly. Instead we solve the set of equations with length and velocity scales frozen at their initial values, that is,

$$\frac{\partial \hat{u}_j}{\partial \hat{x}_j} = 0, \tag{A 1}$$

$$\frac{\partial \hat{u}_i}{\partial \hat{t}} + \frac{\partial \hat{u}_i \hat{u}_j}{\partial \hat{x}_j} = -\frac{\partial \hat{p}}{\partial \hat{x}_i} + \hat{\nu}\frac{\partial^2 \hat{u}_i}{\partial \hat{x}_j^2} + \delta_{i1} + \hat{\gamma}\hat{\phi}\delta_{i3}, \tag{A 2}$$

$$\frac{\partial \hat{\phi}}{\partial \hat{t}} + \frac{\partial \hat{\phi}\hat{u}_j}{\partial \hat{x}_j} = \hat{\sigma}\frac{\partial^2 \hat{\phi}}{\partial \hat{x}_j^2}. \tag{A 3}$$

The variables in the above equations are normalised with respect to the friction velocity $\tilde{u}_{\tau,0}$, characteristic temperature $\tilde{\Phi}_{N,0}$, and channel height $\tilde{h}_0$ of the initial state, that is

$$\left.\begin{aligned} \hat{u} = \frac{\tilde{u}}{\tilde{u}_{\tau,0}}, \quad \hat{\phi} = \frac{\tilde{\phi}}{\tilde{\Phi}_{N,0}}, \quad \hat{p} = \frac{\tilde{p}}{\tilde{\rho}_0 \tilde{u}_{\tau,0}^2} \quad \hat{x} = \frac{\tilde{x}}{\tilde{h}_0}, \quad \hat{t} = \frac{\tilde{u}_{\tau,0}}{\tilde{h}_0}\tilde{t}, \\ \hat{\nu} = \frac{\tilde{\nu}}{\tilde{u}_{\tau,0}\tilde{h}_0} \equiv \frac{1}{Re_{\tau,0}}, \quad \hat{\sigma} = \frac{\tilde{\sigma}}{\tilde{u}_{\tau,0}\tilde{h}_0} \equiv \frac{1}{Re_{\tau,0}Pr}, \quad \hat{\gamma} = \frac{\tilde{\beta}\tilde{g}\tilde{\Phi}_{N,0}\tilde{h}_0}{\tilde{u}_{\tau,0}^2}. \end{aligned}\right\} \tag{A 4}$$

In order to recover the solution to (2.23) to (2.25) formulated in terms of time varying $\tilde{h}(\tilde{t})$ and velocity scale $\tilde{u}_\tau(\tilde{t})$, we renormalise the solution according to the following scheme:

$$\left.\begin{aligned} u = \frac{\hat{u}}{\hat{u}_\tau(\hat{t})}, \quad \phi = \hat{\phi}, \quad p = \frac{\hat{p}}{\hat{u}_\tau^2(\hat{t})}, \quad x = \frac{\hat{x}}{\hat{h}(\hat{t})}, \quad \partial t = \frac{\hat{u}_\tau(\hat{t})\partial \hat{t}}{\hat{h}(\hat{t})}, \quad \hat{t} = \hat{t}, \\ \nu = \frac{\hat{\nu}}{\hat{u}_\tau(\hat{t})\hat{h}(\hat{t})}, \quad \sigma = \frac{\hat{\sigma}}{\hat{u}_\tau(\hat{t})\hat{h}(\hat{t})}, \quad \gamma = \frac{\hat{h}(\hat{t})\hat{\gamma}}{\hat{u}_\tau^2(\hat{t})}. \end{aligned}\right\} \tag{A 5}$$

This renormalisation scheme is derived by redimensionalising equations (A 1)–(A 3) and then non-dimensionalising them again in terms of the time-varying scales $\tilde{h}(\tilde{t})$ and $\tilde{u}_\tau(\tilde{t})$. For (A 1) and (A 3) this is equivalent to multiplying through by a factor

$$\frac{\tilde{u}_{\tau,0}}{\tilde{h}_0}\frac{\tilde{h}(\tilde{t})}{\tilde{u}_\tau(\tilde{t})} \equiv \frac{\hat{h}(\hat{t})}{\hat{u}_\tau(\hat{t})}, \tag{A 6}$$

while for (A 2) the transformation requires multiplication by

$$\frac{\tilde{u}_{\tau,0}^2}{\tilde{h}_0}\frac{\tilde{h}(\tilde{t})}{\tilde{u}_\tau^2(\tilde{t})} \equiv \frac{\hat{h}(\hat{t})}{\hat{u}_\tau^2(\hat{t})}. \tag{A 7}$$

This results in the governing equations formulated in terms of the time varying $\tilde{h}(\tilde{t})$ and velocity scale $\tilde{u}_\tau(\tilde{t})$ given in (2.23) to (2.25).

Note that multiplication of the equations in this fashion implies a renormalisation of the time differential ∂t only, as shown in (A 5), since

$$\partial t = \frac{\hat{u}_\tau(\hat{t})}{\hat{h}(\hat{t})}\partial \hat{t} \neq \partial\left(\frac{\hat{u}_\tau(\hat{t})}{\hat{h}(\hat{t})}\hat{t}\right). \tag{A 8}$$

As a result, we can interpret our renormalised solutions as a series of 'snapshots' of the flow that have been normalised in terms of a characteristic friction time scale

$\tilde{t}_\tau = \tilde{h}/\tilde{u}_\tau$ based on the flow conditions in that particular instant in 'measured time', $\hat{t}$. For this reason, when results are presented we give them in terms of measured time $\hat{t}$ rather than a renormalised time.

REFERENCES

BELL, J. B., COLELLA, P. & GLAZ, H. M. 1989 A second-order projection method for the incompressible Navier–Stokes equations. *J. Comput. Phys.* **85** (2), 257–283.

BLUTEAU, C. E., JONES, N. L. & IVEY, G. N. 2013 Turbulent mixing efficiency at an energetic ocean site. *J. Geophys. Res.* **118** (9), 4662–4672.

BORMANS, M., FORD, P. W. & FABBRO, L. 2005 Spatial and temporal variability in cyanobacterial populations controlled by physical processes. *J. Plankton Res.* **27** (1), 61–70.

BRETHOUWER, G., BILLANT, P., LINDBORG, E. & CHOMAZ, J.-M. 2007 Scaling analysis and simulation of strongly stratified turbulent flows. *J. Fluid Mech.* **585**, 343–368.

BRITTER, R. E. 1974 An experiment on turbulence in a density stratified fluid. PhD thesis, Monash University, Victoria, Australia.

BRUCKER, K. A. & SARKAR, S. 2007 Evolution of an initially turbulent stratified shear layer. *Phys. Fluids* **19** (10), 105105.

CALMET, I. & MAGNAUDET, J. 2003 Statistical structure of high-Reynolds-number turbulence close to the free surface of an open-channel flow. *J. Fluid Mech.* **474**, 355–378.

CAULFIELD, C. P. & PELTIER, W. R. 2000 The anatomy of the mixing transition in homogeneous and stratified free shear layers. *J. Fluid Mech.* **413**, 1–47.

CHUNG, D. & MATHEOU, G. 2012 Direct numerical simulation of stationary homogeneous stratified sheared turbulence. *J. Fluid Mech.* **696**, 434–467.

DEUSEBIO, E., CAULFIELD, C. P. & TAYLOR, J. R. 2015 The intermittency boundary in stratified plane Couette flow. *J. Fluid Mech.* **781**, 298–329.

DYER, A. J. 1974 A review of flux-profile relationships. *Boundary-Layer Meteorol.* **7** (3), 363–372.

ELLISON, T. H. 1957 Turbulent transport of heat and momentum from an infinite rough plane. *J. Fluid Mech.* **2** (5), 456–466.

FLORES, O. & RILEY, J. J. 2011 Analysis of turbulence collapse in the stably stratified surface layer using direct numerical simulation. *Boundary-Layer Meteorol.* **139** (2), 241–259.

FOKEN, T. 2006 50 years of the Monin–Obukhov similarity theory. *Boundary-Layer Meteorol.* **119** (3), 431–447.

GARCIA-VILLALBA, M. & DEL ALAMO, J. C. 2011 Turbulence modification by stable stratification in channel flow. *Phys. Fluids* **23** (4), 045104.

GARG, R. P., FERZIGER, J. H., MONISMITH, S. G. & KOSEFF, J. R. 2000 Stably stratified turbulent channel flows. I. Stratification regimes and turbulence suppression mechanism. *Phys. Fluids* **12** (10), 2569–2594.

GARGETT, A. E., OSBORN, T. R. & NASMYTH, P. W. 1984 Local isotropy and the decay of turbulence in a stratified fluid. *J. Fluid Mech.* **144**, 231–281.

HOKPUNNA, A. & MANHART, M. 2010 Compact fourth-order finite volume method for numerical solutions of Navier–Stokes equations on staggered grids. *J. Comput. Phys.* **229** (20), 7545–7570.

HOWLAND, C. J., TAYLOR, J. R. & CAULFIELD, C. P. 2018 Testing linear marginal stability in stratified shear layers. *J. Fluid Mech.* **839**.

HUNT, J. C. R. & GRAHAM, J. M. R. 1978 Free-stream turbulence near plane boundaries. *J. Fluid Mech.* **84** (2), 209–235.

IVEY, G. N., BLUTEAU, C. E. & JONES, N. L. 2018 Quantifying diapycnal mixing in an energetic ocean. *J. Geophys. Res.* **123** (1), 346–357.

IVEY, G. N. & IMBERGER, J. 1991 On the nature of turbulence in a stratified fluid. Part I: The energetics of mixing. *J. Phys. Oceanogr.* **21** (5), 650–658.

IVEY, G. N., WINTERS, K. B. & KOSEFF, J. R. 2008 Density stratification, turbulence, but how much mixing? *Annu. Rev. Fluid Mech.* **40** (1), 169–184.

KAMINSKI, A. K., CAULFIELD, C. P. & TAYLOR, J. R. 2017 Nonlinear evolution of linear optimal perturbations of strongly stratified shear layers. *J. Fluid Mech.* **825**, 213–244.

KAMINSKI, A. K. & SMYTH, W. D. 2019 Stratified shear instability in a field of pre-existing turbulence. *J. Fluid Mech.* **862**, 639–658.

VAN KAN, J. 1986 A second-order accurate pressure-correction scheme for viscous incompressible flow. *SIAM J. Sci. Stat. Comput.* **7** (3), 870–891.

KIM, J. & MOIN, P. 1989 Transport of passive scalars in a turbulent channel flow. In *Turbulent Shear Flows 6* (ed. J.-C. Andr, J. Cousteix, F. Durst, B. E. Launder, F. W. Schmidt & J. H. Whitelaw), pp. 85–96. Springer.

KIRKPATRICK, M. P. 2002 A large eddy simulation code for industrial and environmental flows. PhD thesis, University of Sydney.

LORENZ, E. N. 1955 Available potential energy and the maintenance of the general circulation. *Tellus* **7** (2), 157–167.

MATER, B. D. & VENAYAGAMOORTHY, S. K. 2014*a* The quest for an unambiguous parameterization of mixing efficiency in stably stratified geophysical flows. *Geophys. Res. Lett.* **41** (13), 4646–4653.

MATER, B. D. & VENAYAGAMOORTHY, S. K. 2014*b* A unifying framework for parameterizing stably stratified shear-flow turbulence. *Phys. Fluids* **26** (3), 036601.

MONIN, A. S. 1970 The atmospheric boundary layer. *Annu. Rev. Fluid Mech.* **2** (1), 225–250.

NIEUWSTADT, F. T. M. 1984 The turbulent structure of the stable, nocturnal boundary layer. *J. Atmos. Sci.* **41** (14), 2202–2216.

OSBORN, T. R. 1980 Estimates of the local state of vertical diffusion from dissipation measurements. *J. Phys. Oceanogr.* **10** (1), 83–89.

OSBORN, T. R. & COX, C. S. 1972 Oceanic fine structure. *Geophys. Fluid Dyn.* **3** (1), 321–345.

SALEHIPOUR, H. & PELTIER, W. R. 2015 Diapycnal diffusivity, turbulent Prandtl number and mixing efficiency in Boussinesq stratified turbulence. *J. Fluid Mech.* **775**, 464–500.

SCOTTI, A. & WHITE, B. 2016 The mixing efficiency of stratified turbulent boundary layers. *J. Phys. Oceanogr.* **46** (10), 3181–3191.

SHERMAN, B. S., WEBSTER, I. T., JONES, G. J. & OLIVER, R. L. 1998 Transitions between Auhcoseira and Anabaena dominance in a turbid river weir pool. *Limnol. Oceanogr.* **43**, 1902–1915.

SHIH, L. H., KOSEFF, J. R., FERZIGER, J. H. & REHMANN, C. R. 2000 Scaling and parameterization of stratified homogeneous turbulent shear flow. *J. Fluid Mech.* **412**, 1–20.

SHIH, L. H., KOSEFF, J. R., IVEY, G. N. & FERZIGER, J. H. 2005 Parameterization of turbulent fluxes and scales using homogeneous sheared stably stratified turbulence simulations. *J. Fluid Mech.* **525**, 193–214.

SMYTH, W. D. & MOUM, J. N. 2000 Length scales of turbulence in stably stratified mixing layers. *Phys. Fluids* **12** (6), 1327–1342.

TAYLOR, J. R., SARKAR, S. & ARMENIO, V. 2005 Large eddy simulation of stably stratified open channel flow. *Phys. Fluids* **17** (11), 116602.

TURNER, L. & ERSKINE, W. D. 2005 Variability in the development, persistence and breakdown of thermal, oxygen and salt stratification on regulated rivers of southeastern Australia. *River Res. Appl.* **21**, 151–168.

VAN BUREN, T., WILLIAMS, O. & SMITS, A. J. 2017 Turbulent boundary layer response to the introduction of stable stratification. *J. Fluid Mech.* **811**, 569–581.

VENAYAGAMOORTHY, S. K. & KOSEFF, J. R. 2016 On the flux Richardson number in stably stratified turbulence. *J. Fluid Mech.* **798**, R1.

WALTER, R. K., SQUIBB, M. E., WOODSON, C. B., KOSEFF, J. R. & MONISMITH, S. G. 2014 Stratified turbulence in the nearshore coastal ocean: dynamics and evolution in the presence of internal bores. *J. Geophys. Res.* **119** (12), 8709–8730.

WEBSTER, I. T., SHERMAN, B. S., BORMANS, M. & JONES, G. 2000 Management strategies for cyanobacterial blooms in an impounded lowland river. *Regul. Rivers: Res. Manage.* **16** (5), 513–525.

WILLIAMSON, N., ARMFIELD, S. W., KIRKPATRICK, M. P. & NORRIS, S. E. 2015 Transition to stably stratified states in open channel flow with radiative surface heating. *J. Fluid Mech.* **766**, 528–555.

WINTERS, K. B. & D'ASARO, E. A. 1996 Diascalar flux and the rate of fluid mixing. *J. Fluid Mech.* **317**, 179–193.

WINTERS, K. B., LOMBARD, P. N., RILEY, J. J. & D'ASARO, E. A. 1995 Available potential energy and mixing in density-stratified fluids. *J. Fluid Mech.* **289**, 115–128.

ZHOU, Q., TAYLOR, J. R. & CAULFIELD, C. P. 2017 Self-similar mixing in stratified plane Couette flow for varying Prandtl number. *J. Fluid Mech.* **820**, 86–120.